# HELIOS: A ZERO-DIMENSIONAL TOOL FOR NEXT STEP AND REACTOR STUDIES

JEAN JOHNER*

*CEA, IRFM, F-13108 Saint-Paul-lez-Durance, France*

Received June 8, 2010
Accepted for Publication September 26, 2010

*The HELIOS zero-dimensional code (Version 1.0) is described in detail in the case of deuterium-tritium (D-T) plasmas.*

*The part of the code described solves in a self-consistent way the thermal equilibrium equation of a D-T thermonuclear plasma coupled to the conservation equation of the helium ash with a* $\tau^*_{He}/\tau_E$ = *const. constraint.*

*Prominent features of the modeling are the following: description of any type of last closed magnetic surface (LCMS) by means of four portions of conics; exact closed form expressions for the poloidal surface, plasma volume, plasma surface, and LCMS length; exact surface and volume integration (for arbitrary aspect ratio) in the approximation of magnetic surfaces similar to the LCMS; parabolic type density profile and two-parameters temperature profile, both with pedestals and finite values at the separatrix; line radiation of light impurities calculated from tabulated radiative power loss functions; scalings for the pedestal temperature, L-H transition, and confinement time; modeling for the divertor thermal load; self-consistent radial build modeling for the plateau duration calculation; and detailed power plant thermal balance.*

*Applications to ITER and DEMO operation and to inductive reactor design are given.*

**KEYWORDS:** *ITER, DEMO, zero-dimensional model*

*Note: Some figures in this paper are in color only in the electronic version.*

## I. INTRODUCTION

Zero-dimensional (0-D) codes solving the thermal equilibrium equation of a thermonuclear plasma, coupled with the conservation equations for ashes, are still useful tools for the quick prediction of next step machine performances and the performances of DEMO and reactor designs. They are well adapted to parametric studies and for the preparation of more precise one-dimensional (1-D) simulations. Here, a detailed description of the HELIOS code is given. The code has been used recently for ITER parametric studies,[1] assessment of FT3 (Ref. 2), for private assessments of JT-60SA reduced field and Power Plant Conceptual Study[3] (PPCS) DEMO projects, and for preliminary purely inductive reactor design.

Compared to other 0-D approaches (PROCESS systems code[4] and ARIES systems code[5]), the HELIOS code puts the emphasis on the following points:

1. precision of the plasma shape description (using two elongations, two triangularities, and four angles)
2. numerical efficiency in the computation of geometrical parameters [exact closed form expressions are used for the calculation of the last closed magnetic surface (LCMS) length, plasma volume, poloidal and toroidal surfaces, and finite aspect ratio corrections to the volume integration]
3. precision of the density and temperature profiles (finite pedestal and separatrix values for both density and temperature, finite pedestal width, two-parameters temperature profile in the core plasma). Such profiles, which give realistic values of density and temperature near the plasma edge, allow the exact calculation of line-radiation losses in the plasma bulk inside the separatrix. Also, the pedestal width may be adjusted for the maximum pressure gradient inside the pedestal to meet the ballooning stability criterion.

*E-mail: jean.johner@cea.fr

4. precision of the plateau loop voltage calculation in the case of (partial) inductive current drive. The $1/R$ variation of the equilibrium electric field is properly taken into account in the loop voltage calculation.

In Sec. II, the plasma modeling is described in detail in the case of 50-50 deuterium-tritium (D-T) mixtures (the way the code can treat the case of D-$^3$He mixtures is only briefly mentioned). After thermal equilibrium and He conservation equations have been presented, geometry, profiles, composition, thermonuclear source, ohmic power, bremsstrahlung, synchrotron and line-radiation losses, transport losses, and helium ash contents calculation are reviewed. The operating window is then described with the associated modeling for density and beta limits, L-H transition, and maximum thermal load on the divertor plates. Finally, additional features are described. They include the description of the modeling for the pedestal, the bootstrap current calculation, external current drive, inductive discharge duration, and the maximum magnetic field inside the superconducting windings.

In Sec. III, the modeling implemented for the power plant balance is discussed, with particular attention given to the power required for pumping. In Sec. IV, to demonstrate the use of the code, examples of its application to ITER, DEMO, and inductive reactor design are given. The scenario 2 ($Q = 10$, $P_{fus} = 400$ MW) operating point in ITER is obtained at 85% of the Greenwald density limit using IPB98($y$,2) scaling[6] and a temperature profile in good agreement with 1-D simulations. The sensitivity of ITER performances to the toroidal magnetic field magnitude and the effect of using ITERH06-IP($y, dd$) scaling[7] for the energy confinement time are illustrated. DEMO-PPCS-C and DEMO-2007 performances are also considered, showing the strong negative effect of the divertor load constraint and of the large recirculated power required for helium pumping. Finally, a preliminary design of an ITER-like, purely inductive, pure H-mode reactor results in very large machines with relatively low plateau durations. Unless explicitly stated, mksa units are used except for the temperature, which is always expressed in keV (Boltzmann's constant $k = 1.6021892 \times 10^{-16}$ J/keV).

## II. PLASMA MODELING

In this section, the plasma modeling implemented in the HELIOS code is described in detail.

### II.A. Thermal Equilibrium and Helium Conservation

#### *II.A.1. Plasma Core, Plasma Mantle, Core Energy Confinement Time*

The plasma inside the LCMS, also called plasma bulk, is divided into a plasma core (for $\rho < \rho_{core}$) and a plasma mantle region (for $\rho_{core} < \rho < 1$) where $\rho$ is the nondimensional radial coordinate defined later. The plasma core is the plasma region where the main mechanism for thermal losses is conduction-convection. The corresponding power $P_{con}$ at the edge of the core region is used to define the core energy confinement time $\tau_E$ as

$$\tau_E = \frac{W_{th}}{P_{con}} \quad . \tag{1}$$

The plasma mantle is the plasma region close to the LCMS where line-radiation mechanisms are dominant. The power $P_{con}$ enters the plasma mantle where it is partially radiated. The remaining part is the power $P_{sep}$ crossing the separatrix.

The introduction of a plasma core and plasma mantle is made necessary when describing conduction-convection losses using a 0-D global confinement time. It avoids obtaining infinite values of $\tau_E$ in discharges with high edge line radiation (as the conducted power is very low in this case for $\rho = 1$). The precise value of $\rho_{core}$ (which is close to 1) has very little effect on the core thermal equilibrium (actually, integrals in the core thermal equilibrium equation are performed from $\rho = 0$ to 1 except for $P_{line\text{-}core}$). $\rho_{core}$ is essentially required for the calculation of $P_{sep}$, which is used in the L-H transition criterion. The $\rho_{core}$ radius, which depends on the density and temperature conditions near the separatrix, is chosen "by hand," looking at the line-radiation profile curve (see Fig. 11 in Sec. IV). In this paper, $\rho_{core} = 0.95$ is taken. The imprecision inherent in this choice is a limitation of the 0-D approach (no such concept exists in the 1-D description where conduction is clearly defined everywhere using a thermal diffusivity).

#### *II.A.2. Thermal Equilibrium of the Plasma Core and Helium Conservation*

In the case of D-T plasmas, the following equations are solved self-consistently by the HELIOS code:

*Core thermal equilibrium equation:*

$$\begin{aligned} F_{P_\alpha} P_\alpha(n_e, T_e, n_{\rm He}) + P_{OH}(n_e, T_e, n_{\rm He}) + P_{add} \\ = P_B(n_e, T_e, n_{\rm He}) + P_{syn}(n_e, T_e) \\ + P_{line\text{-}core}(n_e, T_e) + P_{con}(n_e, T_e, n_{\rm He}, P_{net}) \end{aligned} \tag{2}$$

and

*Conservation of He:*

$$S_{\rm He}(n_e, T_e, n_{\rm He}) = \frac{N_{\rm He}}{\tau^*_{\rm He}} \quad . \tag{3}$$

In Eqs. (2) and (3), $n_e$ and $T_e$ symbolically denote the electron density and temperature, and $n_{\mathrm{He}}$ denotes the helium density. In practice, the HELIOS code solves Eqs. (2) and (3) expressed in terms of the parameters $\langle n_e \rangle$, $\langle T_e \rangle_n$, and $f_{\mathrm{He}}$, which are defined later. $P_\alpha$ is the thermonuclear power that is produced inside the plasma core in the form of alpha particles, and $F_{P_\alpha}$ is the fraction of this power that is trapped within the plasma ($F_{P_\alpha}$ is introduced for completeness, as for typical tokamak currents, direct loss of alpha particles is negligible so that $F_{P_\alpha}$ is always taken to be 1 here). $P_{OH}$ and $P_{add}$ are the ohmic and additional power sources; $P_B$ and $P_{syn}$ are the bremsstrahlung and synchrotron radiation losses; $P_{line\text{-}core}$ is the power lost in the plasma core by line-radiation mechanism (bremsstrahlung excluded); and $P_{con}$ is the conduction-convection transport loss at the edge of the core region.

In the calculation of $P_\alpha$, $P_{OH}$, $P_B$, $P_{syn}$, and $W_{th}$, no difference is made between the plasma core and the plasma inside the LCMS. In the calculation of $P_{line\text{-}core}$, a $\rho_{core} < 1$ value is taken. $S_{\mathrm{He}}$ is the helium source (number of alpha particles produced by the thermonuclear reactions per unit time), $N_{\mathrm{He}}$ is the total number of helium ions present in the plasma, and $\tau^*_{\mathrm{He}}$ is (by definition) the apparent helium confinement time. It includes the effects of He diffusion losses and recycling sources, so that it depends on the pumping speed.

After a detailed description of the geometry, source and loss terms in Eqs. (2) and (3) will be described in the order in which they appear. Sections II.B through II.F may be skipped by the reader more interested in the physics contents.

### II.B. Geometry

#### *II.B.1. The Poloidal Section*

We consider an axisymmetric torus with a poloidal section shape defined by two elongations $\kappa_X^{(1)}$, $\kappa_X^{(2)}$, two triangularities $\delta_X^{(1)}$, $\delta_X^{(2)}$, and four angles $\psi^{-(1)}$, $\psi^{+(1)}$, $\psi^{-(2)}$, $\psi^{+(2)}$ as described in Fig. 1.

The four portions of the LCMS are taken to be conic arcs, the nature of which depends on $\kappa_X$, $\delta_X$, and $\psi$.

For the inner parts of the LCMS, we introduce

$$t^- = \frac{1-\delta_X}{\kappa_X} \tan\psi^- \quad .$$

Note that $t^- \leq 1$.

If $t^- < \frac{1}{2}$, the portion is an arc of ellipse with the following parametric equations (with $\xi = x/a$ and $\zeta = z/a$, where $x$ is the distance measured from the major radius $R$):

$$\begin{cases} \xi = \alpha_0^- - \alpha^- \cos\theta \\ \zeta = \beta^- \sin\theta \end{cases} ,$$

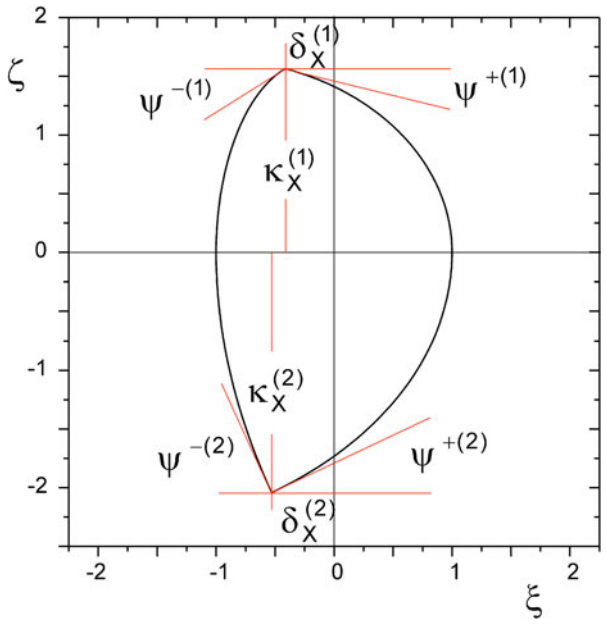


Fig. 1. Description of the poloidal section shape in the HELIOS code.

where

$$\alpha_0^- = -\frac{\delta_X - (1+\delta_X)t^-}{1-2t^-} \quad ,$$

$$\alpha^- = (1-\delta_X)\frac{1-t^-}{1-2t^-} \quad ,$$

and

$$\beta^- = \kappa_X \frac{1-t^-}{\sqrt{1-2t^-}} \tag{4}$$

and where

$$0 \leq \theta \leq \theta_X^- \quad \text{or} \quad -\theta_X^- \leq \theta \leq 0 \quad ,$$

depending on whether the considered portion belongs to the upper or lower part of the torus, respectively. We have

$$\theta_X^- = \arcsin\frac{\sqrt{1-2t^-}}{1-t^-} \quad . \tag{5}$$

If $t^- = \frac{1}{2}$, the portion is an arc of parabola with the following equation:

$$\xi = -1 + \frac{1-\delta_X}{\kappa_X^2}\zeta^2 \quad ,$$

where

$$0 \leq \zeta \leq \kappa_X \quad \text{or} \quad -\kappa_X \leq \zeta \leq 0$$

depending on whether the considered portion belongs to the upper or lower part of the torus, respectively.

If $t^- > \frac{1}{2}$, the portion is an arc of hyperbola with the following parametric equations:

$$\begin{cases} \xi = \alpha_0^- + \alpha^- \cosh\varphi \\ \zeta = \beta^- \sinh\varphi \end{cases} ,$$

where

$$\alpha_0^- = -\frac{(1+\delta_X)t^- - \delta_X}{2t^- - 1} ,$$

$$\alpha^- = (1-\delta_X)\frac{1-t^-}{2t^- - 1} ,$$

and

$$\beta^- = \kappa_X \frac{1-t^-}{\sqrt{2t^- - 1}} \tag{6}$$

and where

$$0 \le \varphi \le \varphi_X^- \quad \text{or} \quad -\varphi_X^- \le \varphi \le 0 ,$$

depending on whether the considered portion belongs to the upper or lower part of the torus, respectively. We have

$$\varphi_X^- = \operatorname{arcsinh}\frac{\sqrt{2t^- - 1}}{1-t^-} . \tag{7}$$

If $t^- = 1$, the portion is a straight line with the following equation:

$$\xi = -1 + \frac{1-\delta_X}{\kappa_X}\zeta ,$$

where

$$0 \le \zeta \le \kappa_X \quad \text{or} \quad -\kappa_X \le \zeta \le 0 ,$$

depending on whether the considered portion belongs to the upper or lower part of the torus, respectively.

For the outer parts of the LCMS, we introduce

$$t^+ = \frac{1+\delta_X}{\kappa_X}\tan\psi^+ .$$

Note that $t^+ \le 1$.

If $t^+ < \frac{1}{2}$, the portion is an arc of ellipse with the following parametric equations:

$$\begin{cases} \xi = \alpha_0^+ + \alpha^+ \cos\theta \\ \zeta = \beta^+ \sin\theta \end{cases} ,$$

where

$$\alpha_0^+ = -\frac{\delta_X + (1-\delta_X)t^+}{1-2t^+} ,$$

$$\alpha^+ = (1+\delta_X)\frac{1-t^+}{1-2t^+} ,$$

and

$$\beta^- = \kappa_X \frac{1-t^+}{\sqrt{1-2t^+}} \tag{8}$$

and where

$$0 \le \theta \le \theta_X^+ \quad \text{or} \quad -\theta_X^+ \le \theta \le 0 ,$$

depending on whether the considered portion belongs to the upper or lower part of the torus, respectively. We have

$$\theta_X^+ = \arcsin\frac{\sqrt{1-2t^+}}{1-t^+} . \tag{9}$$

If $t^+ = \frac{1}{2}$, the portion is an arc of parabola with the following equation:

$$\xi = -1 - \frac{1+\delta_X}{\kappa_X^2}\zeta^2 ,$$

where

$$0 \le \zeta \le \kappa_X \quad \text{or} \quad -\kappa_X \le \zeta \le 0 ,$$

depending on whether the considered portion belongs to the upper or lower part of the torus, respectively.

If $t^+ > \frac{1}{2}$, the portion is an arc of hyperbola with the following parametric equations:

$$\begin{cases} \xi = \alpha_0^+ + \alpha^+ \cosh\varphi \\ \zeta = \beta^+ \sinh\varphi \end{cases} ,$$

where

$$\alpha_0^+ = \frac{(1-\delta_X)t^+ + \delta_X}{2t^+ - 1} ,$$

$$\alpha^+ = -(1+\delta_X)\frac{1-t^+}{2t^+ - 1} ,$$

and

$$\beta^+ = \kappa_X \frac{1-t^+}{\sqrt{2t^+ - 1}} \tag{10}$$

and where

$$0 \le \varphi \le \varphi_X^+ \quad \text{or} \quad -\varphi_X^+ \le \varphi \le 0 ,$$

depending on whether the considered portion belongs to the upper or lower part of the torus, respectively. We have

$$\varphi_X^+ = \text{arcsinh}\,\frac{\sqrt{2t^+ - 1}}{1 - t^+} \quad . \tag{11}$$

If $t^+ = 1$, the portion is a straight line with the following equation:

$$\xi = 1 - \frac{1 + \delta_X}{\kappa_X}\zeta \ ,$$

where

$$0 \le \zeta \le \kappa_X \quad \text{or} \quad -\kappa_X \le \zeta \le 0 \ ,$$

depending on whether the considered portion belongs to the upper or lower part of the torus, respectively.

*II.B.2. Volume, Surfaces, and Length*

With the above LCMS description, the volume inside the separatrix, the surface of the plasma cross section, the toroidal surface of the LCMS, and the length of the separatrix may be expressed in closed form with the help of elliptic integrals.

*The Case of an Up-Down Symmetrical Section*

This case corresponds to

$$\kappa_X^{(1)} = \kappa_X^{(2)} = \kappa_X \ ,$$

$$\delta_X^{(1)} = \delta_X^{(2)} = \delta_X \ ,$$

$$\psi^{-(1)} = \psi^{-(2)} = \psi^- \ ,$$

and

$$\psi^{+(1)} = \psi^{+(2)} = \psi^+ \ .$$

The inner volume $V$, the poloidal surface $S_p$, the toroidal surface $S$, and the length $L$ of the LCMS may be written as

$$V = 2\pi^2 R\kappa_X a^2 \Theta_V^* \ ,$$

$$S_p = \pi\kappa_X a^2 \Theta_{Sp}^* \ ,$$

$$S = 4\pi^2 Ra\boldsymbol{E}_1(\kappa_X)\Theta_S^* \ ,$$

and

$$L = 2\pi a\boldsymbol{E}_1(\kappa_X)\Theta_L^* \ ,$$

with

$$\Theta_V^*(\kappa_X, \delta_X, \psi^-, \psi^+, A) \ ,$$

$$\Theta_{Sp}^*(\kappa_X, \delta_X, \psi^-, \psi^+) \ ,$$

$$\Theta_S^*(\kappa_X, \delta_X, \psi^-, \psi^+, A) \ ,$$

and

$$\Theta_L^*(\kappa_X, \delta_X, \psi^-, \psi^+) \ ,$$

where $A = R/a$ is the torus aspect ratio and

$$\boldsymbol{E}_1(k) = \frac{2}{\pi}k\boldsymbol{E}\left(\sqrt{1 - \frac{1}{k^2}}\right) \quad \text{for } k \ge 1, \boldsymbol{E}_1(1) = 1 \ ,$$

where

$$\boldsymbol{E}(k) = \int_0^{\pi/2} \sqrt{1 - k^2 \sin^2\theta}\, d\theta \quad \text{for } 0 \le k \le 1$$

is the complete elliptic integral of the second kind.

In the above expressions, $\Theta_V^*$, $\Theta_{Sp}^*$, $\Theta_S^*$, and $\Theta_L^*$ are the corrections with respect to the pure elliptic case ($\delta_X = \psi^- = \psi^+ = 0$). Each of these functions may be decomposed in an inner and outer part according to

$$\Theta_V^* = \Theta_V^{*-} + \Theta_V^{*+} \ ,$$

$$\Theta_{Sp}^* = \Theta_{Sp}^{*-} + \Theta_{Sp}^{*+} \ ,$$

$$\Theta_S^* = \Theta_S^{*-} + \Theta_S^{*+} \ ,$$

and

$$\Theta_L^* = \Theta_L^{*-} + \Theta_L^{*+} \ ,$$

with

$$\Theta_V^{*-}(\kappa_X, \delta_X, \psi^-, A) \ ,$$

$$\Theta_V^{*+}(\kappa_X, \delta_X, \psi^+, A) \ ,$$

$$\Theta_{Sp}^{*-}(\kappa_X, \delta_X, \psi^-) \ ,$$

$$\Theta_{Sp}^{*+}(\kappa_X, \delta_X, \psi^+) \ ,$$

$$\Theta_S^{*-}(\kappa_X, \delta_X, \psi^-, A) \ ,$$

$$\Theta_S^{*+}(\kappa_X, \delta_X, \psi^+, A) \ ,$$

$$\Theta_L^{*-}(\kappa_X, \delta_X, \psi^{*-}) \ ,$$

and

$$\Theta_L^{*+}(\kappa_X, \delta_X, \psi^+) \ .$$

Expressions for $\Theta_V^{*-}$, $\Theta_V^{*+}$, $\Theta_{Sp}^{*-}$, $\Theta_{Sp}^{*+}$, $\Theta_S^{*-}$, $\Theta_S^{*+}$, $\Theta_L^{*-}$, and $\Theta_L^{*+}$ are given in Appendix A. They have been checked by comparison with calculation of volume, surfaces, and length from their original integral expressions.

In the special case of an up-down symmetrical LCMS with no *X*-points ($\psi^- = \psi^+ = 0$), we obtain

$$\Theta_V^* = 1 - \left(1 - \frac{8}{3\pi}\right)\frac{\delta_X}{A} \ ,$$

$$\Theta_{Sp}^* = 1 \text{ independent of } \delta_X \ ,$$

$$\Theta_S^* = \frac{1}{\boldsymbol{E}_1(\kappa_X)}\left[\left(1 - \frac{\delta_X}{A}\right)\left(\frac{1+\delta_X}{2}\boldsymbol{E}_1(\kappa^+) + \frac{1-\delta_X}{2}\boldsymbol{E}_1(\kappa^-)\right) + \cdots \right.$$
$$\left. + \frac{\kappa_X}{\pi A}\left(\frac{1+\delta_X}{2}\frac{\arcsin\sqrt{1-1/\kappa^{+2}}}{\sqrt{1-1/\kappa^{+2}}} - \frac{1-\delta_X}{2}\frac{\arcsin\sqrt{1-1/\kappa^{-2}}}{\sqrt{1-1/\kappa^{-2}}}\right) + \frac{2\delta_X}{\pi A}\right] ,$$

and

$$\Theta_L^* = \frac{1}{\boldsymbol{E}_1(\kappa_X)}\left(\frac{1+\delta_X}{2}\boldsymbol{E}_1(\kappa^+) + \frac{1-\delta_X}{2}\boldsymbol{E}_1(\kappa^-)\right) ,$$

where $\kappa^-$ and $\kappa^+$ are defined in Appendix A.

*The Case of an Asymmetrical Configuration*

Introducing the mean LCMS elongation $\kappa_X$ as

$$\kappa_X = \frac{\kappa_X^{(1)} + \kappa_X^{(2)}}{2} \ , \qquad (12)$$

the inner volume $V$, the poloidal surface $S_p$, the toroidal surface $S$, and the length $L$ of the LCMS are written as

$$V = 2\pi^2 R\kappa_X a^2 \Theta_V \ ,$$

$$S_p = \pi\kappa_X a^2 \Theta_{Sp} \ ,$$

$$S = 4\pi^2 Ra\boldsymbol{E}_1(\kappa_X)\Theta_S \ ,$$

and

$$L = 2\pi a\boldsymbol{E}_1(\kappa_X)\Theta_L \ , \qquad (13)$$

with

$$\Theta_V(\kappa_X^{(1)}, \delta_X^{(1)}, \psi^{-(1)}, \psi^{+(1)}, \kappa_X^{(2)}, \delta_X^{(2)}, \psi^{-(2)}, \psi^{+(2)}, A) \ ,$$

$$\Theta_{Sp}(\kappa_X^{(1)}, \delta_X^{(1)}, \psi^{-(1)}, \psi^{+(1)}, \kappa_X^{(2)}, \delta_X^{(2)}, \psi^{-(2)}, \psi^{+(2)}) \ ,$$

$$\Theta_S(\kappa_X^{(1)}, \delta_X^{(1)}, \psi^{-(1)}, \psi^{+(1)}, \kappa_X^{(2)}, \delta_X^{(2)}, \psi^{-(2)}, \psi^{+(2)}, A) \ ,$$

and

$$\Theta_L(\kappa_X^{(1)}, \delta_X^{(1)}, \psi^{-(1)}, \psi^{+(1)}, \kappa_X^{(2)}, \delta_X^{(2)}, \psi^{-(2)}, \psi^{+(2)}) \ ;$$

$\Theta_V$, $\Theta_{Sp}$, $\Theta_S$, and $\Theta_L$ are then the corrections with respect to the pure symmetrical elliptic case (i.e., the ellipse enclosed in the cross-section rectangle as illustrated in Fig. 2). It can be shown that

$$\Theta_V = \frac{\kappa_X^{(1)}\Theta_V^{*(1)} + \kappa_X^{(2)}\Theta_V^{*(2)}}{\kappa_X^{(1)} + \kappa_X^{(2)}} \ ,$$

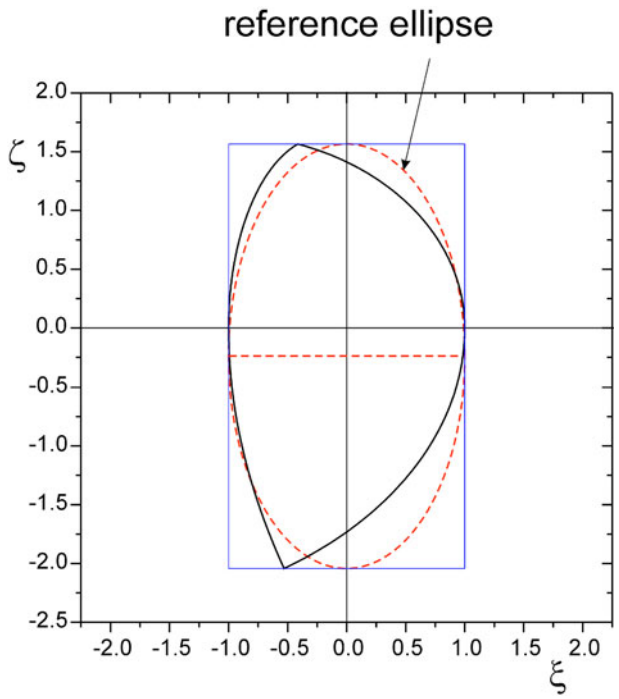


Fig. 2. Reference ellipse in the case of an asymmetrical configuration.

$$\Theta_{Sp} = \frac{\kappa_X^{(1)}\Theta_{Sp}^{*(1)} + \kappa_X^{(2)}\Theta_{Sp}^{*(2)}}{\kappa_X^{(1)} + \kappa_X^{(2)}} \quad ,$$

$$\Theta_S = \frac{\frac{1}{2}\left(\boldsymbol{E}_1(\kappa_X^{(1)})\Theta_S^{*(1)} + \boldsymbol{E}_1(\kappa_X^{(2)})\Theta_S^{*(2)}\right)}{\boldsymbol{E}_1\left(\frac{\kappa_X^{(1)} + \kappa_X^{(2)}}{2}\right)} \quad ,$$

and

$$\Theta_L = \frac{\frac{1}{2}\left(\boldsymbol{E}_1(\kappa_X^{(1)})\Theta_L^{*(1)} + \boldsymbol{E}_1(\kappa_X^{(2)})\Theta_L^{*(2)}\right)}{\boldsymbol{E}_1\left(\frac{\kappa_X^{(1)} + \kappa_X^{(2)}}{2}\right)} \quad ,$$

with

$$\Theta_Y^{*(1)} = \Theta_Y^*(\kappa_X^{(1)}, \delta_X^{(1)}, \psi^{-(1)}, \psi^{+(1)}, A)$$

and

$$\Theta_Y^{*(2)} = \Theta_Y^*(\kappa_X^{(2)}, \delta_X^{(2)}, \psi^{-(2)}, \psi^{+(2)}, A) \quad .$$

In the special case of a LCMS with no *X*-points $[\psi^{-(1)} = \psi^{+(1)} = \psi^{-(2)} = \psi^{+(2)} = 0]$, we obtain

$$\Theta_V = 1 - \left(1 - \frac{8}{3\pi}\right)\frac{1}{A}\,\frac{\kappa_X^{(1)}\delta_X^{(1)} + \kappa_X^{(2)}\delta_X^{(2)}}{\kappa_X^{(1)} + \kappa_X^{(2)}}$$

and

$$\Theta_{Sp} = 1 \quad .$$

### *II.B.3. Magnetic Surfaces Modeling, Poloidal Surface Integration, and Volume Integration*

The magnetic surfaces are supposed to be similar to the outer magnetic surface. The similarity center *O* is situated at the middle of the horizontal axis of the LMCS (no Shafranov shift). The similarity factor is $\rho$ ($\rho = 0$ at the magnetic axis, $\rho = 1$ at the plasma boundary). Such magnetic surfaces of course do not represent solutions of the Grad-Shafranov equation, but they constitute a good preliminary approximation to take profile effects into account.

For any shape of the LCMS and any function $F(\rho)$, we have (see Appendix B):

$$\langle F\rangle_{S_p} = \frac{1}{S_p}\int_{S_p} F(\rho)\,dS_p = \int_0^1 F(\rho)2\rho\,d\rho \qquad (14)$$

and

$$\langle F\rangle = \frac{1}{V}\int_V F(\rho)\,dV = \frac{1}{1 - \frac{\Theta_1}{A}}\int_0^1 F(\rho)\left(1 - \frac{3}{2}\,\frac{\Theta_1}{A}\,\rho\right)2\rho\,d\rho \quad , \qquad (15)$$

where $\langle F\rangle_{S_p}$ and $\langle F\rangle$ denote poloidal surface and volume averages, respectively. $\Theta_1$ is only a function of the shape of the LCMS and of the aspect ratio; it can be expressed in terms of $\Theta_{Sp}$ and $\Theta_V$:

$$\frac{\Theta_1}{A} = 1 - \frac{\Theta_V}{\Theta_{Sp}} \quad . \qquad (16)$$

In the special case of a LCMS with no *X*-points ($\psi^{-(1)} = \psi^{+(1)} = \psi^{-(2)} = \psi^{+(2)} = 0$), we obtain

$$\Theta_1 = \left(1 - \frac{8}{3\pi}\right)\frac{\kappa_X^{(1)}\delta_X^{(1)} + \kappa_X^{(2)}\delta_X^{(2)}}{\kappa_X^{(1)} + \kappa_X^{(2)}} \quad .$$

For poloidal surface and volume integration over the restricted region corresponding to $0 \le \rho \le \rho_0$, we have

$$\int_{S_{p0}} F(\rho)\,dS_p = S_p\int_0^{\rho_0} F(\rho)2\rho\,d\rho$$

and

$$\int_{V_0} F(\rho)\,dV = \frac{V}{1 - \frac{\Theta_1}{A}} \times \int_0^{\rho_0} F(\rho)\left(1 - \frac{3}{2}\,\frac{\Theta_1}{A}\,\rho\right)2\rho\,d\rho \quad .$$

In particular, we get

$$S_{p_0} = S_p\,\rho_0^2$$

and

$$V_0 = V\rho_0^2\,\frac{1 - \frac{\Theta_1}{A}\,\rho_0}{1 - \frac{\Theta_1}{A}} \quad .$$

## II.C. Safety Factor at the Plasma Edge

Some ingredients of the modeling implemented in the HELIOS code are dependent of the safety factor at the plasma edge (peak heat flux on the divertor target plates, critical pressure gradient in the pedestal region). As no magnetic equilibrium is calculated in the code, the safety factor at the plasma edge ($q_{95}$) in the case of a configuration with *X* points will be taken to be the following standard ITER fit[6,8]:

$$q_{95} = \frac{2\pi}{\mu_0}\,\frac{B_t a^2}{RI_p}\,\frac{1.17 - \frac{0.65}{A}}{\left(1 - \frac{1}{A^2}\right)^2} \times \frac{1 + \kappa_{95}^2(1 + 2\delta_{95}^2 - 1.2\delta_{95}^3)}{2} \quad . \qquad (17)$$

## II.D. Profiles, Average Values

### *II.D.1. Density and Temperature Profiles*

*Density and Temperature Profiles with Pedestals and Finite Values at the Separatrix*

The density and temperature profiles considered in the code may exhibit nonzero values at the separatrix as well as pedestals (characterized by the pedestal radius $\rho_{ped}$ and the pedestal values $n_{ped}$ and $T_{ped}$). The density and temperature profiles are given by the following expressions:

$$n(\rho) = \begin{cases} n_{ped} + (n_0 - n_{ped})\left(1 - \dfrac{\rho^2}{\rho_{ped}^2}\right)^{\alpha_n} \\ \qquad \text{for } 0 \le \rho \le \rho_{ped} \\ n_{sep} + (n_{ped} - n_{sep})\,\dfrac{1-\rho}{1-\rho_{ped}} \\ \qquad \text{for } \rho_{ped} \le \rho \le 1 \end{cases} \tag{18}$$

and

$$T(\rho) = \begin{cases} T_{ped} + (T_0 - T_{ped})\left(1 - \dfrac{\rho^{\beta_T}}{\rho_{ped}^{\beta_T}}\right)^{\alpha_T} \\ \qquad \text{for } 0 \le \rho \le \rho_{ped} \\ T_{sep} + (T_{ped} - T_{sep})\,\dfrac{1-\rho}{1-\rho_{ped}} \\ \qquad \text{for } \rho_{ped} \le \rho \le 1 \ . \end{cases} \tag{19}$$

It can be seen that the density and temperature vary linearly between $\rho = \rho_{ped}$ and $\rho = 1$. In the interior region, the density has a parabolic type profile (parabolic with an exponent $\alpha_n$) while the temperature profile has a two-parameters profile (the square exponent is replaced by the more general $\beta_T$ exponent). This latter profile allows a more accurate description of temperature profiles with a triangular shape or a strong gradient near the pedestal (characteristic of regimes with an internal transport barrier).

*Density and temperature at the separatrix*: The electronic density and temperature at the separatrix are free parameters in the HELIOS code. For ITER and DEMO calculations, the following values are taken:

$$n_{e,sep} = 0.3 \times 10^{20}\ \text{m}^{-3} \quad \text{and} \quad T_{e,sep} = 100\ \text{eV} \ .$$

*Pedestal temperature and width*: The pedestal temperature may be either given or calculated from a scaling. The pedestal width may be either given or calculated from a simplified ballooning stability criterion. See Sec. II.L.1 for more details.

*Parabolic Type Density and Temperature Profiles*

Many 0-D codes use the so-called parabolic type density profiles, i.e.,

$$n(\rho) = n_0(1 - \rho^2)^{\alpha_n} \tag{20}$$

and

$$T(\rho) = T_0(1 - \rho^2)^{\alpha_T} \ . \tag{21}$$

These profiles are a particular case of the above profiles taking $\beta_T = 2$, $n_{ped} = T_{ped} = 0$, $n_{sep} = T_{sep} = 0$, $\rho_{ped} = 1$.

In this case, all the coefficients appearing in the calculation of average quantities may be calculated in closed form, as well as bremsstrahlung losses. The corresponding expressions will be given explicitly for completeness.

### *II.D.2. Average Quantities*

Different average quantities are used in the code:

1. *line averaged density*:

$$\bar{n} = \frac{1}{a}\int_0^a n(x)\,dx = \int_0^1 n(\rho)\,d\rho$$

2. *volume averaged density and temperature*: as defined in Eq. (15) for $n$ or $T$

3. *density averaged electron temperature*:

$$\langle T_e \rangle_n = \frac{\displaystyle\int_V n_e T_e(\rho)\,dV}{\displaystyle\int_V n_e(\rho)\,dV} \ .$$

The density averaged electron temperature is the temperature parameter used internally in the code for historical reasons. It allows very simple expressions for the thermal energy contents $W_{th}$ [Eq. (40)] and for the thermal beta parameter $\beta_{th}$ [Eq. (46)].

*The Case of the General Profiles*

The electron density profile is supposed to be described by giving the electron density at the separatrix $n_{e,sep}$, the shape parameter $\alpha_n$, the central versus pedestal peaking parameter $n_{e0}/n_{e,ped}$, and the pedestal radius $\rho_{ped}$. The inverse of the $n_{e0}/n_{e,ped}$ parameter is introduced, i.e.,

$$n^*_{ped} = \frac{n_{e,ped}}{n_{e0}} \ .$$

The volume averaged electron density $\langle n_e \rangle$ is the density variable used internally in the code. The following expressions allow the calculation of $n_{e0}$, $\bar{n}_e$, and $n_{e,ped}$ in terms of $\langle n_e \rangle$, $n_{e,sep}$, $\alpha_n$, $n^*_{ped}$, and $\rho_{ped}$:

$$n_{e0} = \frac{\langle n_e \rangle - (I^{(1)} - I^{(1)}_{lin1}) n_{e,sep}}{n^*_{ped}(I^{(0)} + I^{(1)}_{lin1}) + (1 - n^*_{ped}) I^{(0)}_n} \ ,$$

$$\bar{n}_e = \left[ n^*_{ped} \frac{1 + \rho_{ped}}{2} + (1 - n^*_{ped}) \rho_{ped} \Gamma_2(\alpha_n) \right] n_{e0} + \frac{1}{2} (1 - \rho_{ped}) n_{e,sep} \ ,$$

$$n_{e,ped} = n_{e0} n^*_{ped} \ ,$$

with

$$\Gamma_2(\alpha) = \frac{\sqrt{\pi}}{2} \frac{\Gamma(1 + \alpha)}{\Gamma\left(\frac{3}{2} + \alpha\right)} \ , \quad \Gamma_2(0) = 1 \ ,$$

where $\Gamma$ is the Euler Gamma function.

The electron temperature profile is supposed to be described by giving the electron temperatures at the separatrix ($T_{e,sep}$), at the pedestal ($T_{e,ped}$), the shape parameters $\beta_T$, $\alpha_T$, and the pedestal radius $\rho_{ped}$.

The following expressions allow the calculation of $T_{e0}$,$\langle T_e \rangle$ in terms of $\langle T_e \rangle_n$ (internal temperature parameter), $T_{e,ped}$, $T_{e,sep}$, $\beta_T$, $\alpha_T$, $\rho_{ped}$, and of the parameters describing the density profile:

$$T_{e0} = \frac{A_0 \langle T_e \rangle_n - B_0 T_{e,ped} - C_0 T_{e,sep}}{[n^*_{ped} I^{(0)}_T + (1 - n^*_{ped}) I^{(0)}_{nT}][\langle n_e \rangle - (I^{(1)} - I^{(1)}_{lin1}) n_{e,sep}]} \ ,$$

$$\langle T_e \rangle = I^{(0)}_T T_{e0} + (I^{(0)} - I^{(0)}_T + I^{(1)}_{lin1}) T_{e,ped} + (I^{(1)} - I^{(1)}_{lin1}) T_{e,sep} \ ,$$

or

$$\langle T_e \rangle = \frac{A_V \langle T_e \rangle_n + B_V T_{e,ped} + C_V T_{e,sep}}{[n^*_{ped} I^{(0)}_T + (1 - n^*_{ped}) I^{(0)}_{nT}][\langle n_e \rangle - (I^{(1)} - I^{(1)}_{lin1}) n_{e,sep}]} \ .$$

All the coefficients appearing in the above expressions can be expressed in closed form using the integral expressions given in Appendix C except the $I^{(0)}_{nT}$ function, which must be calculated numerically. These expressions are given in Appendix D.

*The Case of Parabolic Type Profiles*

In this case, the above expressions simplify to the closed form formulas given at the end of Appendix D.

### II.E. $Z_{eff}$, Composition, Impurities

*II.E.1. $Z_{eff}$*

For an arbitrary plasma composition, $Z_{eff}$ is defined as

$$Z_{eff} = \frac{\sum_i n_i Z_i^2}{\sum_i n_i Z_i} \ ,$$

where the summation is done over all ion species $i$.

Using the quasi-neutrality condition ($n_e = \sum_i n_i Z_i$), $Z_{eff}$ may be written as

$$Z_{eff} = \sum_i f_i Z_i^2 = 1 + \sum_{non\text{-}Hoid} Z_i (Z_i - 1) f_i \ ,$$

where

$$f_i = \frac{n_i}{n_e} \tag{22}$$

is the so-called impurity fraction and where the second summation is over nonhydrogenoid ions only.

*II.E.2. Nuclear Reactions*

D-T or D-$^3$He mixtures may be considered in HELIOS. The following fusion reactions are possibly taken into account:

$$\mathrm{D} + \mathrm{T} \rightarrow {}^4\mathrm{He}(3.56\ \mathrm{MeV}) + n(14.03\ \mathrm{MeV}) \quad [17.59\ \mathrm{MeV}] \ , \tag{23}$$

$$\mathrm{D} + {}^3\mathrm{He} \rightarrow {}^4\mathrm{He}(3.71\ \mathrm{MeV}) + p(14.64\ \mathrm{MeV}) \quad [18.35\ \mathrm{MeV}] \ , \tag{24}$$

$$\mathrm{D} + \mathrm{D} \rightarrow {}^3\mathrm{He}(0.82\ \mathrm{MeV}) + n(2.45\ \mathrm{MeV}) \quad [3.27\ \mathrm{MeV}] \ , \tag{25}$$

and

$$\mathrm{D} + \mathrm{D} \rightarrow \mathrm{T}(1.01\ \mathrm{MeV}) + p(3.02\ \mathrm{MeV}) \quad [4.03\ \mathrm{MeV}] \ . \tag{26}$$

*II.E.3. The Case of D-T Plasmas*

In this case, which is the only one described in detail in this paper, an equal mixture of deuterium and tritium ($n_\mathrm{D} = n_\mathrm{T}$) is considered. It will be referred to as a 50-50 D-T mixture. Only reaction in Eq. (23) is retained so that $^3$He and proton concentrations are neglected. In addition to the fraction $f_\mathrm{He}$ of $^4$He ions ($Z_\mathrm{He} = 2$), two light impurity species, with atomic numbers $Z_1$ and $Z_2$, are assumed to be present in the plasma with fractions $f_1$ and $f_2$, respectively. In this case, we have explicitly

$$Z_{eff} = 1 + 2 f_\mathrm{He} + Z_1 (Z_1 - 1) f_1 + Z_2 (Z_2 - 1) f_2 \ .$$

*II.E.4. The Case of D-$^3$He Mixtures*

In this case, we consider arbitrary D-$^3$He mixtures with ionic $^3$He fraction defined as

$$f_{i^3\mathrm{He}} = \frac{n_{^3\mathrm{He}}}{n_\mathrm{D} + n_{^3\mathrm{He}}}$$

(pure D injection plasmas can also be considered). Now, $^4$He and protons are produced by reaction (24); protons are also produced by reaction (26), which has a slightly lower reaction rate; tritium is produced by reaction (26), and it is consumed by reaction (23). All three reactions are considered in the calculation of the equilibrium

density of $^4$He, $p$, and T together with $\tau_p^*/\tau_E = \text{const.}$ and $\tau_T^*/\tau_E = \text{const.}$ conditions. In the same way, reactions (23) through (26) are considered in the calculation of the plasma power source, which results from the slowing down of the produced charged particles.[a]

### II.F. Ratio of Electron to Ion Temperatures

In the D-T case, all the ion species are assumed to have a Maxwellian distribution with the same temperature $T_i$ except He for which nonthermal effects are implemented. The ratio $T_e/T_i$ is supposed to be given and is independent of the radial coordinate $\rho$. The constant ratio

$$\theta_i = \frac{T_i}{T_e}$$

is used in the code.

For a specific operating point, this parameter is obtained from 1-D simulation results. Keeping it independent of $\rho$ and constant over the whole $(n_e, T_e)$ space is clearly one of the limitations of the present modeling.

### II.G. Power Sources

#### *II.G.1. Thermonuclear Power Source*

In the case of a D-T mixture, the number $N_{\rm DT}$ of D-T fusion reactions occurring in the plasma volume is

$$N_{\rm DT} = \int_V n_{\rm D}\, n_{\rm T}\, \overline{\sigma v}_{\rm DT}(T_i)\, dV \ , \qquad (27)$$

where $\overline{\sigma v}_{\rm DT}(T_i)$ is the D-T thermonuclear reaction rate for two D and T Maxwellian populations with the same temperature $T_i$. The expression used for $\overline{\sigma v}_{\rm DT}(T_i)$ is given in Appendix E. The alpha power produced inside the plasma is then

$$P_\alpha = N_{\rm DT} E_\alpha \ ,$$

where $E_\alpha$ is the initial kinetic energy of the alpha particle (3.56 MeV). The plasma kinetic energy is neglected in comparison with the initial alpha particle energy. $N_{\rm DT}$ may be rewritten as

$$N_{\rm DT} = \langle n_{\rm D}\rangle \langle n_{\rm T}\rangle \overline{\sigma v}^*_{\rm DT} V \ ,$$

where $\overline{\sigma v}^*_{\rm DT}$ is the profile averaged thermonuclear reaction rate

$$\overline{\sigma v}^*_{\rm DT} = \frac{\displaystyle\int_V n_{\rm D}\, n_{\rm T}\, \overline{\sigma v}_{\rm DT}(T_i)\, dV}{\langle n_{\rm D}\rangle \langle n_{\rm T}\rangle V} \ ;$$

$\overline{\sigma v}^*_{\rm DT}$ is only a function of the density and temperature profiles and of the average ion temperature. Introducing the density and temperature profiles $n^*(\rho)$ and $T^*(\rho)$ normalized to the central values

$$n^*(\rho) = \frac{n(\rho)}{n_0} \quad \text{and} \quad T^*(\rho) = \frac{T(\rho)}{T_0} \ ,$$

we get explicitly

$$\overline{\sigma v}^*_{\rm DT}(n^*, T^*, \langle T_e\rangle_n) = \left(\frac{n_0}{\langle n\rangle}\right)^2 \frac{1}{1 - \dfrac{\Theta_1}{A}} \int_0^1 n^{*2}(\rho)\overline{\sigma v}_{\rm DT} \ldots \left(\theta_i \frac{T_0}{\langle T\rangle_n} \langle T_e\rangle_n T^*(\rho)\right) \times \left(1 - \frac{3}{2}\frac{\Theta_1}{A}\rho\right) 2\rho\, d\rho \ .$$

In the special case of a 50-50 D-T mixture, $P_\alpha$ may be rewritten as

$$P_\alpha = C_\alpha \frac{\langle n_e\rangle^2}{4} \overline{\sigma v}^*_{\rm DT} E_\alpha V \ ,$$

where $C_\alpha$ is the dilution coefficient in the alpha power source due to the impurity and He contents. In this case

$$C_\alpha = (1 - 2f_{\rm He} - Z_1 f_1 - Z_2 f_2)^2 \ .$$

#### *II.G.2. Ohmic Power*

*Plasma Resistivity*

The ohmic current density is given by

$$j_{OH} = \frac{E}{\eta} \ , \qquad (28)$$

where $\eta$ is the local plasma resistivity. Spitzer resistivity with a simple trapped particles neoclassical correction $\gamma_{NC}$ is taken:

$$\eta(\rho) = \frac{\eta_{00} Z_{eff} \ln\Lambda}{T_e^{3/2}} \gamma_{NC}(A, \rho) \ ,$$

where

$$\eta_{00} = 0.51 \frac{m_e^{1/2} e^2}{3\varepsilon_0^2 (2\pi k)^{3/2}} \simeq 1.66 \times 10^{-9} \ ,$$

$$\ln\Lambda(\rho) = \ln\left(\frac{2\sqrt{3} m_e^{1/2} \varepsilon_0^{1/2} k}{e\hbar} \frac{T_e}{n_e^{1/2}}\right) \ , \qquad (29)$$

[a]Detail of the equations used to calculate $^4$He, $p$, and T densities as well as the charged particles power source in the case of a D-$^3$He mixture will be given in a separate paper together with an application to the design of a D-$^3$He reactor.

and

$$\gamma_{NC}(A,\rho) = \frac{1}{1 - \frac{1.95}{A^{1/2}}\rho^{1/2} + \frac{0.95}{A}\rho} \ .$$

*Loop Voltage*

At steady state, the condition $\nabla \times \boldsymbol{E} = \boldsymbol{0}$ gives a $1/R$ variation of the electric field according to

$$E = E_0 \frac{R_0}{R} \ , \tag{30}$$

where the subscript 0 refers to the geometrical axis position. Integration of Eq. (28) over the poloidal cross section gives

$$I_{OH} = E_0 \int_{S_p} \frac{1}{\eta} \frac{R_0}{R} \, dS_p \ .$$

The loop voltage $U_\ell = E_0 2\pi R_0$ is then given by

$$U_\ell = 2\pi R_0 \frac{I_{OH}}{\int_{S_p} \frac{1}{\eta} \frac{R_0}{R} \, dS_p}$$

$$= (1 - f_{NI}) 2\pi R_0 \frac{I_p}{\int_{S_p} \frac{1}{\eta} \frac{R_0}{R} \, dS_p} \ , \tag{31}$$

where $I_p$ is the total plasma current ($I_p = I_{OH} + I_{BS} + I_{CD}$) and $f_{NI}$ is the noninductive current fraction defined as

$$f_{NI} = \frac{I_{BS} + I_{CD}}{I_p} = f_{BS} + f_{CD} \ ,$$

where $I_{BS}$ and $I_{CD}$ are the bootstrap and current-driven currents, respectively; $\int_{S_p}(1/\eta(\rho))(R_0/R)\, dS_p$, where $\rho$ is the radial coordinate, is a double integral. In the frame of the present modeling for the magnetic surfaces representation, this integral may be reduced to a simple integral. The exact form of the simple integral depends on the nature of the conic fragments that compose the last magnetic surface. It is given in Appendix F.

*Ohmic Power*

In the presence of noninductive current densities (bootstrap and external current drive), the ohmic power density is

$$\frac{dP_{OH}}{dV} = Ej = E(j_{OH} + j_{NI}) \ , \tag{32}$$

where

$j_{OH}$ = ohmic current density

$j_{NI}$ = noninductive part of the current density.

Using Eq. (30), we have

$$P_{OH} = E_0 R_0 \int_V \frac{1}{R} j \, dV = E_0 R_0 \int_{S_p} 2\pi R \frac{1}{R} j \, dS_p$$

$$= 2\pi R_0 E_0 \int_{S_p} j \, dS_p \ ,$$

giving

$$P_{OH} = U_\ell I_p$$

(note that obtaining the above exact Ohm's law requires taking into account the $1/R$ variation of the electric field) or, in terms of the plasma current,

$$P_{OH} = (1 - f_{NI}) \frac{2\pi R_0}{\int_{S_p} \frac{1}{\eta} \frac{R_0}{R} \, dS_p} I_p^2 \ .$$

*II.G.3. Additional Power*

The additional power source $P_{add}$ is a constant in a 0-D model. It includes neutral beam injection (NBI) heating as well as high-frequency wave heating.

### II.H. Radiation Losses

*II.H.1. Bremsstrahlung Radiation Loss*

The nonrelativistic Born approximation is used for the electron-ion bremsstrahlung loss, i.e.,

$$P_B = \int_V C_B Z_{eff} n_e^2 T_e^{1/2} \, dV \ , \tag{33}$$

where

$$C_B = \frac{1}{(4\pi\varepsilon_0)^3} \frac{32\sqrt{2}}{3\sqrt{\pi}} \frac{e^6 k^{1/2}}{m_e^{3/2} c^3 \hbar} \simeq 5.355 \times 10^{-37} \ .$$

Introducing

$$C_B^*(n^*, T^*) = C_B \left( \frac{n_0}{\langle n \rangle} \right)^2 \left( \frac{T_0}{\langle T \rangle_n} \right)^{1/2} \frac{1}{V} \int_V n^{*2} T^{1/2} \, dV \ ,$$

we get

$$P_B(\langle n_e \rangle, \langle T_e \rangle_n) = C_B^* Z_{eff} \langle n_e \rangle^2 \langle T_e \rangle_n^{1/2} V \ .$$

In the special case of parabolic type density and temperature profiles as described in Eqs. (20) and (21), $C_B^*$ may be written in closed form, giving

$$C_B^* = C_B \frac{(1+\alpha_n)^{3/2}(1+\alpha_n+\alpha_T)^{1/2}}{1+2\alpha_n+\frac{\alpha_T}{2}} \times \frac{\left(1-\frac{\Theta_1}{A}\right)\left[1-\frac{\Theta_1}{A}\Gamma_1\left(2\alpha_n+\frac{\alpha_T}{2}\right)\right]}{\left[1-\frac{\Theta_1}{A}\Gamma_1(\alpha_n)\right]^{3/2}\left[1-\frac{\Theta_1}{A}\Gamma_1(\alpha_n+\alpha_T)\right]^{1/2}} \ .$$

The first part of the above expression is the classical form obtained in the approximation of infinite aspect ratio.

### *II.H.2. Synchrotron Radiation Loss*

The power loss due to synchrotron emission, taking into account reabsorption and partial reflection by the wall, is taken from Refs. 9 and 10, i.e.,

$$P_{syn} = 3.84\times10^{-9.6}\frac{(1-r_{syn})^{0.62}}{\left[1+0.12\frac{T_{e0}}{p_{a0}^{0.41}}(1-r_{syn})^{0.41}\right]^{1.51}} \times Ra^{1.38}\kappa_X^{0.79}B_t^{2.62}n_{e0}^{0.38}T_{e0}(16+T_{e0})^{2.61} \times K(\alpha_{n,syn},\alpha_{T,syn},\beta_{T,syn})G(A) \ ,$$

where $r_{syn}$ is the reflection coefficient of the wall for synchrotron radiation, $p_{a0}$ is defined as

$$p_{a0} = \frac{a\omega_{pe0}^2}{c\omega_{ce0}} = \frac{e}{c\varepsilon_0}\frac{an_{e0}}{B_t} \ ,$$

and $K$ is a profile correction factor:

$$K(\alpha_n,\alpha_T,\beta_T) = (\alpha_n+3.87\alpha_T+1.46)^{-0.79} \times (1.98+\alpha_T)^{1.36} \times \beta_T^{2.14}(\beta_T^{1.53}+1.87\alpha_T-0.16)^{-1.33} \ .$$

In Ref. 9, $K$ has been derived for a parabolic type electron density profile [as given in Eq. (20)] and a two-parameters electron temperature profile as given in Eq. (19) in the special case $\rho_{ped}=1$ and $T_{e,ped}=1$ keV. For the more general density and temperature profiles given by Eqs. (18) and (19) with arbitrary $\rho_{ped}$ and $T_{ped}$ pedestal values, we take

$$\alpha_{n,syn} = \alpha_n^* = \frac{n_{e0}}{\langle n_e\rangle} - 1 \ ; \qquad (34)$$

$\alpha_n^*$ is called the density peaking parameter. Note that $\alpha_n^*$ does not reduce exactly to $\alpha_n$ even in the case of a parabolic type density profile [as apparent in Eq. (D.1)] because of the nonzero $\Theta_1$ parameter.

For the evaluation of the $K$ function, the present version of HELIOS still uses $\beta_{T,syn}=\beta_T$ and $\alpha_{T,syn}=\alpha_T$, where $\beta_T$ and $\alpha_T$ are the parameters appearing in Eqs. (18) and (19). $G$ is an aspect ratio correction factor:

$$G(A) = 0.93[1+0.85\exp(-0.82A)] \ .$$

### *II.H.3. Line-Radiation Losses*

For a given impurity *Imp*, the total power lost per unit volume by all line-radiation processes (including bremsstrahlung) is

$$\frac{dP_{line,Imp}}{dV} = n_{Imp}n_eP_{line\text{-}LF,Imp}(n_e,T_e) = f_{Imp}n_e^2P_{line\text{-}LF,Imp}(n_e,T_e) \ ,$$

where $n_{Imp}$ is the density of the impurity ion and $f_{Imp}$ is the impurity fraction as defined in Eq. (22). $P_{line\text{-}LF,Imp}$ is called the radiative power loss function. For each impurity species, $P_{line\text{-}LF,Imp}$ is calculated from quantum mechanics codes and tabulated in the Atomic Data and Analysis Structure (ADAS) database[11] from which $P_{line\text{-}LF,\mathrm{Be}}$ (with $T_e$ in the range 0 to 20 keV) and $P_{line\text{-}LF,\mathrm{Ar}}$ (with $T_e$ in the range 0 to 340 keV) are taken for HELIOS. It appears that $P_{line\text{-}LF,Imp}$ is a weak function of electron density as illustrated in Fig. 3 for Be and Fig. 4 for Ar. This density dependence is neglected in HELIOS.

As total bremsstrahlung losses in the nonrelativistic Born approximation [Eq. (33)] have already been taken into account in the thermal equilibrium, we introduce the following $P_{line\text{-}core}$ term in Eq. (2):

$$P_{line\text{-}core} = \sum_{imp} P_{line\text{-}core,Imp} \ , \qquad (35)$$

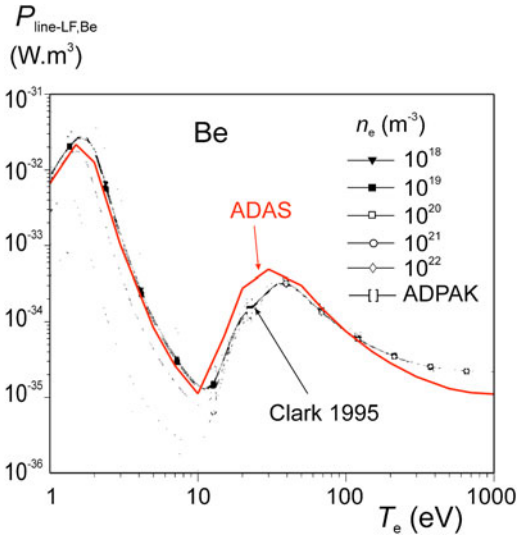


Fig. 3. Comparison of radiative power loss function for beryllium from ADAS database and from Clark et al.[12]

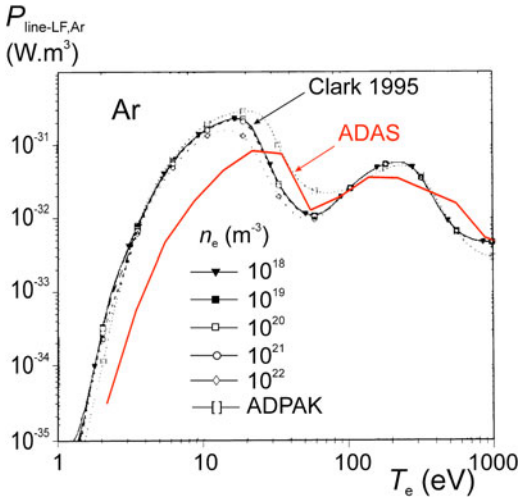


Fig. 4. Comparison of radiative power loss function for argon from ADAS database and from Clark et al.[12]

where

$$P_{line\text{-}core,\,Imp} = \int_{core} f_{Imp} n_e^2 [P_{line\text{-}LF,\,Imp}(T_e) - C_B Z_{Imp}^2 T_e^{1/2}]\, dV \ . \qquad (36)$$

For the plasma mantle, $P_{line\text{-}mantle}$ is defined in the same way.

No heavy impurity line-radiation loss is presently implemented in HELIOS. Tungsten losses will be considered in the next version.

### II.I. Transport Losses, Confinement Time Scaling Expressions

#### *II.I.1. Transport Losses*

If the energy confinement time is assumed to follow a scaling, Eq. (1) enables the conduction-convection term $P_{con}$ in Eq. (2) to be written as

$$P_{con} = \frac{W_{th}(n_e, T_e, n_{\rm He})}{\tau_{E,sc}(n_e, P_{net})} \ , \qquad (37)$$

where $\tau_{E,sc}$ is the confinement time scaling expression used to describe the transport losses of the plasma core. In the scaling expressions, $P_{net}$ is the so-called "net" power delivered to the plasma; it is defined as

$$P_{net} = P_{source} - (P_B + P_{syn} + P_{line\text{-}core}) \ ,$$

where

$$P_{source} = F_{P_\alpha} P_\alpha + P_{OH} + P_{add} \ , \qquad (38)$$

which means that at thermal equilibrium, we have

$$P_{con} = P_{net} \ . \qquad (39)$$

For the multispecies and multitemperature plasma considered here, the plasma thermal energy content is defined as

$$W_{th} = \int_V \left( \frac{3}{2} n_e k T_e + \sum_i \frac{3}{2} n_i k T_i \right) dV \ ,$$

where the summation is over all ion species. It may be rewritten as

$$W_{th}(\langle n_e \rangle, \langle T_e \rangle_n, f_{\rm He}) = C_W 3 \langle n_e \rangle k \langle T_e \rangle_n V \ , \qquad (40)$$

where $C_W$ is the "dilution + temperature ratio" coefficient for the energy content. For an arbitrary D-T mixture containing impurities with atomic number $Z_i$ and fraction $f_i$, $C_W$ may be written as

$$C_W = \frac{1+\theta_i}{2} - \frac{\theta_i}{2} \sum_{non\text{-}Hoid} (Z_i - 1) f_i \qquad (41)$$

or explicitly in the case of He and two light impurities:

$$C_W = \frac{1+\theta_i}{2} - \frac{\theta_i}{2} [\, f_{\rm He} + (Z_1 - 1) f_1 + (Z_2 - 1) f_2 ] \ .$$

#### *II.I.2. Confinement Time Scaling Expressions*

The confinement time scaling expressions give a fit of the experimentally measured $\tau_E$ in terms of the engineering parameters $M_{eff}$ (effective atomic mass of the ions), $\kappa_a$ (average elongation), $A$ (aspect ratio), $F_q$ (defined later), $I_p$ (plasma current), $B_t$ (magnetic field on the geometrical axis), $\bar{n}_e$ (line averaged electron density), $R$ (plasma major radius), and $P_{net}$. They are either monomial, two-term (sum of two monomial terms), or more general. As an illustration, we give below the explicit expressions for the ITER-97P(th) L-mode scaling[13] and the IPB98($y$,2) H-mode scaling,[6] which are both of the monomial form, and for the H-mode ITERH06-IP($y, dd$) scaling[7]:

$$\tau_{E,\text{ITER-97P}(th)} = C_{\tau,\text{ITER-97P}(th)} H_L M_{eff}^{0.2} \kappa_X^{0.64} A^{0.06} \times \frac{I_p^{0.96} (\bar{n}_e)^{0.4} B_t^{0.03} R^{1.83}}{P_{net}^{0.73}} \ , \qquad (42)$$

where $C_{\tau,\text{ITER-97P}(th)} = 2.3 \times 10^{-10.98} \simeq 2.41 \times 10^{-11}$;

$$\tau_{E,\text{IPB98}(y,2)} = C_{\tau,\text{IPB98}(y,2)} H_{98} \times \frac{M_{eff}^{0.19} \kappa_a^{0.78}}{A^{0.58}} \frac{I_p^{0.93} (\bar{n}_e)^{0.41} B_t^{0.15} R^{1.97}}{P_{net}^{0.69}} \ , \qquad (43)$$

where

$$C_{\tau,\mathrm{IPB98}(y,2)} = 5.62\times10^{-11.23} \simeq 3.31\times10^{-11} \ ;$$

and

$$\tau_{E,\mathrm{ITERH06\text{-}IP}(y,dd)} \simeq 7.3098\times10^{-7} H_{06} M_{eff}^{0.2} \kappa_a^{0.37} \times F_q^{0.77} A^{2.48205} A^{-0.9\ln A} \times \cdots \times \frac{I_p^{1.3678} (\bar{n}_e)^{0.032236} B_t^{0.12} R^{1.2345}}{P_{net}^{0.74}} \times \left(\frac{\bar{n}_e}{n_G}\right)^{-0.22\ln(\bar{n}_e/n_G)} , \quad (44)$$

where $\kappa_X$ is defined in Eq. (12) and $\kappa_a$ is the average elongation defined as

$$\kappa_a = \frac{V}{2\pi^2 R a^2} \ .$$

According to Eq. (13), we have

$$\kappa_a = \kappa_X \Theta_V \ .$$

The shape parameter $F_q$ (reflecting essentially the triangularity dependence) is defined as

$$F_q = \frac{q_{95}}{q_{cyl}} \ ,$$

where

$$q_{cyl} = \frac{2\pi}{\mu_0} \kappa_a \frac{B_t a^2}{R I_p} \ .$$

In contrast to purely monomial scaling expressions, we see that the ITERH06-IP$(y,dd)$ scaling retains $\ln^2 A$ and $\ln^2(\bar{n}_e/n_G)$ terms in the fit for $\ln\tau_E$.

In Eqs. (42), (43), and (44), $H$ is the so-called enhancement factor (relative to L- or H-mode) used to describe improved confinement regimes. Strictly speaking, the referred confinement time scalings are defined with $H = 1$. The $H$ dependence has been included here to simplify the presentation of the $H$ dependence modification when the confinement time is expressed in terms of $\langle T_e\rangle_n$ (see below).

*Expression of the Confinement Time in Terms of the Averaged Temperature*

In the case of a monomial $P_{net}$ dependence, Eqs. (42), (43), and (44) may be rewritten identically in terms of the average temperature $\langle T_e\rangle_n$ by solving the equation

$$P_{net} = \frac{C_W 3\langle n_e\rangle k \langle T_e\rangle_n V}{\tau_{E,sc}(\bar{n}_e, P_{net})} \quad (45)$$

obtained from Eqs. (37), (39), and (40), which yields $P_{net}(\langle T_e\rangle_n)$. In the case of a purely monomial scaling, the explicit result is given in Appendix G for arbitrary exponents. In the special case of IPB98$(y,2)$ scaling, it reads

$$\tau_{E,\mathrm{IPB98}(y,2)} = C_{\tau 1} H_{98}^{1/0.31} \frac{(\bar{n}/\langle n\rangle)^{0.69/0.31}}{C_W^{0.69/0.31}} \times M_{eff}^{0.19/0.31} \kappa_a^{0.09/0.31} A^{0.8/0.31} \times \frac{I_p^3 (\bar{n}_e)^{-(0.28/0.31)} B_t^{0.15/0.31} R^{-(0.1/0.31)}}{\langle T_e\rangle_n^{0.69/0.31}} ,$$

where

$$C_{\tau 1} = \frac{(5.62\times10^{-11.23})^{1/0.31}}{(6\pi^2 k)^{0.69/0.31}}$$

or, approximately,

$$\tau_{E,\mathrm{IPB98}(y,2)} \simeq 2.54\times10^{-3} H_{98}^{3.23} \frac{(\bar{n}/\langle n\rangle)^{2.23}}{C_W^{2.23}} \times M_{eff}^{0.613} \kappa_a^{0.290} A^{2.58} \times \frac{I_p^3 B_t^{0.484}}{(\bar{n}_e)^{0.903} R^{0.323}} \frac{1}{\langle T_e\rangle_n^{2.23}} \ .$$

The above expression shows the strong temperature degradation ($1/\langle T_e\rangle_n^{2.23}$) of the confinement time and the strong favorable dependence in $I_p$. Also notable is the $H_{98}^{3.23}$ dependence of the confinement time when comparing plasmas with the same density and temperature.

It is also interesting to compare the confinement time for plasmas with the same $q_{95}$ and same normalized density $n_N = \bar{n}_e/n_G$. In this case,

$$\tau_{E,\mathrm{IPB98}(y,2)} = C_{\tau 2} H_{98}^{1/0.31} \frac{(\bar{n}/\langle n\rangle)^{0.69/0.31}}{C_W^{0.69/0.31}} \times M_{eff}^{0.19/0.31} \frac{\kappa_a^{0.74/0.31} F_q^{0.65/0.31}}{A^{1.06/0.31}} \times \frac{n_N^{-(0.28/0.31)} B_t^{0.8/0.31} R^{1.11/0.31}}{q_{95}^{0.65/0.31} \langle T_e\rangle_n^{0.69/0.31}} ,$$

where

$$C_{\tau 2} = \frac{10^{-14(0.28/0.31)}}{\pi^{-(0.28/0.31)}} \left(\frac{2\pi}{\mu_0}\right)^{0.65/0.31} \times \frac{(5.62\times10^{-11.23})^{1/0.31}}{(6\pi^2 k)^{0.69/0.31}}$$

or, approximately,

$$\tau_{E,\mathrm{IPB98}(y,2)} \simeq 0.180 H_{98}^{3.23} \frac{(\bar{n}/\langle n\rangle)^{2.23}}{C_W^{2.23}} \times M_{eff}^{0.613} \frac{\kappa_a^{2.39} F_q^{2.10}}{A^{3.42}} \frac{B_t^{2.58} R^{3.58}}{n_N^{0.903} q_{95}^{2.10} \langle T_e\rangle_n^{2.23}} \ .$$

In the above expression, the strong increase of the confinement time with magnetic field ($B_t^{2.58}$) and dimension ($R^{3.58}$) becomes apparent, when comparing plasmas with the same aspect ratio, normalized density, edge safety factor, and averaged temperature.

### II.J. Calculation of the Helium Content

For a 50-50 D-T mixture, the helium source in Eq. (3) is given by

$$S_{\mathrm{He}} = C_\alpha \frac{\langle n_e\rangle^2}{4} \overline{\sigma v}^*_{\mathrm{DT}}(\langle T_e\rangle_n) V \ .$$

The apparent helium confinement time is supposed to be proportional to the energy confinement time:

$$\frac{\tau^*_{\mathrm{He}}}{\tau_E} = \mathrm{const} \ .$$

This assumption is a consequence of the observed link between the thermal diffusivity $\chi$ and the particle diffusion coefficient $D$. It has replaced the explicit data of He fraction in most 0-D codes. In all the applications considered in this paper, $\tau^*_{\mathrm{He}}/\tau_E = 5$ is taken. Imposing the $\tau^*_{\mathrm{He}}/\tau_E$ ratio, Eqs. (2) and (3) may be reduced to a single equation for the He fraction $f_{\mathrm{He}}$. The explicit form of this equation is given in Appendix H.

### II.K. The Operating Window and the POpCon Representation

Physics and technological constraints impose limits in the operating space of a tokamak. A convenient way to present results of a 0-D code is to plot iso-value contours in the $(n_e, T_e)$ space for a given parameter $(Q, P_{fus}, \beta_N, \ldots)$. Let us consider, for example, operation with a given $Q$. Equation (2) with $P_{OH} + P_{add}$ replaced with $P_{fus}/Q$ together with Eq. (3) give two relations between $n_e$, $T_e$, and $n_{\mathrm{He}}$. Formal elimination of $n_{\mathrm{He}}$ then yields a relation $F(n_e, T_e, Q) = 0$. Zero iso-value contours of $F$ for a given $Q$ value may be plotted in the $(n_e, T_e)$ plane. Such plots are called Plasma Operation Contours[14] (POpCon) plots. In such a representation, physics and technological constraints delimit an accessible window (white part of the plots in this paper).

#### *II.K.1. Density Limit*

The condition on the density limit is taken to be

$$\bar{n}_e < n_G \ , \quad \text{with } n_G = 10^{14} \frac{I_p}{\pi a^2} \ ,$$

where $n_G$ is the Greenwald density limit ($I_p$ is expressed in $A$ according to the convention described in Sec. I). The Greenwald density limit is not a hard barrier, but most of the discharges with $\bar{n}_e > n_G$ have degraded energy confinement.

#### *II.K.2. Beta Limit*

Iso-value curves of the $\beta_N$ parameter can be plotted by HELIOS. $\beta_N$ is a normalization of the toroidal beta parameter defined as

$$\beta_t = 10^{-8} \beta_N \frac{I_p}{a B_t} \ ,$$

where $\beta_t$ is the toroidal beta parameter defined as

$$\beta_t = \frac{\langle p_{th}\rangle + \langle p_\alpha\rangle}{B_t^2/(2\mu_0)} \ ,$$

where $p_{th}$ and $\langle p_{th}\rangle$ are the local and volume averaged thermal pressures, respectively. We have

$$p_{th} = n_e k T_e + \sum_i n_i k T_i$$

and

$$\langle p_{th}\rangle = C_W 2 \langle n_e\rangle k \langle T_e\rangle_n \ , \tag{46}$$

where $C_W$ is the same coefficient as defined in Eq. (41). $\langle p_\alpha\rangle$ is the fast alpha pressure. The fit in Ref. 15 is taken:

$$p_\alpha = \frac{C_{\tau\alpha} E_\alpha}{6} C_\alpha \frac{n_e T_e^{3/2}}{\ln\Lambda} \overline{\sigma v}_{\mathrm{DT}}(T_i) U_\alpha(T_e) \ ,$$

where $\ln\Lambda$ is defined in Eq. (29) and

$$C_{\tau\alpha} = \frac{3\sqrt{2}\pi^{3/2}\varepsilon_0^2 m_\alpha k^{3/2}}{m_e^{1/2} Z_\alpha^2 e^4}$$

and

$$U_\alpha(T_e) = 1 - \frac{T_e}{50} + 0.37\left(\frac{T_e}{50}\right)^{7/4} \ ,$$

where $m_\alpha$ and $Z_\alpha$ are the mass and charge of the alpha particle, respectively. $\beta_{N,th}$ is also used in connection with the thermal pressure only.

For discharges with $q_0 < 1$ (inductive operation with sawtooth activity), destabilization of neoclassical tearing modes (NTMs) may occur for $\beta_N \sim 2$. For discharges with $q_0 > 1$ (hybrid and advanced operation with no

sawtooth activity), $\beta_N$ is limited by ideal magnetohydrodynamic (MHD) ($\beta_N \sim 4\ell_i$).

*II.K.3. L-H Transition*

The existence of the H-mode is expressed as a condition of the following form:

$$P_{sep} > P_{L\text{-}H} \ ,$$

where $P_{sep}$ is the power crossing the separatrix. $P_{sep}$ is defined as

$$P_{sep} = P_{con} - P_{line\text{-}mantle} \ ,$$

where $P_{line\text{-}mantle}$ is defined as $P_{line\text{-}core}$ in Eqs. (35) and (36) with "core" replaced with "mantle." $P_{L\text{-}H}$ is a scaling expression for the threshold power required for the plasma to stay in H-mode. The more recently implemented scaling expression for $P_{L\text{-}H}$ is the Martin scaling [Eq. (2) of Ref. 16]:

$$P_{L\text{-}H,Martin08} = C_{Martin08} \frac{(\bar{n}_e)^{0.717} B_t^{0.803} S^{0.941}}{M_{eff}} \ ,$$

where $C_{Martin08} = 0.0976 \times 10^{-8.34} \simeq 4.46 \times 10^{-10}$.

Degradation of the confinement time occurs when $P_{sep}$ gets close to $P_{L\text{-}H}$. It is generally considered that good H-mode confinement requires $P_{sep} \geq 1.3 \times P_{L\text{-}H}$.

*II.K.4. Maximum Available Additional Power*

Of course, the operating window is limited by the maximum additional power available in the machine. This curve is also represented in POpCon plots.

*II.K.5. Thermal Load on the Divertor Plates*

The time averaged peak thermal load on the divertor plates is limited by technology (to ~10 MW/m$^2$). This load is calculated using the following expression[17]:

$$q_{peak} = 1.02 \times 10^{30} \frac{1}{n_{e,sep}^{1.82}} \left( \frac{P_{non\text{-}rad}}{S} \right)^{2.37} q_{95}^{0.52} R^{0.33} \ , \tag{47}$$

where $n_{e,sep}$ is the electron density at the midplane separatrix and $P_{non\text{-}rad}$ is the nonradiated power defined as

$$P_{non\text{-}rad} = P_{source} - (P_B + P_{syn} + P_{line\text{-}tot}) \ ,$$

where $P_{source}$, defined in Eq. (38), is the total power delivered to the plasma and $P_{line\text{-}tot}$ is the total power lost by line-radiation processes in the plasma bulk, scrape-off-layer, and divertor. This power is supposed to be given by the Matthews scaling[18]:

$$P_{line\text{-}tot} = \frac{10^{-31.8}}{4.5} (\bar{n}_e)^{1.89} S^{0.94} \frac{Z_{eff} - 1}{Z_r^{0.12}} \ ,$$

where $Z_r$ is the atomic number of the main radiative impurity (Ar in the applications considered in the present paper). The constant in Eq. (47) has been adjusted to get $q_{peak} = 7$ MW/m$^2$ for $P_{sep} = 86$ MW in ITER-FDR scenario 1 according to B2-Eirene calculations in Ref. 19.

In addition to accepting the above average thermal load, the divertor must be designed to withstand thermal peaks due to edge-localized modes[20] (ELMs) (if ELM activity cannot be mitigated in the chosen scenario). Such a constraint is not considered in the present modeling.

The above modeling, using the relatively imprecise Matthews scaling, is a first simple approach for the description of $q_{peak}$ in HELIOS. More elaborate modelings, such as those described in Ref. 5 or 21, will be considered in the next version. For this reason, the $q_{peak} = 10$ MW/m$^2$ limit in the POpCon plots must be considered as indicative.

### II.L. Additional Features

*II.L.1. Pedestal Temperature and Width*

*Pedestal Temperature Scaling*

The electron temperature at the pedestal may be either given or calculated from a scaling. In Ref. 22, scalings are proposed for the following quantity:

$$W_{ped,Cor03} = C_{Cor03} 3 n_{e,ped} k T_{e,ped} V \ , \tag{48}$$

where $C_{Cor03} = 0.92$.

Equation (4) of Ref. 22 gives a scaling relationship between the parameters $\beta_{ped}$, $T_{pav}$, $\rho^*_{ped}$, and $\nu^*_{ped}$. Using the following definitions:

$$\beta_{ped} = \frac{W_{ped,Cor03}\,(\mathrm{MJ})}{R I_p^2\,(\mathrm{MA})} \ ,$$

$$T_{pav}\,(\mathrm{keV}) = 2 \times 10^2 \frac{W_{ped,Cor03}\,(\mathrm{MJ})}{C_{Cor03} V n_{e,ped}\,(10^{19}\ \mathrm{m}^{-3})} \ ,$$

$$\rho^*_{ped} = \frac{T_{pav}^{1/2}\,(\mathrm{keV})}{I_p\,(\mathrm{MA})} \ ,$$

and

$$\nu^*_{ped} = \frac{n_{e,ped}\,(10^{19}\ \mathrm{m}^{-3}) R}{T_{pav}^2\,(\mathrm{keV})}$$

and the definition in Eq. (48), we can derive the following scaling for $T_{e,ped}$:

$$T_{e,ped,Cor03(4)} = \frac{\overline{8.33}^{1/0.705} \times 10^{-(2.435/0.705)}}{6 \times \pi^{2/0.705} C_{Cor03}^{1/0.705}} \frac{1}{k} M_{eff}^{0.2/0.705} \times \kappa_a^{1.48/0.705} F_q^{2.29/0.705} \frac{A^{4.56/0.705} I_p^{1.73/0.705}}{R^{2.08/0.705} n_{e,ped}^{1.08/0.705}} \ . \tag{49}$$

The above scaling will be used in all the applications proposed in Sec. IV.

*Pedestal Width*

The pedestal width $\Delta_{ped}$ (or equivalently $\rho_{ped}$) may be either given or calculated in the HELIOS code. When the pedestal width is calculated, it is obtained assuming that the pedestal is at the ballooning stability limit. The following simplified criterion for ballooning stability is taken:

$$\left|\frac{dp}{dr}\right|_{\max} < \left|\frac{dp}{dr}\right|_{balloon} , \quad \text{with} \left|\frac{dp}{dr}\right|_{balloon} = 2.47\times 10^6 \frac{B_t^2}{Rq_{95}^2} , \tag{50}$$

where the constant has been adjusted to give results in accordance with measured values in DIII-D (Ref. 23).

For linear shape of density and temperature profiles in the pedestal, the maximum pressure gradient is obtained for $\rho = \rho_{ped}$ giving

$$\left|\frac{dp}{dr}\right|_{\max} = \left|\frac{dp}{dr}\right|_{ped} = \left(2 - \frac{n_{e,sep}}{n_{e,ped}} - \frac{T_{e,sep}}{T_{e,ped}}\right)\frac{2C_W n_{e,ped} kT_{e,ped}}{\Delta_{ped}} . \tag{51}$$

For given $\langle n_e\rangle$ and electron density profile ($\alpha_n$, $n_{e0}/n_{e,ped}, n_{e,sep}$), $n_{e,ped}$ can be calculated. $T_{e,ped}$ is then obtained from the scaling in Eq. (49), and $\Delta_{ped}$ is derived from Eqs. (50) and (51).

*II.L.2. Bootstrap Current*

The bootstrap current fraction defined as

$$f_{BS} = \frac{I_{BS}}{I_p}$$

is supposed to be given by the following relation:

$$f_{BS} = \frac{\beta_{p,th}}{A^{1/2}} B(prof, shape, imp) ,$$

where $\beta_{p,th}$ is the thermal poloidal beta defined as

$$\beta_{p,th} = \frac{\langle p_{th}\rangle}{\langle\langle B_p\rangle\rangle^2/(2\mu_0)} , \quad \text{with} \langle\langle B_p\rangle\rangle = \frac{\int_L B_p\, d\ell}{L} ,$$

where $\langle p_{th}\rangle$ is the volume averaged pressure given in Eq. (46). $\langle\langle B_p\rangle\rangle$ is the average of the poloidal component of the magnetic field along the LCMS. Using

$$\int_L B_p\, d\ell = \mu_0 I_p ,$$

$\beta_{p,th}$ may also be written as

$$\beta_{p,th} = \frac{4}{\mu_0} C_W \frac{\langle n_e\rangle k\langle T_e\rangle_n}{I_p^2} L^2 . \tag{52}$$

The $B$ function depends on density, temperature and current profiles, plasma shape, and impurity contents. The Wilson fit[24] and the following simple Hoang fit have been implemented in HELIOS:

$$B_{Hoang}(\alpha_p^*, \alpha_j) = 0.45\sqrt{\frac{1+\alpha_p^*}{1+\alpha_j}} ,$$

where $\alpha_p^*$ is the thermal pressure peaking parameter defined in the same way as $\alpha_n^*$ in Eq. (34), i.e.,

$$\alpha_p^* = \frac{p_{th0}}{\langle p_{th}\rangle} - 1 , \quad \text{with } p_{th0} = 2C_W n_{e0} kT_{e0} ,$$

and $\alpha_j$ is an ad hoc current density peaking parameter.

*II.L.3. Current Drive*

In the present version of HELIOS, the total additional power $P_{add}$ is divided into three parts: $P_{add,noCD}$, $P_{add,CD,1}$, and $P_{add,CD,2}$. $P_{add,noCD}$ is the part of the additional power that drives no current (pure heating in the case of balanced NBI, for example). $P_{add,CD,1}$ is a part of the additional power that drives a current with an efficiency $\gamma_{CD,1}$ (for example, NBI current drive). $P_{add,CD,2}$ is a part of the additional power that drives a current with an efficiency $\gamma_{CD,2}$ (for example, electron cyclotron current drive). The following relations hold:

$$P_{add} = P_{add,noCD} + P_{add,CD,1} + P_{add,CD,2}$$

and

$$I_{CD} = \frac{\gamma_{CD,1}}{\langle n_e\rangle R} P_{add,CD,1} + \frac{\gamma_{CD,2}}{\langle n_e\rangle R} P_{add,CD,2} .$$

Different expressions for the current drive efficiencies of the main current drive methods have been implemented in HELIOS. For the application to DEMO, the following simple fit for the negative NBI current drive efficiency will be considered ($\langle T_e\rangle$ in keV):

$$\gamma_{CD,\mathrm{NBI}} = 0.035\times 10^{20}\langle T_e\rangle . \tag{53}$$

In Fig. 5, comparison of Eq. (53) with experimental and theoretical results for NBI current drive efficiency is shown.

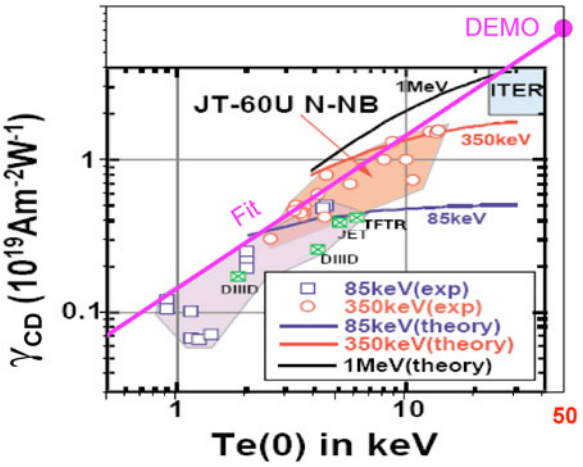


Fig. 5. Comparison of the fit in Eq. (53) with experimental and theoretical results for NBI current drive efficiency[25] assuming $T_e(\rho) = T_{e0}(1-\rho^2)^{1.5}$.

### *II.L.4. Inductive Discharge Duration*

The maximum duration $\Delta t_{pl}$ of an inductive discharge is obtained from the following equation:

$$\Phi_{CS} + \Phi_{VF} = \Phi_{PI} + \Phi_{RU} + U_\ell \, \Delta t_{pl} \ ,$$

where

$\Phi_{CS}$ = magnetic flux stored in the central solenoid

$\Phi_{VF}$ = flux stored in the vertical field

$\Phi_{PI}$ = flux consumed during plasma initiation

$\Phi_{RU}$ = flux consumed during the ramp-up phase

$U_\ell$ = plateau loop voltage.

*Central Solenoid*

Assuming a constant current density in the central solenoid windings, it can be shown that

$$\Phi_{CS} = \frac{2\pi}{3} B_{CS,\max}(R_{CS,i}^2 + R_{CS,i} R_{CS,e} + R_{CS,e}^2) \ ,$$

where $B_{CS,\max}$ is the maximum magnetic field in the inner part of the central solenoid. This field is supposed to be given. $R_{CS,i}$ and $R_{CS,e}$ are the internal and external radii, respectively, of the central solenoid. The above expression takes into account the linear increase of the magnetic field due to the constant current density and the doubling effect due to complete inversion of the magnetic field in the central solenoid. $R_{CS,e}$ and $R_{CS,i}$ are calculated from the following radial build relations:

$$R_{CS,e} = R - a - \Delta_{\text{int}} - d_{TFC} - gap$$

and

$$R_{CS,i} = R_{CS,e} - d_{CS} \ ,$$

where

$\Delta_{\text{int}}$ = distance between the inner plasma surface and the plasma facing side of the superconducting winding of the toroidal field coil

$d_{TFC}$ = radial width of the toroidal field coil

$gap$ = gap between the toroidal field coil and the central solenoid

$d_{CS}$ = radial width of the central solenoid.

The following relation holds:

$$d_{CS} = \frac{B_{CS,\max}}{\mu_0 j_{CS}} \ ,$$

where $j_{CS}$ is the average current density in the central solenoid coil chosen for the machine design.

*Vertical Field*

A preliminary modeling for the available part of the vertical field flux is

$$\Phi_{VF} = \pi(R^2 - R_{CS,e}^2) B_V \ ,$$

where[26]

$$B_V = \frac{\mu_0 I_p}{4\pi R}\left(\beta_{p,th} + \frac{\ell_i}{2} - \frac{3}{2} + \ln\frac{8A}{\sqrt{\kappa_{95}}}\right) \ ,$$

where $\ell_i$ is the plasma internal inductance.

*Plasma Initiation*

$\Phi_{PI}$ is a given constant.

*Current Ramp-Up*

Flux consumption during current ramp-up is

$$\Phi_{RU} = \Phi_{res} + \Phi_{ind} \ ,$$

where $\Phi_{res}$ and $\Phi_{ind}$ are the resistive and inductive flux consumption, respectively. We take

$$\Phi_{res} = C_E \, \mu_0 R I_p \ ,$$

where $C_E$ is the so-called Ejima constant ($C_E = 0.45$ is taken for the applications). We assume

$$\Phi_{ind} = L_p I_p \ ,$$

with

$$L_p = 1.07\mu_0 R(1 + 0.1\beta_{p,th})\left(\frac{\ell_i}{2} - 2 + \ln\frac{8A}{\sqrt{\kappa_{95}}}\right) \ ,$$

where $\beta_{p,th}$ is given in Eq. (52) and expression of $L_p$ is slightly modified with respect to Ref. 26.

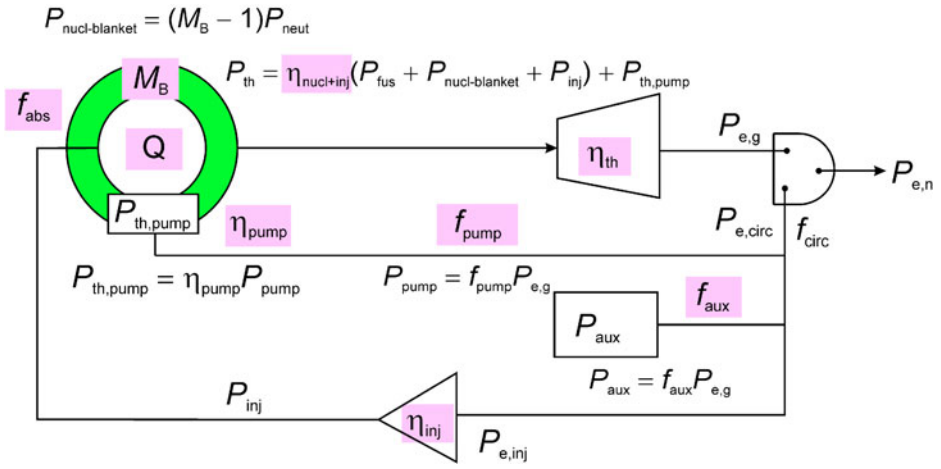


Fig. 6. Power balance of a thermonuclear power plant.

*Loop Voltage*

The plateau loop voltage $U_\ell$ is supposed to be the loop voltage corresponding to a completely relaxed electric field. It is given in Eq. (31). Note that the loop voltage is zero when $f_{NI} = 1$.

*II.L.5. Average Neutron Flux at the Plasma Surface*

As an approximation to neutron wall load, the average neutron flux at the plasma surface is calculated:

$$\Gamma_n = \frac{N_{\rm DT} E_n}{S} \quad ,$$

where

$N_{\rm DT}$ = total number of D-T reactions [Eq. (27)]

$E_n$ = neutron energy.

For a 50-50 D-T mixture, we get

$$\Gamma_n = C_\alpha \frac{\langle n_e \rangle^2}{4} \overline{\sigma v}^*_{\rm DT} E_n \frac{V}{S} \quad .$$

*II.L.6. Maximum Magnetic Field Inside the Superconducting Windings*

The relation between $B_t$ and the maximum magnetic field in the superconducting windings $B_{t,\max}$ is

$$\frac{B_{t,\max}}{B_t} = k_{B_{t,\max}} \frac{1}{1 - \frac{1}{A} - \frac{\Delta_{\rm int}}{R}} \quad , \qquad (54)$$

where $k_{B_{t,\max}}$ is a correction factor (close to one) taking into account the ripple effect due to the finite number of toroidal field coils.

In reactor studies, relation (54) allows the calculation of $B_t$ in terms of given $B_{t,\max}$, $A$, and $\Delta_{\rm int}$.

## III. PLASMA ENERGY GAIN AND POWER PLANT BALANCE MODELING

### III.A. Plasma Energy Gain

In HELIOS, the plasma energy gain $Q$ is defined as the ratio of the total fusion power $P_{fus}$ to the total external power $P_{ext} = P_{OH} + P_{add}$ coupled to the plasma:

$$Q = \frac{P_{fus}}{P_{OH} + P_{add}} \quad .$$

Note that, with the above definition, $Q$ is large but not infinite in the case of ohmic ignition ($P_{add} = 0$, $P_{OH} \neq 0$).

### III.B. Power Plant Balance Modeling

The power plant power diagram considered in HELIOS is represented in Fig. 6. $f_{abs}$ is the fraction of the injected power that is effectively absorbed by the plasma, $M_B$ is the blanket neutron energy gain, and $P_{neut}$ and $P_{fus}$ are the neutron and total fusion power generated inside the plasma, respectively:

$$P_{neut} = N_{\rm DT} E_n \quad ; \quad P_{fus} = N_{\rm DT}(E_\alpha + E_n) \quad ,$$

where $N_{\rm DT}$ is defined in Eq. (27). $P_{th}$ is the high-grade thermal power used to generate electricity, $\eta_{nucl+inj}$ is the fraction of the nuclear plus injected power that is converted into useful heat, $\eta_{th}$ is the thermodynamic cycle efficiency of the generator of electricity ($P_{e,g} = \eta_{th} P_{th}$), $f_{circ}$ is the fraction of the gross electrical output that is recirculated, $\eta_{inj}$ is the electrical efficiency of the power injector, $f_{pump}$ is the fraction of the gross electrical output $P_{e,g}$ used to energize the pumping system, $P_{e,n} = (1 - f_{circ})P_{e,g}$ is the net electrical power delivered to the network, $\eta_{pump}$ is the fraction of $P_{pump}$ that is converted

into useful heat, and $f_{aux}$ is the fraction of the gross electrical output used to energize the auxiliary equipment (including the cryogenic plant).

For a plasma with a given amplification factor $Q$, the required recirculated fraction may be shown to be

$$f_{circ} = f_{pump} + f_{aux} + \frac{1 - \eta_{th}\eta_{pump}f_{pump}}{\eta_{nucl+inj}\eta_{th}\eta_{inj}(1 + f_{abs}A_B Q)} \ ,$$

where

$$A_B = \frac{P_{fus} + P_{nucl\text{-}blanket}}{P_{fus}} = \frac{E_\alpha + M_B E_n}{E_\alpha + E_n} \ .$$

In the same way, if we want a given recirculated fraction $f_{circ}$, the plasma amplification factor $Q$ must be

$$Q = \frac{1}{f_{abs}A_B}\left[\frac{1 - \eta_{th}\eta_{pump}f_{pump}}{\eta_{nucl+inj}\eta_{th}\eta_{inj}(f_{circ} - f_{pump} - f_{aux})} - 1\right] . \tag{55}$$

The following expressions for $P_{e,n}$, $P_{e,g}$ in terms of $P_{fus}$ and $Q$ are obtained:

$$P_{e,n} = \frac{(1 - f_{pump} - f_{aux})\eta_{nucl+inj}\eta_{th}\eta_{inj}(1 + f_{abs}A_B Q) - (1 - \eta_{th}\eta_{pump}f_{pump})}{f_{abs}\eta_{inj}Q(1 - \eta_{th}\eta_{pump}f_{pump})} P_{fus}$$

and

$$P_{e,g} = \frac{P_{e,n}}{1 - f_{circ}} = \frac{\eta_{nucl+inj}\eta_{th}(1 + f_{abs}A_B Q)}{f_{abs}Q(1 - \eta_{th}\eta_{pump}f_{pump})} P_{fus} \ .$$

The global power plant efficiency, defined as

$$\eta_{PP} = \frac{P_{e,n}}{P_{fus} + P_{nucl\text{-}blanket}} \ ,$$

where the denominator is the total nuclear power generated by the installation, may be shown to be

$$\eta_{PP} = \frac{(1 - f_{pump} - f_{aux})\eta_{nucl+inj}\eta_{th}\eta_{inj}(1 + f_{abs}A_B Q) - (1 - \eta_{th}\eta_{pump}f_{pump})}{f_{abs}\eta_{inj}A_B Q(1 - \eta_{th}\eta_{pump}f_{pump})} \ .$$

It is also interesting to express $\eta_{PP}$ in terms of $f_{circ}$ using Eq. (55):

$$\eta_{PP} = \frac{1 - f_{circ}}{1 - \eta_{th}\eta_{pump}f_{pump} - \eta_{nucl+inj}\eta_{th}\eta_{inj}(f_{circ} - f_{pump} - f_{aux})} \eta_{nucl+inj}\eta_{th} \ .$$

As an illustration, the power plant efficiencies used for the DEMO-2007 project[27] will be considered, i.e.,

$$f_{abs} = 100\% \ , \quad M_B = 1.18 \ , \quad \eta_{nucl+inj} = 93.6\% \ , \quad \eta_{pump} = 91\% \ , \quad \eta_{th} = 44\% \ ,$$

$$f_{pump} = 21.4\% \ , \quad f_{aux} = 2.39\% \ , \quad \eta_{inj} = 60\% \ . \tag{56}$$

It is important to outline the large fraction of the gross electrical power used to energize the pumping system (characteristic of helium cooling) and the large fraction of this power that is converted into useful heat. The above values will also be taken in the applications to DEMO and to a purely inductive reactor discussed in Sec. IV.

For the above power plant parameters, the curves in Fig. 7 are obtained for $f_{circ}$, $P_{e,n}$, and $\eta_{PP}$ as a function of $Q$. The $P_{e,n}$ curve has been plotted taking the value $P_{fus} =$ 2401 MW of Ref. 27. The particular values obtained for $Q = 13.2$ (Ref. 27) are also given. The dashed lines correspond to the values that would be obtained with ignited operation ($Q = \infty$).

For the relatively low $Q$ amplification factor considered in Ref. 27, we see that the recirculated fraction is high (46.8%); consequently, the network electrical output

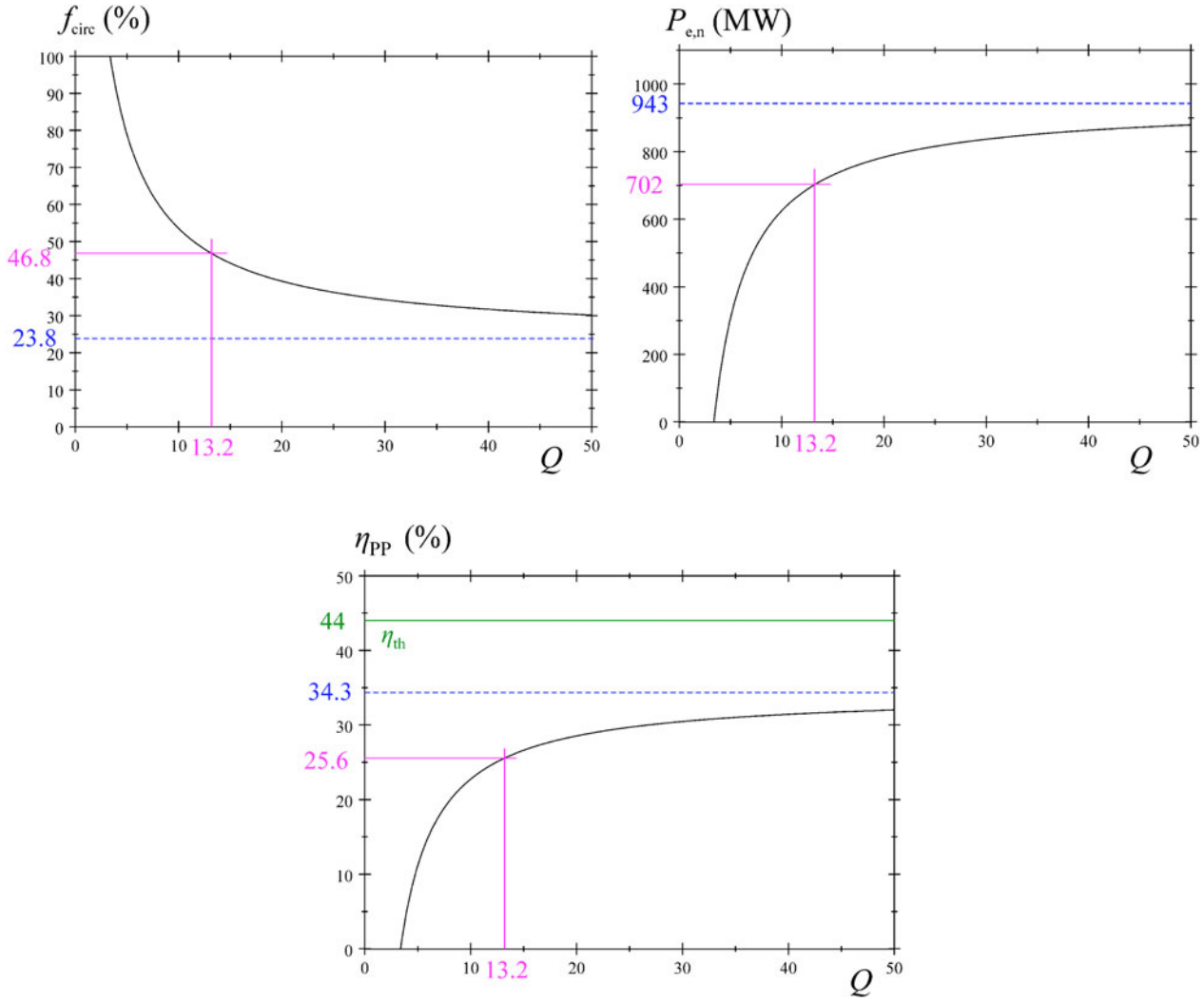


Fig. 7. Recirculated fraction, network electrical power, and power plant efficiency as a function of $Q$ with the power plant parameters given in Eq. (55).

is low (702 MW compared to $P_{e,g} \simeq 1320$ MW), and the power plant efficiency (25.6%) exhibits a very strong reduction with respect to the thermodynamic efficiency of the electricity generator (44%).

## IV. EXAMPLES OF APPLICATION

In this section, to demonstrate the use of the code, examples of its application to ITER, to DEMO, and to a purely inductive reactor are given.

For ITER (Ref. 28), the scenario 2 inductive operation with IPB98($y$,2) scaling and full magnetic field is first considered. The effect of a 10% reduction of the toroidal field, keeping the same confinement scaling and the same edge safety factor, is then treated. The effect of using the ITERH06-IP($y, dd$) confinement time scaling for scenario 2 is also analyzed.

For DEMO, noninductive advanced operation ($H_{98} = 1.5$) in the PPCS-C project [3] is considered. The Ar fraction is adjusted to obtain a fully noninductive operating point at the Greenwald density limit with the maximum power load on the divertor plates. For the calculation of the electrical power delivered to the network, account is taken of the large recirculated power required to energize the helium pumping system. The same study is also performed in the DEMO-2007 version characterized by a slightly lower magnetic field and $H_{98} = 1.3$.

Finally, a preliminary design of a pure H-mode ($H_{98} = 1$), purely inductive ITER-like 1-GW(electric) reactor is performed. Constraints on the density, thermal load on the divertor plates, and network electrical power lead to a large ($R = 10$ m) machine.

### IV.A. ITER Inductive Operation in H-Mode

#### *IV.A.1. ITER Scenario 2 Inductive Operation with IPB98(y,2) Scaling*

The ITER machine with the scenario 2 parameters listed in Table I (Ref. 29) is considered. For the description of the LCMS, the parameters listed in Table II are taken. These parameters have been directly measured in the drawing of Fig. 8 showing the ITER scenario 2 operating point MHD equilibrium. The LCMS reconstructed from the HELIOS modeling with four portions of conics is represented as a solid line (in red in online electronic version). It shows good agreement.

With the above data, the following global parameters obtained with HELIOS are listed in Table III and compared to the ones of Ref. 29. It can be seen that the geometrical modeling in HELIOS performs very well.

For the pedestal width and the core plasma definition, we take

$$\rho_{ped} = 0.925 \ , \quad \rho_{core} = 0.95 \ .$$

We suppose a flat density profile characterized by

$$\frac{n_{e0}}{n_{e,ped}} = 1.023 \ . \tag{57}$$

For a given value of the volume averaged density $\langle n_e \rangle$, the above condition together with the value of $n_{e,sep}$ and the density profile described in Eq. (18) allows the calculation of $n_{e,ped}$. Concerning the temperature profile, $T_{e,ped}$ is given by Eq. (49) with the above value of $n_{e,ped}$.

TABLE I

ITER Scenario 2 Parameters

| | | | |
|---|---|---|---|
| $R$ (m) | 6.2 | $\tau^*_{\mathrm{He}}/\tau_E$ | 5 |
| $a$ (m) | 2 | $T_e/T_i$ | 1.1 |
| $B_t$ (T) | 5.3 | $n_{e,sep}$ ($\mathrm{m}^{-3}$) | $0.3 \times 10^{20}$ |
| $I_p$ (MA) | 15 | $T_{e,sep}$ (eV) | 100 |
| $\kappa_{95}/\delta_{95}$ | 1.70/0.33 | $M_{eff}$ | 2.5 |
| $f_{\mathrm{Be}}$ (%) | 2 | $F_{P_\alpha}$ | 1 |
| $f_{\mathrm{Ar}}$ (%) | 0.12 | $r_{syn}$ | 0.7 |

TABLE II

Description of the LCMS in HELIOS for ITER Scenario 2

| | | | |
|---|---|---|---|
| $\kappa_X^{(1)}/\kappa_X^{(2)}$ | 1.687/2.001 | $\psi^{-(1)}/\psi^{+(1)}$ (deg) | 0/0 |
| $\delta_X^{(1)}/\delta_X^{(2)}$ | 0.466/0.568 | $\psi^{-(2)}/\psi^{+(2)}$ (deg) | 67.92/22.46 |

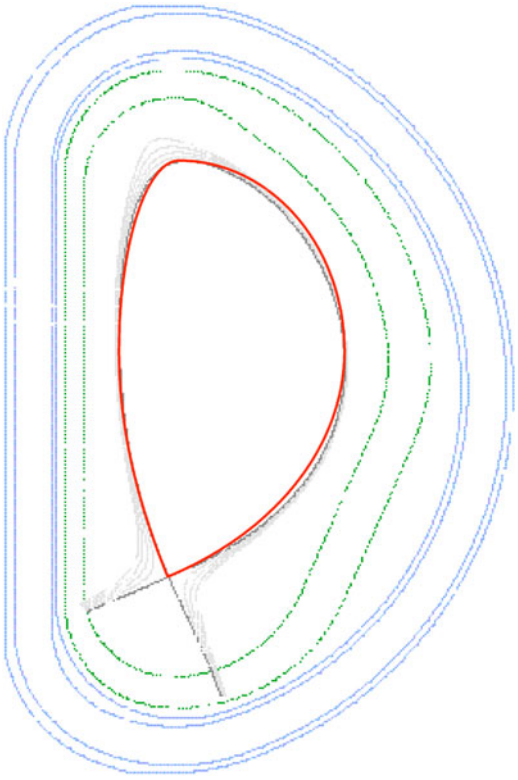

Fig. 8. ITER scenario 2 operating point MHD equilibrium and HELIOS LCMS (solid line, in red online) corresponding to measured $\kappa_X^{(i)}, \delta_X^{(i)}, \psi^{-(i)}, \psi^{+(i)}$.

TABLE III

ITER Geometrical Parameters Calculated by HELIOS Compared to ITER Documentation Parameters

| | HELIOS | ITER (Ref. 29) |
|---|---|---|
| $A$ | 3.1 | 3.1 |
| $V$ ($\mathrm{m}^3$) | 827 | 831 |
| $S_p$ ($\mathrm{m}^2$) | 21.8 | 21.9 |
| $S$ ($\mathrm{m}^2$) | 684 | 683 |
| $L$ (m) | 18.2 | 18.2 |
| $q_{95}$ | 3.00 | 3.0 |

For the profile parameters $\beta_T$ and $\alpha_T$ in Eq. (19), we take $\beta_T = 2$, and the value of $\alpha_T$ is adjusted in such a way that the scenario 2 operating point ($Q = 10$, $P_{fus} = 400$ MW) is obtained for $\bar{n}_e/n_G \simeq 0.85$. We get $\alpha_T = 2.18$.

The POpCon plot obtained for scenario 2 purely inductive H-mode operation of ITER with IPB98(y,2) scaling [$H_{98} = 1$ in Eq. (43)] is drawn in Fig. 9 (Ref. 1). It can be seen that that the maximum $Q$ in inductive H-mode

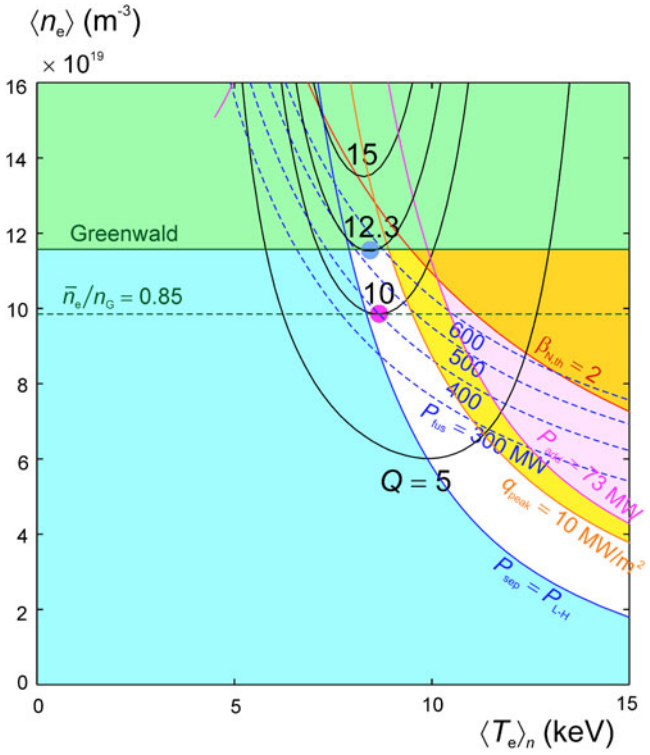


Fig. 9. POpCon plot for purely inductive H-mode operation in ITER (scenario 2) with IPB98($y$,2) scaling. Volume averaged electron density and density averaged electron temperature are chosen for the axes. Iso-$Q$ contours (as described in Sec. II.K) are plotted as solid lines; iso-$P_{fus}$ contours are the dashed lines (in blue online). The following forbidden regions are shaded with increasingly deep gray: $P_{sep} < P_{L\text{-}H}$ (in blue online), $q_{peak} > 10$ MW/m$^2$ (in light orange online), $P_{add} > P_{add\text{-}available}$ (in light magenta online), $\beta_{N,th} > 2$ (possible NTMs) (in dark orange online), $\bar{n}_e > n_G$ (in green online). Only the white region corresponds to acceptable equilibrium operating points.

operation with the parameters in Table I would be $Q = 12.3$ (neglecting possible confinement degradation near the Greenwald density limit).

The scenario 2 operating point ($Q = 10$, $P_{fus} = 400$ MW) is obtained for $P_{add} \simeq 38.6$ MW. It appears to be close to the L-H threshold, as it corresponds to $P_{sep}/P_{L\text{-}H} \simeq 1.13$ (i.e., only a 13% margin). A 30% margin of $P_{sep}$ with respect to $P_{L\text{-}H}$ (generally considered to be adequate to get $H_{98} \simeq 1$) is obtained by slightly increasing the additional power to 43 MW, giving an acceptable operating point for $\bar{n}_e/n_G = 0.85$ with $Q \simeq 9.87$, $P_{fus} \simeq 440$ MW, and $q_{peak} \simeq 5.50$ MW/m$^2$.

It is also interesting to note that, in the frame of the modeling, the operating points corresponding to the maximum available additional power in the first phase of ITER ($P_{add} = 73$ MW) are situated above the limit $q_{peak} = 10$ MW/m$^2$. This means that high fusion power steady-state operating points of ITER that this additional power could allow are beyond divertor capabilities for the 2% beryllium and 0.12% argon fractions considered in scenario 2. However, this power is useful for hybrid operation (scenario 3) where the argon fraction is increased to 0.19%.

The operating window for $\bar{n}_e/n_G = 0.85$ appears to be relatively narrow as illustrated in Fig. 10, where it can be seen that the additional power corresponding to H-L transition (neglecting any hysteresis effect) is 35 MW, and the one corresponding to maximum thermal load on the divertor plates is 51 MW.

The parameters corresponding to the operating point with $Q = 10$, $P_{fus} = 400$ MW are given in Table IV. They are compared to the ones corresponding to the operating point with $P_{fus}/P_{add} = 10$, $P_{fus} = 400$ MW considered in Ref. 29. It can be seen that the agreement is fair. The main differences are in the synchrotron losses calculation, in the assumption $P_{line\text{-}core} = P_{line\text{-}bulk}/3$ assumed in Ref. 29 (compared to $\rho_{core} = 0.95$ in HELIOS), and in the $P_{L\text{-}H}$ scaling used.

The density, temperature, and pressure profiles corresponding to the scenario 2 operating point are plotted in Fig. 11. Also represented is the line-radiated power per unit volume for beryllium and argon impurities in the

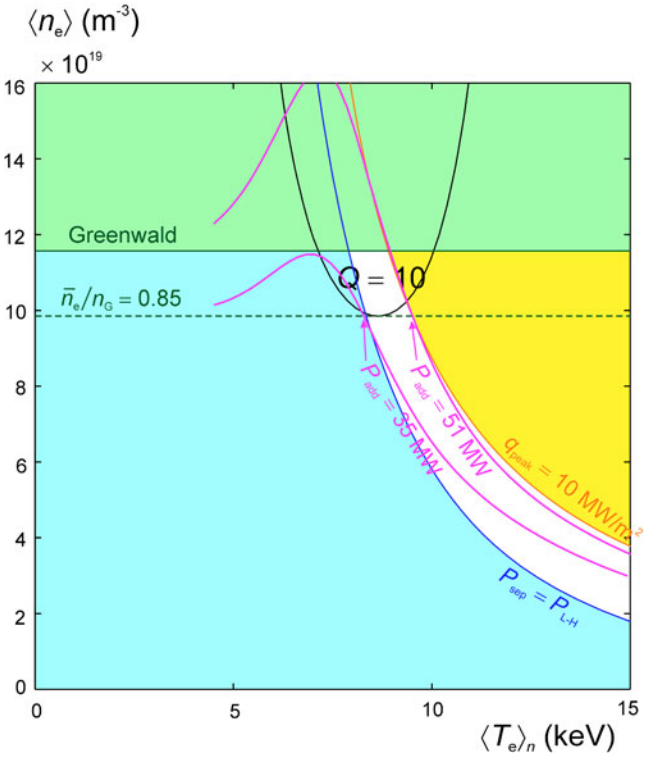


Fig. 10. Additional powers corresponding to the H-L transition and to maximum divertor heat load at 85% of the Greenwald density limit.

TABLE IV

Parameters for the Scenario 2 Inductive Operation in ITER Obtained with HELIOS Compared to the Parameters Described in Ref. 29

| | HELIOS | ITER (Ref. 29) |
|---|---|---|
| $H_{98}$ | **1** | **1** |
| $Q$ | **10** | **10** ($P_{fus}/P_{add}$) |
| $P_{fus}$ (MW) | **400** | **400** |
| $\bar{n}_e/n_G$ | 0.85 | 0.85 ($\langle n_e\rangle/n_G$) |
| $\langle n_e\rangle$ ($10^{20}$ m$^{-3}$) | 0.985 | 1.01 |
| $n_{e,ped}$ ($10^{20}$ m$^{-3}$) | 1.03 | — |
| $T_{e,ped}$ (keV) | 3.30 | — |
| $\langle T_e\rangle_n/\langle T_e\rangle$ (keV) | 8.65/8.23 | —/8.8 |
| $T_{e0}$ (keV) | 22.3 | — |
| $f_{\mathrm{He}}$ (%) | 3.29 | 3.2 ($f_{\mathrm{He},ave}$) |
| $Z_{eff}$ | 1.67 | 1.66 |
| $f_{BS}$ (%) (Hoang fit with $\alpha_j = 1$) | 17.3 | 16 (PRETOR modeling) |
| $P_\alpha$ (MW) | 81.0 | 80 |
| $P_{OH}$ (MW) | 1.42 | 1 |
| $U_\ell$ (mV) | 94.8 | 75 |
| $P_{add}$ (MW) | 38.6 | 40 |
| $P_{source}$ (MW) | 121 | 121 ($P_{tot}$) |
| $P_B$ (MW) | 20.8 | 21 |
| $P_{syn}$ (MW) | 4.06 | 8 |
| $P_{con} = P_{net}$ (MW) | 81.1 | 87 |
| $W_{th}$ (MJ) | 306 | 320 |
| $\tau_E$ (s) | 3.78 | 3.7 |
| $\beta_N/\beta_{N,th}$ | 1.66/1.56 | 1.8 ($\beta_N$) |
| $\beta_{p,th}$ | 0.578 | 0.65 ($\beta_p$) |
| $\Gamma_n$ (MW/m$^2$) | 0.467 | — |
| $P_{line\text{-}core}$ (MW) | 15.0 | 6 |
| $P_{line\text{-}mantle}$ (MW) | 1.95 | 12 |
| $P_{line\text{-}bulk}$ (MW) | 17.0 | 18 ($P_{line}$) |
| $P_{sep}/P_{L\text{-}H}$ ($MW$) | 79.1/70.0 | 75/48 |
| $P_{line\text{-}tot}$ (MW) | 50.2 | — |
| $P_{non\text{-}rad}$ (MW) | 45.9 | — |
| $q_{peak}$ (MW/m$^2$) | 3.23 | $<5$ |
| $\lvert dp/dr\rvert_{ped}/\lvert dp/dr\rvert_{balloon}$ ($10^5$ Pa/m) | 11.0/12.5 | — |

external part of the plasma. Be radiation is seen to be negligible. The peak of Ar radiation at $T_e = 200$ eV (Fig. 4) is visible at the plasma edge. The angular aspect of the curve is due to the ADAS scarce data (Fig. 4) used for the Ar radiative power loss function. Also note that Ar radiation is not negligible in the plasma core as indicated in Table IV. We see in Table IV that the choice $\rho_{ped} = 0.925$ results in a pressure gradient at the pedestal slightly lower than the ballooning limit given in Eq. (50).

#### *IV.A.2. ITER Inductive Operation with IPB98(y,2) Scaling and 10% Reduced Field*

For the ITER Design Review,[1] it appeared important to study the effect on ITER performances in inductive operation, of a 10% decrease of the magnetic field (with correlative decrease of the plasma current to keep the same edge safety factor). The POpCon plot in this case is drawn in Fig. 12.

It can be seen that the maximum $Q$ for operation at $\bar{n}_e/n_G = 0.85$ is close to 6, to be compared with 10 in the full $B_t$ case (see Fig. 9). The corresponding fusion power is only 300 MW.

#### *IV.A.3. ITER Inductive Operation with ITERH06-IP($y, dd$) Scaling*

It is interesting to consider inductive operation of ITER with the same parameters as in Sec. IV.A.1 just changing the energy confinement time scaling to the ITERH06-IP($y, dd$) scaling with $H_{06} = 1$ in Eq. (44). The POpCon plot is plotted in Fig. 13.

It can be seen that the iso-$Q$ lines have a different topology in this case.[b] The maximum $Q$ compatible with the operating window is $Q = 9.2$. It is no longer obtained at the Greenwald density limit (as in Fig. 9) but at low density, at the intersection of the $P_{sep} = P_{L\text{-}H}$ curve with the $Q = 9.2$ curve. The operating point at 85% of the Greenwald density limit giving $P_{fus} = 400$ MW corresponds to $Q \simeq 8.4$ [to be compared with $Q = 10$ in the case of IPB98($y$,2) scaling].

### IV.B. DEMO Noninductive Operation in Advanced Mode

#### *IV.B.1. PPCS-C Machine with $H_{98} = 1.5$*

A DEMO machine is considered, based on the PPCS-C design[3] with the parameters in Table V. For the description of the LCMS, we take the parameters listed in Table VI. These parameters have been obtained by imposing the following PPCS-C data:

$$\kappa_X = \frac{\kappa_X^{(1)} + \kappa_X^{(2)}}{2} = 2.1 \quad \text{and} \quad \delta_X = \frac{\delta_X^{(1)} + \delta_X^{(2)}}{2} = 0.7$$

while keeping the $\kappa_X^{(1)}/\kappa_X^{(2)}$ and $\delta_X^{(1)}/\delta_X^{(2)}$ ratios identical to the ones of the above ITER shape. With these data, the global parameters listed in Table VII are obtained.

[b] In the case of a scaling with monomial $\bar{n}_e$ and $P_{net}$ dependences (with $x_n$ and $x_P$ exponents, respectively) and neglecting synchrotron radiation losses, it may be shown that iso-$Q$ lines in the $(\langle T_e\rangle_n, \langle n_e\rangle)$ space are convex if $1 + x_n - 2x_P > 0$, and concave in the opposite case. For IPB98($y$,2) scaling, $1 + x_n - 2x_P = 0.03$ so that iso-$Q$ lines are convex as observed in Fig. 9. For ITERH06-IP($y, dd$) scaling, neglecting the $(\bar{n}_e/n_G)^{-0.22\ln(\bar{n}_e/n_G)}$ term, $1 + x_n - 2x_P \simeq -0.447764$, so that iso-$Q$ lines are concave as observed in Fig. 13.

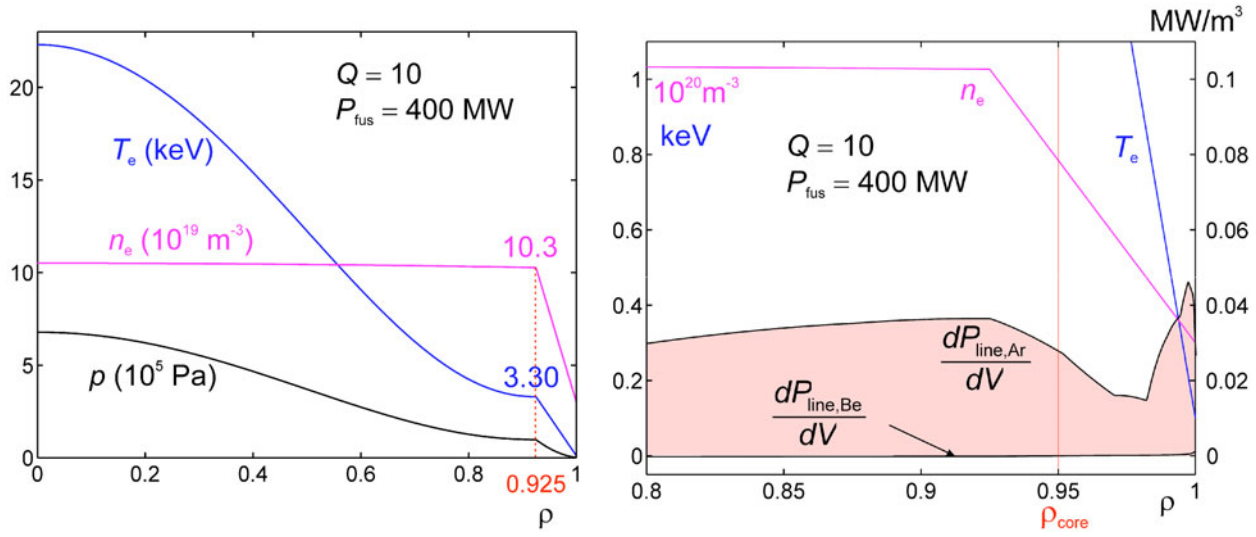


Fig. 11. Density, temperature, pressure, and line-radiation profiles for the scenario 2 inductive operating point of ITER.

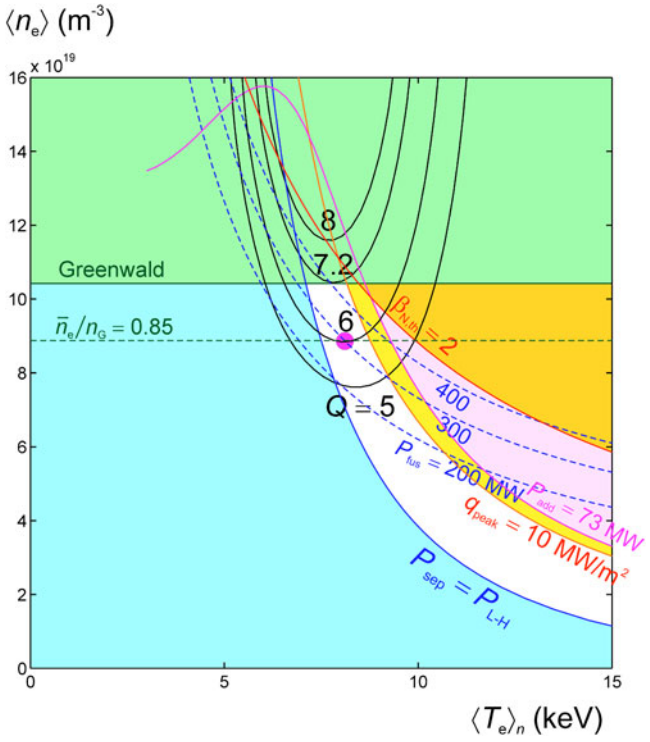


Fig. 12. POpCon plot for purely inductive H-mode operation in ITER with IPB98($y$,2) scaling with a 10% reduction of magnetic field and plasma current ($B_t = 4.77$ T, $I_p = 13.5$ MA).

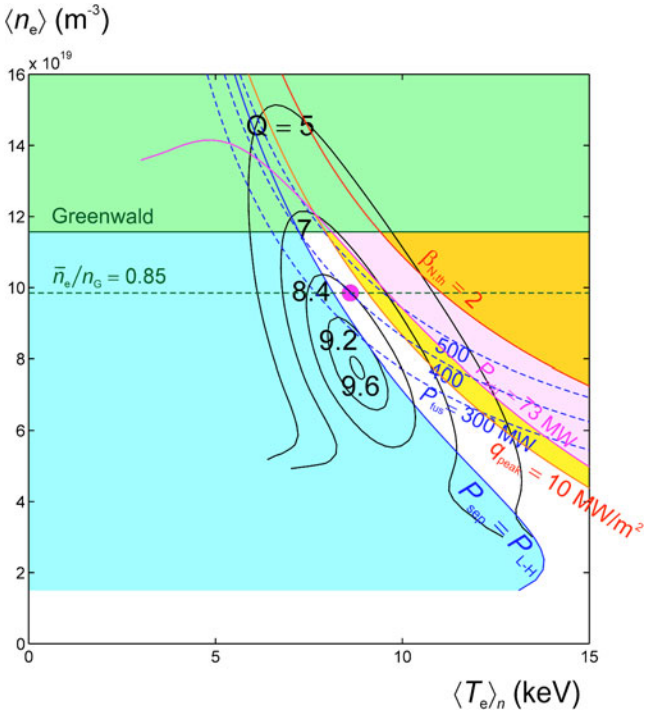


Fig. 13. POpCon plot for purely inductive H-mode operation in ITER with ITERH06-IP($y, dd$) scaling ($B_t = 5.3$ T, $I_p = 15$ MA).

For the pedestal width and the core plasma definition, we take

$$\rho_{ped} = 0.8 \quad \text{and} \quad \rho_{core} = 0.95 \ .$$

A flat density profile with $\alpha_n = 1$ and $n_{e0}/n_{e,ped}$ given in Eq. (57) is considered. The temperature profile is supposed to exhibit an outer internal barrier with a strong gradient near $\rho = 0.6$. Such a profile is well described using high values for $\beta_T$ and $\alpha_T$. $\beta_T = 6$, $\alpha_T = 8.06$ are

TABLE V

Basic Parameters for the PPCS-C Machine

| | | | |
|---|---|---|---|
| $R$ (m) | 7.5 | $T_e/T_i$ | 1 |
| $a$ (m) | 2.5 | $n_{e,sep}$ (m$^{-3}$) | $0.3 \times 10^{20}$ |
| $B_t$ (T) | 6 | $T_{e,sep}$ (eV) | 100 |
| $I_p$ (MA) | 20.1 | $M_{eff}$ | 2.5 |
| $\kappa_{95}/\delta_{95}$ | 1.90/0.47 | $F_{P_\alpha}$ | 1 |
| $f_{\mathrm{Be}}$ (%) | 0 | $r_{syn}$ | 0.7 |
| $\tau^*_{\mathrm{He}}/\tau_E$ | 5 | | |

TABLE VI

Description of the LCMS in HELIOS for the PPCS-C Machine

| | | | |
|---|---|---|---|
| $\kappa_X^{(1)}/\kappa_X^{(2)}$ | 1.921/2.279 | $\psi^{-(1)}/\psi^{+(1)}$ (deg) | 0/0 |
| $\delta_X^{(1)}/\delta_X^{(2)}$ | 0.6309/0.7691 | $\psi^{-(2)}/\psi^{+(2)}$ (deg) | 67.92/22.46 |

TABLE VII

PPCS-C Geometrical Parameters Calculated by HELIOS

| | | | |
|---|---|---|---|
| $A$ | 3 | $S$ (m$^2$) | 1130 |
| $V$ (m$^3$) | 1770 | $L$ (m) | 25.4 |
| $S_p$ (m$^2$) | 39.2 | $q_{95}$ | 4.32 |

chosen. The negative NBI current drive efficiency is supposed to be given by Eq. (53).

For the calculation of the $P_{e,n}$ iso-curves, the power plant efficiencies given in Eq. (56) are taken. The POpCon plot obtained with advanced operation with $H_{98} = 1.5$ and an argon fraction $f_{\mathrm{Ar}} = 0.3\%$ is drawn in Fig. 14.

It can be seen that, for low argon fractions, intersection of the $f_{NI} = 100\%$ contour with the $q_{peak} = 10$ MW/m$^2$ limit occurs for operating points with low density, low fusion power, and low $Q$ (resulting in very low network electrical power output). For $f_{\mathrm{Ar}} = 0.3\%$, the above operating point has $\langle n_e \rangle \simeq 5.91 \times 10^{19}$ m$^{-3}$, $Q \simeq 11.1$, $P_{fus} \simeq 994$ MW, $P_{e,n} \simeq 272$ MW. For the same argon fraction, the noninductive operating point at the Greenwald density limit, which would feature $Q \simeq 17.0$ and $P_{e,n} \simeq 651$ MW, corresponds to a 27.6 MW/m$^2$ peak load on the divertor plates.

Increasing $f_{\mathrm{Ar}}$ allows access to larger densities, $Q$ and $P_{e,n}$ as illustrated in Fig. 15. For $f_{\mathrm{Ar}} \simeq 0.407\%$, a fully noninductive operating point at the Greenwald density limit satisfying the divertor constraint may be obtained,

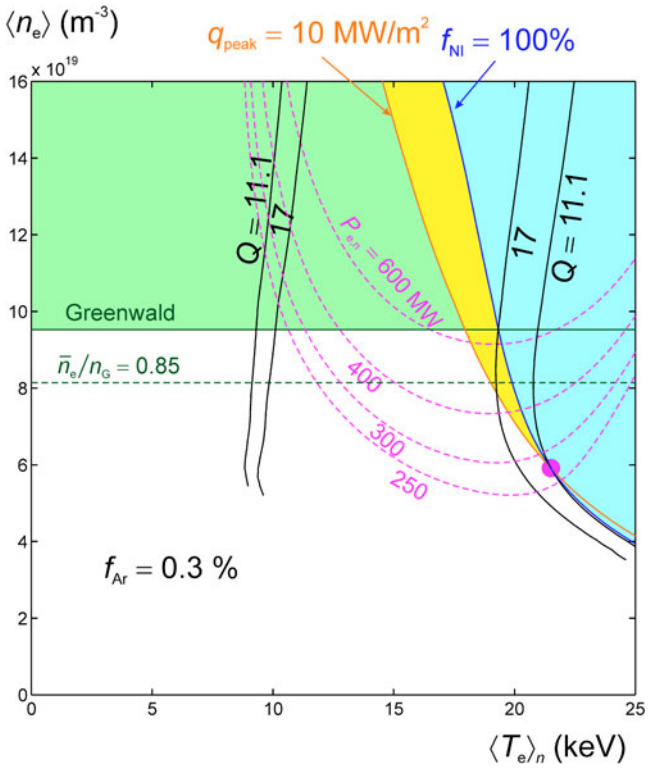


Fig. 14. POpCon plot for advanced operation ($H_{98} = 1.5$) of DEMO PPCS-C with $f_{\mathrm{Ar}} = 0.3\%$.

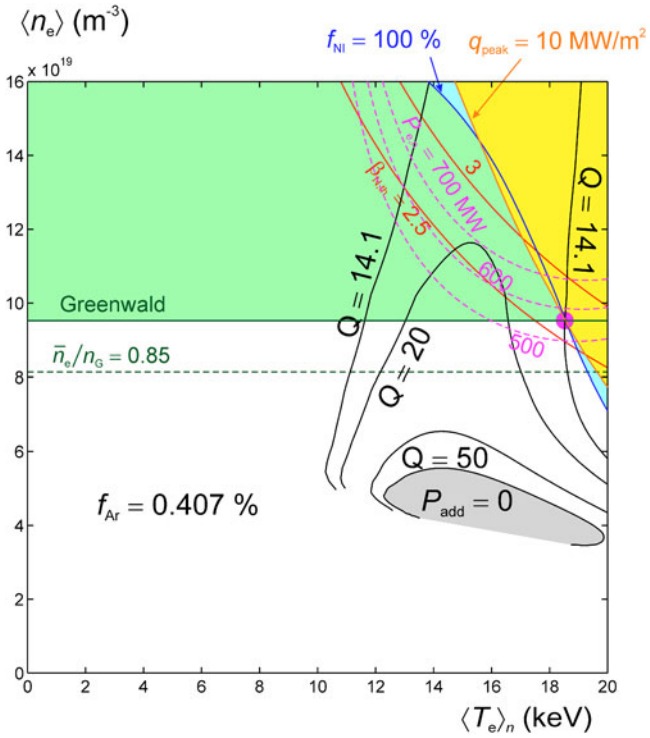


Fig. 15. POpCon plot for advanced operation ($H_{98} = 1.5$) of DEMO PPCS-C with $f_{\mathrm{Ar}} = 0.407\%$.

TABLE VIII

Parameters of the Fully Noninductive DEMO PPCS-C Operating Point at the Greenwald Density Limit and Maximum Divertor Heat Load

| | | | |
|---|---|---|---|
| $H_{98}$ | **1.5** | $P_{syn}$ (MW) | 128 |
| Q | **14.1** | $P_{con} = P_{net}$ (MW) | 212 |
| $\bar{n}_e/n_G$ | **1** | $\tau_E$ (s) | 6.42 |
| $f_{Ar}$ (%) | **0.407** | $\beta_N/\beta_{N,th}$ | 3.00/2.66 |
| $\langle n_e \rangle$ ($10^{20}$ m$^{-3}$) | 0.952 | $\Gamma_n$ (MW/m$^2$) | 1.32 |
| $n_{e,ped}$ ($10^{20}$ m$^{-3}$) | 1.09 | $P_{line\text{-}core}$ (MW) | 80.2 |
| $T_{e,ped}$ (keV) | 6.09 | $P_{line\text{-}mantle}$ (MW) | 11.2 |
| $\langle T_e \rangle_n/\langle T_e \rangle$ (keV) | 18.5/16.2 | $P_{sep}/P_{L\text{-}H}$ (MW) | 200/125 |
| $T_{e0}$ (keV) | 45.9 | $P_{line\text{-}tot}$ (MW) | 182 |
| $f_{He}$ (%) | 12.7 | $P_{non\text{-}rad}$ (MW) | 109 |
| $Z_{eff}$ | 2.50 | $q_{peak}$ (MW/m$^2$) | 9.86 |
| $f_{BS}$ (%) (Hoang fit with $\alpha_j = 0.5$) | 46.9 | $\lvert dp/dr \rvert_{ped}/\lvert dp/dr \rvert_{balloon}$ ($10^5$ Pa/m) | 6.55/6.36 |
| $P_\alpha$ (MW) | 380 | $P_{e,g}$ (MW) | 1030 |
| $P_{fus}$ (MW) | 1880 | $P_{e,n}$ (MW) | 561 |
| $P_{OH}$ (MW) | $4.68 \times 10^{-3}$ | $f_{circ}$ (%) | 45.4 |
| $P_{add}$ (MW) | 133 | $P_{pump}$ (MW) | 220 |
| $\gamma_{CD}$ ($10^{20}$ A/W m$^2$) | 0.568 | $\eta_{PP}$ (%) | 26.1 |
| $P_B$ (MW) | 93.1 | | |

featuring $Q \simeq 14.1$ and $P_{e,n} \simeq 561$ MW. The other parameters for this operating point are listed in Table VIII. Notable is the strong helium fraction (12.7%) due to the $\tau^*_{He}/\tau_E = 5$ condition with high $\tau_E$, the large $\beta_N$ value (3.00), the large bootstrap fraction (~47%), and the strong synchrotron radiation loss (~130 MW).

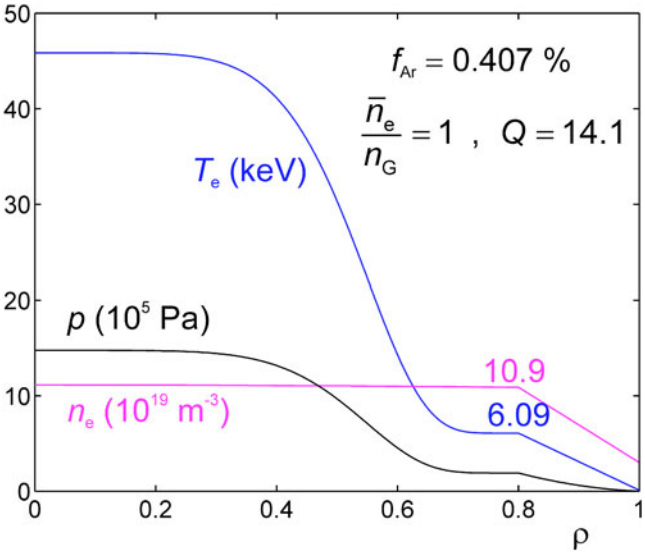


Fig. 16. Density, temperature, and pressure profiles for the DEMO PPCS-C fully noninductive operating point at the Greenwald density limit and maximum divertor heat load.

The operating point corresponds to a relatively low amplification factor $Q \simeq 14.1$ due to the strong dilution ($Z_{eff} \simeq 2.50$) generated by the necessary argon seeding and He contamination. Taking that into account plus the large required pumping power ($P_{pump} \simeq 220$ MW), we end with a strong circulated fraction ($f_{circ} \simeq 45.4\%$), a consequently relatively low electrical power delivered to the network ($P_{e,n} \simeq 561$ MW), and a very low power plant efficiency ($\eta_{PP} \simeq 26.1\%$). It is however important to note that high-temperature He cooling allows the large thermodynamic efficiency ($\eta_{th} = 44\%$) considered here. The possible reduction of $\eta_{th}$ must then be properly taken into account in the case of an alternative cooling method.

The temperature profile, showing a strong gradient near $\rho = 0.6$ characteristic of advanced operation, is plotted in Fig. 16. The large pedestal width ($\rho_{ped} \simeq 0.8$) is a direct consequence of our modeling: lower $\lvert dp/dr \rvert_{balloon}$ [larger $R$ and $q_{95}$ in Eq. (50)] and larger $T_{e,ped}$ than in the ITER case.

### *IV.B.2. DEMO-2007 Machine with $H_{98} = 1.3$*

The effect of reducing the $H_{98}$ factor from 1.5 to 1.3 as taken in the DEMO-2007 machine of Ref. 27 is now considered. The parameters are the same as given in Table V except for slightly lower magnetic field ($B_t = 5.86$ T) and plasma current ($I_p = 19.4$ MA), giving comparable $q_{95} \simeq 4.37$. All the other parameters are kept identical. One can see in Fig. 17 that the argon fraction must now be increased up to 0.584% to allow fully noninductive operation at $q_{peak} = 10$ MW/m$^2$ and $\bar{n}_e = n_G$. The corresponding amplification factor $Q$ drops

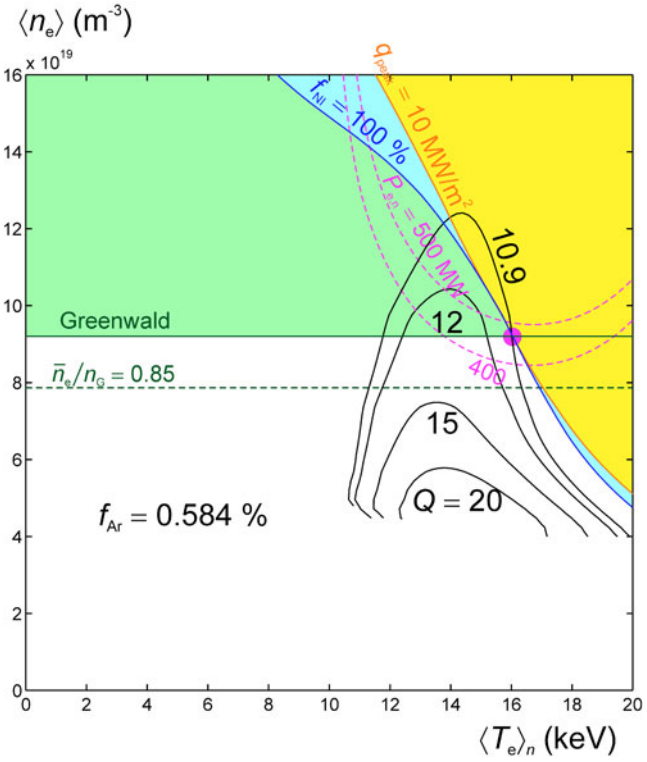


Fig. 17. POpCon plot for advanced operation ($H_{98} = 1.3$) of DEMO-2007 with $f_{\mathrm{Ar}} = 0.584\%$.

to 10.9 giving operation with $P_{e,n} \simeq 465$ MW and $\eta_{PP} \simeq 23.7\%$.

### IV.C. Example of Inductive Reactor Design

An example of application of HELIOS to the design of a 1000-MW(electric) purely inductive reactor operating in pure H-mode with IPB98($y$,2) scaling ($H_{98} = 1$) is considered now. The machine is supposed to be ITER-like for its shape and profiles. The same parameters as described in Sec. IV.A.1 are taken, except for the Be fraction, which is supposed to be zero.

The magnetic field at the plasma axis is calculated from Eq. (54) with

$$B_{t,\max} = 13.6\ \mathrm{T}\ , \quad A = 3.1\ ,$$

$$\Delta_{\mathrm{int}} = 1.9\ \mathrm{m}\ , \quad k_{B_{t,\max}} = 1\ .$$

The plasma current is calculated from the value of $q_{95}$ by means of Eq. (17). In the present application, we take

$$q_{95} = 3\ .$$

The fractions and efficiencies for the power plant balance are taken from Eq. (56). The radial build is self-consistency taken into account for the calculation of the magnetic fluxes described in Sec. II.L.4, where we take

$$B_{CS,\max} = 13\ \mathrm{T}\ , \quad j_{CS} = 16\ \mathrm{A/mm^2}\ ,$$

$$d_{TFC} = 1.1\ \mathrm{m}\ , \quad gap = 0.1\ \mathrm{m}\ ,$$

$$C_E = 0.45\ , \quad \ell_i = 0.85\ ,$$

$$\Phi_{PI} = 20\ \mathrm{Wb}\ .$$

With the above modeling and assumptions, it can be shown that the lowest value of $R$ required to get a 1000-MW(electric) machine satisfying the constraints on density and divertor load, is ~10 m. Taking $R = 10$ m, we get the following machine parameters:

$$a \simeq 3.23\ \mathrm{m}\ , \quad B_t \simeq 6.63\ \mathrm{T}\ ,$$

$$d_{CS} \simeq 0.647\ \mathrm{m}\ , \quad I_p \simeq 30.2\ \mathrm{MA}\ .$$

The POpCon plot for operation of this machine with $f_{\mathrm{Ar}} = 0.177\%$ is drawn in Fig. 18. For lower values of the argon fraction, the operating point with $P_{e,n} = 1000$ MW, $q_{peak} = 10$ MW/m$^2$ is situated in the pink

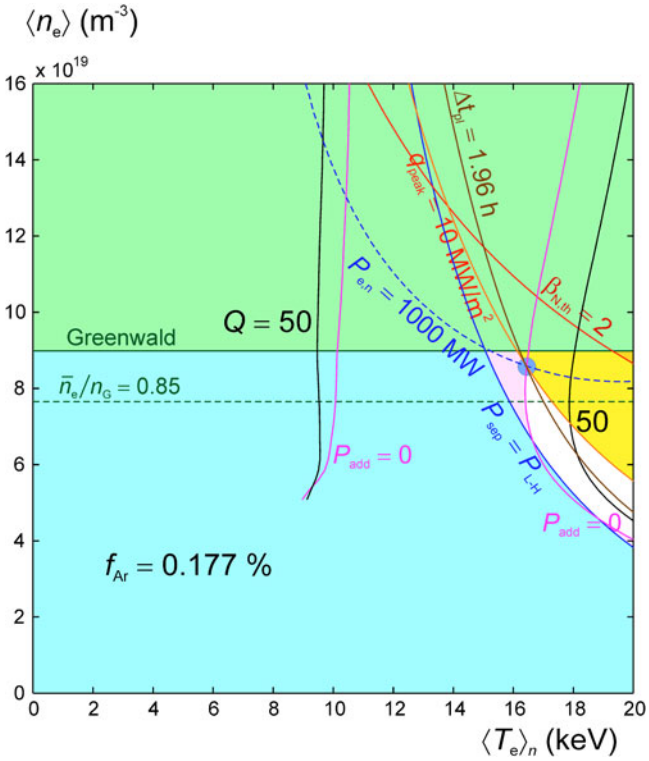


Fig. 18. POpCon plot for inductive operation ($H_{98} = 1$) in an ITER-like, $R = 10$ m reactor with $f_{\mathrm{Ar}} = 0.177\%$.

TABLE IX

Parameters of the $R = 10$ m ITER-Like Purely Inductive Reactor with $f_{\mathrm{Ar}} = 0.177\%$, $P_{add} = 0$, $q_{peak} = 10$ MW/m$^2$

| | | | |
|---|---|---|---|
| $H_{98}$ | **1** | $\beta_N/\beta_{N,th}$ | 1.80/1.62 |
| $Q$ | 1740 | $\Gamma_n$ (MW/m$^2$) | 1.14 |
| $\bar{n}_e/n_G$ | 0.954 | $P_{line\text{-}core}$ (MW) | 44.4 |
| $\langle n_e \rangle$ ($10^{20}$ m$^{-3}$) | 0.858 | $P_{line\text{-}mantle}$ (MW) | 7.54 |
| $n_{e,ped}$ ($10^{20}$ m$^{-3}$) | 0.892 | $P_{sep}/P_{L\text{-}H}$ (MW) | 240/186 |
| $T_{e,ped}$ (keV) | 5.58 | $P_{line\text{-}tot}$ (MW) | 112 |
| $\langle T_e \rangle_n/\langle T_e \rangle$ (keV) | 16.4/15.7 | $P_{non\text{-}rad}$ (MW) | 180 |
| $T_{e0}$ (keV) | 44.2 | $q_{peak}$ (MW/m$^2$) | **10** |
| $f_{\mathrm{He}}$ (%) | 12.7 | $P_{e,g}$ (MW) | 1310 |
| $Z_{eff}$ | 1.80 | $P_{e,n}$ (MW) | 998 |
| $f_{BS}$ (%) (Hoang fit with $\alpha_j = 1$) | 18.3 | $f_{circ}$ (%) | 24.0 |
| $P_\alpha$ (MW) | 515 | $P_{pump}$ (MW) | 281 |
| $P_{fus}$ (MW) | 2250 | $\eta_{PP}$ (%) | 34.3 |
| $P_{OH}$ (MW) | 1.46 | $\Phi_{CS}$ (Wb) | 920 |
| $P_{add}$ (MW) | **0** | $\Phi_{VF}$ (Wb) | 203 |
| $P_B$ (MW) | 97.1 | $\Phi_{res}$ (Wb) | 171 |
| $P_{syn}$ (MW) | 128 | $\Phi_{ind}$ (Wb) | 590 |
| $P_{con} = P_{net}$ (MW) | 248 | $\Phi_{pl}$ (Wb) | 342 |
| $\tau_E$ (s) | 8.40 | $\Delta t_{pl}$ (h) | 1.96 |

zone (color online) between the two branches of the ohmic-ignition curve ($P_{add} = 0$), corresponding to forbidden negative values for $P_{add}$. For $f_{\mathrm{Ar}} = 0.177\%$, the ignited operating point with $q_{peak} = 10$ MW/m$^2$ corresponds to $P_{e,n} \simeq 1000$ MW. At this point, the plateau duration given by the modeling is $\Delta t_{pl} \simeq 1.96$ h. For larger values of $f_{\mathrm{Ar}}$, the acceptable operating points give shorter plateau durations. The point with $f_{\mathrm{Ar}} = 0.177\%$, $P_{add} = 0$ is then the operating point with $P_{e,n} = 1000$ MW in this machine giving the longest plateau duration. The other parameters for this operating point are given in Table IX.

Note that, despite the enormous electrical power used for He pumping (281 MW), the power plant efficiency is marginally acceptable (~34%). This is because the plasma is at ohmic ignition so that no additional power needs to be injected.

The plateau duration (~2 h) obtained for this plasma aspect ratio ($A = 3.1$) and safety factor ($q_{95} = 3$) is shorter than the recommended 8-h value.[30] Longer plateau durations can be obtained by increasing $R$, $A$, or $q_{95}$. A detailed sensitivity analysis of this problem will be given in a separate paper, including detailed comparison with results obtained recently in Refs. 30 and 31.

## V. THE HELIOS CODE

The code is written in Fortran 77 (approximately 15 000 lines). It is a collection of subroutines with a main program forking to the different tasks. The program is not dependent on a commercial library as sources from the CERN (Ref. 32) and BBLCISI[c] libraries have been imported (for integration, equation solving, complete and incomplete elliptical functions, and gamma function).

Input is still basic. Specific data for the different machines studied are given in DATA in the main program, allowing easy archiving by just commenting. Parameters describing the physics (scalings used) and forking indices are read from a data file.

Iso-value curves in the $(\langle n_e \rangle, \langle T_e \rangle_n)$ plane for certain values of the $X$ parameter are described by $F(\langle n_e \rangle, \langle T_e \rangle_n, X) = 0$. The matrix of the $F$ function is calculated by HELIOS. A MATLAB post processing using the excellent "contour" tool generates the plot, which is printed as an eps file. This vector file is opened with CorelDraw to generate the final graph (colors, shading, comments).

For many years, the code has run on Alpha processors. It was ported recently to x86-64 Intel architecture. Best performances are obtained using the Intel compiler. The typical run time to generate a $50 \times 50$ matrix of the above $F$ function is 1 min. Calculations including modification of the geometry $(R, A, \kappa)$ are also very quick thanks to the closed form expressions derived for all the geometrical parameters. A large reduction in the computing time was also obtained by expressing the $\int_{S_p} (1/\eta(\rho))(R_0/R)\, dS_p$ double integral as a simple one.

[c] BBLCISI is a private CEA Fortran scientific library (no longer supported).

Because of the present experimental and rapidly developing state of the code, it is not envisaged to distribute binaries. However, parts of the code will soon be integrated in a more general systems code tool, which will be made available to the community.

## VI. CONCLUSIONS

The 0-D HELIOS code has been described in detail in the case of D-T plasmas. The following features may be specifically outlined:

1. description of the poloidal section of the LCMS by means of four portions of conics, allowing closed form calculation of the plasma volume, surface, poloidal surface, and LCMS length
2. exact poloidal surface and volume integration valid for arbitrary aspect ratio in the approximation of magnetic surfaces similar to the LCMS
3. parabolic type density profile with a pedestal and finite value at the separatrix. Two-parameters temperature profile with a pedestal and finite value at the separatrix, allowing simulation of temperature profiles for a wide variety of tokamak operations.
4. scaling for the pedestal temperature
5. self-consistent calculation of the He contents from the $\tau^*_{\mathrm{He}}/\tau_E$ = const. condition
6. accurate calculation of the loop voltage and ohmic heating taking into account the $1/R$ variation of the equilibrium electric field
7. calculation of the plasma core and plasma mantle line radiation of light impurities (Be and Ar) from the tabulated radiative power loss functions
8. modeling for the thermal load on the divertor plates
9. modeling for the calculation of the magnetic flux stored in the central solenoid and vertical field as well as for the flux consumption during current ramp-up. This modeling allows the calculation of the plateau duration of an inductive discharge.
10. detailed calculation of the power plant balance taking into account recirculation of the gross electrical power to energize the pumping system
11. output in the form of easily readable POpCon plots.

Recent application of the HELIOS code in an ITER sensitivity analysis has highlighted the proximity of the scenario 2 inductive operating point to the H-L transition and the great sensitivity of $Q$ to the magnetic field intensity (a 40% degradation of $Q$ is observed for a 10% reduction of $B_t$).

The sensitivity of ITER extrapolations to the choice of the scaling for the energy confinement time is also illustrated here. Using ITERH06-IP$(y, dd)$ results in a $Q$ of 8.4 for operation at $\bar{n}_e/n_G = 0.85$ with $P_{fus} = 400$ MW [to be compared with $Q = 10$ in the same conditions with IPB98$(y,2)$ scaling].

Application to a DEMO based on PPCS-C (in advanced operation with $H_{98} = 1.5$) shows that strong argon seeding must be used to obtain fully noninductive operating points satisfying the divertor thermal load constraint at the Greenwald density limit. The modest $Q$ (14.1) obtained in these conditions associated with a 21% fraction of the gross electrical power used to energize the pumping system results in a low network electrical power output and very low power plant efficiency (despite the high thermodynamic efficiency $\eta_{th} = 44\%$ allowed by He cooling).

In the case of DEMO-2007 with the same size with slightly lower magnetic field and plasma current but reduced confinement time enhancement ($H_{98} = 1.3$), the effects described above are still more pronounced.

An example of application to the design of a 1000-MW(electric) ITER-like (with $A = 3.1$, $q_{95} = 3$) purely inductive reactor in H-mode shows that the minimum major radius required is $R \sim 10$ m. For a $R = 10$ m machine, a minimum $f_{\mathrm{Ar}} \sim 0.18\%$ is required to get 1000-MW(electric) at the maximum divertor load. The operating point with maximum discharge duration ($\Delta t_{pl} \sim 2$ h) is obtained at ohmic ignition, resulting in a marginally acceptable power plant efficiency ($\sim$34%). In this example, there is no attempt to optimize $R$, $A$, and $q_{95}$ in order to maximize the discharge duration.

## APPENDIX A

## EXPRESSIONS OF THE CORRECTION FUNCTIONS FOR THE VOLUME, SURFACES, AND LENGTH IN THE UP-DOWN SYMMETRICAL CASE

Introducing the following functions:

$$\mathrm{arc}(t) = 1 - \frac{2}{\pi}\arcsin\frac{t}{1-t} - \frac{2}{\pi}\frac{t\sqrt{1-2t}}{(1-t)^2} \quad ,$$

$$\mathrm{arch}(t) = \frac{t\sqrt{2t-1}}{(1-t)^2} - \mathrm{arcsinh}\frac{\sqrt{2t-1}}{1-t} \quad ,$$

and

$$\kappa^- = \frac{\kappa_X}{1-\delta_X} \quad \text{and} \quad \kappa^+ = \frac{\kappa_X}{1+\delta_X} \quad ,$$

we get the following expressions for the inner and outer parts of the correction functions (supposing $\kappa^- \geq 1$, $\kappa^+ \geq 1$):

**Volume**

$$\Theta_V^{*-} = \begin{cases} \dfrac{1-\delta_X}{2}\left[\left(1-\dfrac{1}{A}\,\dfrac{\delta_X-(1+\delta_X)t^-}{1-2t^-}\right)\dfrac{(1-t^-)^2}{(1-2t^-)^{3/2}}\,\mathrm{arc}(t^-)-\dfrac{4}{3\pi}\,\dfrac{1}{A}\,\dfrac{1-\delta_X}{1-2t^-}\right] & \text{if } 0\le t^-<\tfrac{1}{2} \\ \dfrac{4(1-\delta_X)}{3\pi}\left(1-\dfrac{1}{A}\,\dfrac{2+3\delta_X}{5}\right) & \text{if } t^-=\tfrac{1}{2} \\ \dfrac{1-\delta_X}{\pi}\left[\left(1-\dfrac{1}{A}\,\dfrac{(1+\delta_X)t^--\delta_X}{2t^--1}\right)\dfrac{(1-t^-)^2}{(2t^--1)^{3/2}}\,\mathrm{arch}(t^-)+\dfrac{2}{3}\,\dfrac{1}{A}\,\dfrac{1-\delta_X}{2t^--1}\right] & \text{if } \tfrac{1}{2}<t^-<1 \\ \dfrac{1-\delta_X}{\pi}\left(1-\dfrac{1}{A}\,\dfrac{1+2\delta_X}{3}\right) & \text{if } t^-=1 \end{cases}$$

$$\Theta_V^{*+} = \begin{cases} \dfrac{1+\delta_X}{2}\left[\left(1-\dfrac{1}{A}\,\dfrac{\delta_X+(1-\delta_X)t^+}{1-2t^+}\right)\dfrac{(1-t^+)^2}{(1-2t^+)^{3/2}}\,\mathrm{arc}(t^+)+\dfrac{4}{3\pi}\,\dfrac{1}{A}\,\dfrac{1+\delta_X}{1-2t^+}\right] & \text{if } 0\le t^+<\tfrac{1}{2} \\ \dfrac{4(1+\delta_X)}{3\pi}\left(1+\dfrac{1}{A}\,\dfrac{2-3\delta_X}{5}\right) & \text{if } t^+=\tfrac{1}{2} \\ \dfrac{1+\delta_X}{\pi}\left[\left(1+\dfrac{1}{A}\,\dfrac{\delta_X+(1-\delta_X)t^+}{2t^+-1}\right)\dfrac{(1-t^+)^2}{(2t^+-1)^{3/2}}\,\mathrm{arch}(t^+)-\dfrac{2}{3}\,\dfrac{1}{A}\,\dfrac{1+\delta_X}{2t^+-1}\right] & \text{if } \tfrac{1}{2}<t^+<1 \\ \dfrac{1+\delta_X}{\pi}\left(1+\dfrac{1}{A}\,\dfrac{1-2\delta_X}{3}\right) & \text{if } t^+=1 \end{cases}$$

**Poloidal section surface**

$$\Theta_{Sp}^{*-} = \begin{cases} \dfrac{1-\delta_X}{2}\,\dfrac{(1-t^-)^2}{(1-2t^-)^{3/2}}\,\mathrm{arc}(t^-) & \text{if } 0\le t^-<\tfrac{1}{2} \\ \dfrac{4(1-\delta_X)}{3\pi} & \text{if } t^-=\tfrac{1}{2} \\ \dfrac{1-\delta_X}{\pi}\,\dfrac{(1-t^-)^2}{(2t^--1)^{3/2}}\,\mathrm{arch}(t^-) & \text{if } \tfrac{1}{2}<t^-<1 \\ \dfrac{1-\delta_X}{\pi} & \text{if } t^-=1 \end{cases}$$

$$\Theta_{Sp}^{*+} = \begin{cases} \dfrac{1+\delta_X}{2}\,\dfrac{(1-t^+)^2}{(1-2t^+)^{3/2}}\,\mathrm{arc}(t^+) & \text{if } 0\le t^+<\tfrac{1}{2} \\ \dfrac{4(1+\delta_X)}{3\pi} & \text{if } t^+=\tfrac{1}{2} \\ \dfrac{1+\delta_X}{\pi}\,\dfrac{(1-t^+)^2}{(2t^+-1)^{3/2}}\,\mathrm{arch}(t^+) & \text{if } \tfrac{1}{2}<t^+<1 \\ \dfrac{1+\delta_X}{\pi} & \text{if } t^+=1 \end{cases}$$

Special cases: In the case with no $X$ points ($\psi^- = \psi^+ = 0$), we get

$$\Theta_{Sp}^{*} = 1 \quad \text{independent of } \delta_X \ .$$

**Toroidal surface**

$$
\Theta_S^{*-} = \begin{cases}
\dfrac{\kappa_X}{\pi \boldsymbol{E}_1(\kappa_X)} \dfrac{1-t^-}{\sqrt{1-2t^-}} \left[ \left( 1 - \dfrac{1}{A} \dfrac{\delta_X - (1+\delta_X)t^-}{1-2t^-} \right) E\left( \theta_X^-, \sqrt{1 - \dfrac{1}{(1-2t^-)\kappa^{-2}}} \right) - \cdots \right. \\
\qquad \left. - \dfrac{1}{A} \dfrac{1-\delta_X}{2} \dfrac{1}{\sqrt{1-2t^-}} \left( \dfrac{\sqrt{t^{-2}+1/\kappa^{-2}}}{1-t^-} + \dfrac{1-t^-}{\sqrt{1-2t^--1/\kappa^{-2}}} \arcsin \dfrac{\sqrt{1-2t^--1/\kappa^{-2}}}{1-t^-} \right) \right] \\
\qquad\qquad \text{if } 0 \le t^- < \dfrac{1}{2} - \dfrac{1}{2\kappa^{-2}} \\
\dfrac{1}{2\pi \boldsymbol{E}_1(\kappa_X)} \dfrac{\kappa_X^2 + (1-\delta_X)^2}{1-\delta_X} \left[ \left( 1 + \dfrac{1}{2A} \dfrac{\kappa_X^2 + \delta_X^2 - 1}{1-\delta_X} \right) \arcsin \dfrac{2\kappa_X(1-\delta_X)}{\kappa_X^2 + (1-\delta_X)^2} - \dfrac{\kappa_X}{A} \right] \quad \text{if } t^- = \dfrac{1}{2} - \dfrac{1}{2\kappa^{-2}} \\
\dfrac{1-\delta_X}{\pi \boldsymbol{E}_1(\kappa_X)} \dfrac{1-t^-}{1-2t^-} \left\{ \left( 1 - \dfrac{1}{A} \dfrac{\delta_X - (1+\delta_X)t^-}{1-2t^-} \right) \left[ \boldsymbol{E}\left( \sqrt{1-(1-2t^-)\kappa^{-2}} \right) - E\left( \dfrac{\pi}{2} - \theta_X^-, \sqrt{1-(1-2t^-)\kappa^{-2}} \right) \right] - \cdots \right. \\
\qquad \left. - \dfrac{\kappa_X}{2A} \left( \dfrac{\sqrt{t^{-2}+1/\kappa^{-2}}}{1-t^-} + \dfrac{1-t^-}{\sqrt{2t^--1+1/\kappa^{-2}}} \ln \dfrac{\sqrt{t^{-2}+1/\kappa^{-2}} + \sqrt{2t^--1+1/\kappa^{-2}}}{1-t^-} \right) \right\} \\
\qquad\qquad \text{if } \dfrac{1}{2} - \dfrac{1}{2\kappa^{-2}} < t^- < \dfrac{1}{2} \\
\dfrac{1}{2\pi \boldsymbol{E}_1(\kappa_X)} \left[ \sqrt{\kappa_X^2 + 4(1-\delta_X)^2} \left( 1 - \dfrac{1}{A} \dfrac{8(1-\delta_X^2) - \kappa_X^2}{16(1-\delta_X)} \right) + \dfrac{\kappa_X^2}{2(1-\delta_X)} \left( 1 - \dfrac{1}{A} \dfrac{16(1-\delta_X) + \kappa_X^2}{16(1-\delta_X)} \right) \operatorname{arcsinh} \dfrac{2(1-\delta_X)}{\kappa_X} \right] \\
\qquad\qquad \text{if } t^- = \dfrac{1}{2} \\
\dfrac{\kappa_X}{\pi \boldsymbol{E}_1(\kappa_X)} \left\{ \left( 1 - \dfrac{1}{A} \dfrac{(1+\delta_X)t^- - \delta_X}{2t^- - 1} \right) \left[ \dfrac{\sqrt{t^{-2}+1/\kappa^{-2}}}{t^-} + \dfrac{1-t^-}{\sqrt{2t^--1}} \left( F^*(\varphi^-, k^-) - E^*(\varphi^-, k^-) \right) \right] + \cdots \right. \\
\qquad \left. + \dfrac{1}{A} \dfrac{1-\delta_X}{2} \dfrac{1-t^-}{2t^--1} \left( \dfrac{\sqrt{t^{-2}+1/\kappa^{-2}}}{1-t^-} + \dfrac{1-t^-}{\sqrt{2t^--1+1/\kappa^{-2}}} \ln \dfrac{\sqrt{t^{-2}+1/\kappa^{-2}} + \sqrt{2t^--1+1/\kappa^{-2}}}{1-t^-} \right) \right\} \\
\qquad\qquad \text{if } \dfrac{1}{2} < t^- < 1 \\
\dfrac{1}{\pi \boldsymbol{E}_1(\kappa_X)} \sqrt{\kappa_X^2 + (1-\delta_X)^2} \left( 1 - \dfrac{1}{A} \dfrac{1+\delta_X}{2} \right) \qquad \text{if } t^- = 1,
\end{cases}
$$

where

$$
\varphi^- = \arcsin \frac{\sqrt{2t^- - 1}}{t^-} \quad , \quad k^- = \frac{1}{\kappa^- \sqrt{2t^- - 1}} \quad ,
$$

and

$$
E(\varphi, k) = \int_0^{\varphi} \sqrt{1 - k^2 \sin^2 \theta}\, d\theta
$$

is the incomplete elliptic integral of the second kind. We have introduced the following functions:

$$
F^*(\varphi, k) = \int_0^{\varphi} \frac{1}{\sqrt{1 + k^2 \sin^2 \theta}}\, d\theta = \frac{1}{\sqrt{1+k^2}} \left[ \boldsymbol{K}\left( \frac{k}{\sqrt{1+k^2}} \right) - F\left( \frac{\pi}{2} - \varphi, \frac{k}{\sqrt{1+k^2}} \right) \right]
$$

and

$$E^*(\varphi,k)=\int_0^{\varphi}\sqrt{1+k^2\sin^2\theta}\,d\theta=\sqrt{1+k^2}\left[\boldsymbol{E}\left(\frac{k}{\sqrt{1+k^2}}\right)-E\left(\frac{\pi}{2}-\varphi,\frac{k}{\sqrt{1+k^2}}\right)\right]\ ,$$

where

$$\boldsymbol{K}(k)=\int_0^{\pi/2}\frac{1}{\sqrt{1-k^2\sin^2\theta}}\,d\theta$$

and

$$F(\varphi,k)=\int_0^{\varphi}\frac{1}{\sqrt{1-k^2\sin^2\theta}}\,d\theta$$

are the complete and incomplete elliptic integrals of the first kind, respectively. In the above expressions, $(t^-)^2$ and $(\kappa^-)^2$ have been written $t^{-2}$ and $\kappa^{-2}$, respectively, since there is no ambiguity.

$$\Theta_S^{*+}=\begin{cases}
\dfrac{\kappa_X}{\pi\boldsymbol{E}_1(\kappa_X)}\dfrac{1-t^+}{\sqrt{1-2t^+}}\left[\left(1-\dfrac{1}{A}\dfrac{\delta_X+(1-\delta_X)t^+}{1-2t^+}\right)E\left(\theta_X^+,\sqrt{1-\dfrac{1}{(1-2t^+)\kappa^{+2}}}\right)+\cdots\right.\\
\qquad\left.+\dfrac{1}{A}\dfrac{1+\delta_X}{2}\dfrac{1}{\sqrt{1-2t^+}}\left(\dfrac{\sqrt{t^{+2}+1/\kappa^{+2}}}{1-t^+}+\dfrac{1-t^+}{\sqrt{1-2t^+-1/\kappa^{+2}}}\arcsin\dfrac{\sqrt{1-2t^+-1/\kappa^{+2}}}{1-t^+}\right)\right]\\
\qquad\qquad\text{if } 0\le t^+<\dfrac{1}{2}-\dfrac{1}{2\kappa^{+2}}\\
\dfrac{1}{2\pi\boldsymbol{E}_1(\kappa_X)}\dfrac{\kappa_X^2+(1+\delta_X)^2}{1+\delta_X}\left[\left(1-\dfrac{1}{2A}\dfrac{\kappa_X^2+\delta_X^2-1}{1+\delta_X}\right)\arcsin\dfrac{2\kappa_X(1+\delta_X)}{\kappa_X^2+(1+\delta_X)^2}+\dfrac{\kappa_X}{A}\right]\quad\text{if } t^+=\dfrac{1}{2}-\dfrac{1}{2\kappa^{+2}}\\
\dfrac{1+\delta_X}{\pi\boldsymbol{E}_1(\kappa_X)}\dfrac{1-t^+}{1-2t^+}\left\{\left(1-\dfrac{1}{A}\dfrac{\delta_X+(1-\delta_X)t^+}{1-2t^+}\right)\left[\boldsymbol{E}\left(\sqrt{1-(1-2^+)\kappa^{+2}}\right)-E\left(\dfrac{\pi}{2}-\theta_X^+,\sqrt{1-(1-2t^+)\kappa^{+2}}\right)\right]+\cdots\right.\\
\qquad\left.+\dfrac{\kappa_X}{2A}\left(\dfrac{\sqrt{t^{+2}+1/\kappa^{+2}}}{1-t^+}+\dfrac{1-t^+}{\sqrt{2t^+-1+1/\kappa^{+2}}}\ln\dfrac{\sqrt{t^{+2}+1/\kappa^{+2}}+\sqrt{2t^+-1+1/\kappa^{+2}}}{1-t^+}\right)\right\}\\
\qquad\qquad\text{if } \dfrac{1}{2}-\dfrac{1}{2\kappa^{+2}}<t^+<\dfrac{1}{2}\\
\dfrac{1}{2\pi\boldsymbol{E}_1(\kappa_X)}\left[\sqrt{\kappa_X^2+4(1+\delta_X)^2}\left(1+\dfrac{1}{A}\dfrac{8(1-\delta_X^2)-\kappa_X^2}{16(1+\delta_X)}\right)+\dfrac{\kappa_X^2}{2(1+\delta_X)}\left(1+\dfrac{1}{A}\dfrac{16(1+\delta_X)+\kappa_X^2}{16(1+\delta_X)}\right)\operatorname{arcsinh}\dfrac{2(1+\delta_X)}{\kappa_X}\right]\\
\qquad\qquad\text{if } t^+=\dfrac{1}{2}\\
\dfrac{\kappa_X}{\pi\boldsymbol{E}_1(\kappa_X)}\left\{\left(1+\dfrac{1}{A}\dfrac{(1-\delta_X)t^++\delta_X}{2t^+-1}\right)\left[\dfrac{\sqrt{t^{+2}+1/\kappa^{+2}}}{t^+}+\dfrac{1-t^+}{\sqrt{2t^+-1}}\left(F^*(\varphi^+,k^+)-E^*(\varphi^+,k^+)\right)\right]-\cdots\right.\\
\qquad\left.-\dfrac{1}{A}\dfrac{1+\delta_X}{2}\dfrac{1-t^+}{2t^+-1}\left(\dfrac{\sqrt{t^{+2}+1/\kappa^{+2}}}{1-t^+}+\dfrac{1-t^+}{\sqrt{2t^+-1+1/\kappa^{+2}}}\ln\dfrac{\sqrt{t^{+2}+1/\kappa^{+2}}+\sqrt{2t^+-1+1/\kappa^{+2}}}{1-t^+}\right)\right\}\\
\qquad\qquad\text{if } \dfrac{1}{2}<t^+<1\\
\dfrac{1}{\pi\boldsymbol{E}_1(\kappa_X)}\sqrt{\kappa_X^2+(1+\delta_X)^2}\left(1+\dfrac{1}{A}\dfrac{1-\delta_X}{2}\right)\qquad\text{if } t^+=1\ ,
\end{cases}$$

where

$$\varphi^+ = \arcsin \frac{\sqrt{2t^+ - 1}}{t^+}$$

and

$$k^+ = \frac{1}{\kappa^+ \sqrt{2t^+ - 1}} \ .$$

In the above expressions, $(t^+)^2$ and $(\kappa^+)^2$ have been written $t^{+2}$ and $\kappa^{+2}$, respectively, since there is no ambiguity.

**Length**

$$\Theta_L^{*-} = \begin{cases} \dfrac{\kappa_X}{\pi \boldsymbol{E}_1(\kappa_X)} \dfrac{1-t^-}{\sqrt{1-2t^-}} E\left(\arcsin \dfrac{\sqrt{1-2t^-}}{1-t^-}, \sqrt{1 - \dfrac{1}{(1-2t^-)\kappa^{-2}}}\right) & \text{if } 0 \le t^- \le \dfrac{1}{2} - \dfrac{1}{2\kappa^{-2}} \\ \dfrac{\kappa_X}{\pi \boldsymbol{E}_1(\kappa_X)} \dfrac{1-t^-}{\sqrt{1-2t^-}} E^*\left(\arcsin \dfrac{\sqrt{1-2t^-}}{1-t^-}, \sqrt{\dfrac{1}{(1-2t^-)\kappa^{-2}} - 1}\right) & \text{if } \dfrac{1}{2} - \dfrac{1}{2\kappa^{-2}} \le t^- < \dfrac{1}{2} \\ \dfrac{1}{2\pi \boldsymbol{E}_1(\kappa_X)} \left[\sqrt{\kappa_X^2 + 4(1-\delta_X)^2} + \dfrac{\kappa_X^2}{2(1-\delta_X)} \ln\left(\dfrac{2(1-\delta_X) + \sqrt{\kappa_X^2 + 4(1-\delta_X)^2}}{\kappa_X}\right)\right] & \text{if } t^- = \dfrac{1}{2} \\ \dfrac{1}{\pi \boldsymbol{E}_1(\kappa_X)} \left\{ \kappa_X \dfrac{1-t^-}{\sqrt{2t^- - 1}} \left[ F^*\left(\arcsin \dfrac{\sqrt{2t^- - 1}}{t^-}, \dfrac{1}{\kappa^- \sqrt{2t^- - 1}}\right) - E^*\left(\arcsin \dfrac{\sqrt{2t^- - 1}}{t^-}, \dfrac{1}{\kappa^- \sqrt{2t^- - 1}}\right)\right] + \cdots \right. \\ \qquad \left. + \dfrac{(1-\delta_X)\sqrt{1 + \kappa^{-2} t^{-2}}}{t^-} \right\} & \text{if } \dfrac{1}{2} < t^- < 1 \end{cases}$$

$$\Theta_L^{*-} = \begin{cases} \dfrac{\kappa_X}{\pi \boldsymbol{E}_1(\kappa_X)} \dfrac{1-t^+}{\sqrt{1-2t^+}} E\left(\arcsin \dfrac{\sqrt{1-2t^+}}{1-t^+}, \sqrt{1 - \dfrac{1}{(1-2t^+)\kappa^{+2}}}\right) & \text{if } 0 \le t^+ \le \dfrac{1}{2} - \dfrac{1}{2\kappa^{+2}} \\ \dfrac{\kappa_X}{\pi \boldsymbol{E}_1(\kappa_X)} \dfrac{1-t^+}{\sqrt{1-2t^+}} E^*\left(\arcsin \dfrac{\sqrt{1-2t^+}}{1-t^+}, \sqrt{\dfrac{1}{(1-2t^+)\kappa^{+2}} - 1}\right) & \text{if } \dfrac{1}{2} - \dfrac{1}{2\kappa^{+2}} \le t^+ < \dfrac{1}{2} \\ \dfrac{1}{2\pi \boldsymbol{E}_1(\kappa_X)} \left[\sqrt{\kappa_X^2 + 4(1+\delta_X)^2} + \dfrac{\kappa_X^2}{2(1+\delta_X)} \ln\left(\dfrac{2(1+\delta_X) + \sqrt{\kappa_X^2 + 4(1+\delta_X)^2}}{\kappa_X}\right)\right] & \text{if } t^+ = \dfrac{1}{2} \\ \dfrac{1}{\pi \boldsymbol{E}_1(\kappa_X)} \left\{ \kappa_X \dfrac{1-t^+}{\sqrt{2t^+ - 1}} \left[ F^*\left(\arcsin \dfrac{\sqrt{2t^+ - 1}}{t^+}, \dfrac{1}{\kappa^+ \sqrt{2t^+ - 1}}\right) - E^*\left(\arcsin \dfrac{\sqrt{2t^+ - 1}}{t^+}, \dfrac{1}{\kappa^+ \sqrt{2t^+ - 1}}\right)\right] + \cdots \right. \\ \qquad \left. + \dfrac{(1+\delta_X)\sqrt{1 + \kappa^{+2} t^{+2}}}{t^+} \right\} & \text{if } \dfrac{1}{2} < t^+ < 1 \end{cases}$$

## APPENDIX B

### POLOIDAL SURFACE AND VOLUME INTEGRATION, EXPRESSION OF $\Theta_1$ IN TERMS OF $\Theta_V$ AND $\Theta_{Sp}$

The LCMS is supposed to have the following parametric equations:

$$x = x_1(\theta) \quad \text{and} \quad z = z_1(\theta) \ .$$

The coordinate origin $O$ is taken at the middle of the horizontal axis defined as the intersection of $z = 0$ with the LCMS. $R$ is the major radius corresponding to $O$, and $a$ is half the length of the internal part of the horizontal axis. $\theta$ is a poloidal angle that is supposed to vary between 0 and $2\pi$ (without loss of generality). The other magnetic surfaces are supposed to be similar to the LCMS with similarity center $O$ and a factor $\rho$. The parametric equations of the magnetic surface $\rho$ is then

$$x = \rho x_1(\theta) \quad \text{and} \quad z = \rho z_1(\theta) \ .$$

The variables $\rho, \theta$ are chosen to be the new integration variables. The corresponding Jacobian determinant is

$$J(\rho,\theta) = \rho a^2 J_1(\theta) \ , \quad \text{with } J_1(\theta) = |\xi_1 \zeta_1' - \zeta_1 \xi_1'| \ ,$$

where $\xi_1 = x_1/a$, $\zeta_1 = z_1/a$.

### B.I. POLOIDAL SURFACE INTEGRATION

Using the above Jacobian, we get

$$\int_{S_p} F(\rho)\, dS_p = \pi a^2 I_1 \int_0^1 F(\rho) 2\rho\, d\rho \ ,$$

where

$$I_1 = \frac{1}{2\pi} \int_0^{2\pi} J_1(\theta)\, d\theta \ .$$

In particular, we have

$$S_p = \pi a^2 I_1 \ ,$$

which finally gives Eq. (14).

### B.II. VOLUME INTEGRATION

In the same way,

$$\int_V F(\rho)\, dV = 2\pi R \times \pi a^2 \int_0^1 F(\rho) 2\rho\, d\rho \times \int_0^{2\pi} \frac{1}{2\pi} \left(1 + \frac{\rho}{A}\, \xi_1(\theta)\right) J_1^*(\theta)\, d\theta \ ,$$

giving

$$\int_V F(\rho)\, dV = 2\pi R \times \pi a^2 I_1 \int_0^1 F(\rho) \left(1 + \frac{\rho}{A}\, \frac{I_2}{I_1}\right) 2\rho\, d\rho \ ,$$

where

$$I_2 = \frac{1}{2\pi} \int_0^{2\pi} \xi_1(\theta) J_1(\theta)\, d\theta \ .$$

In particular, we have

$$V = 2\pi R \times \pi a^2 I_1 \left(1 + \frac{2}{3}\, \frac{I_2}{I_1}\, \frac{1}{A}\right) \ .$$

Introducing

$$\Theta_1 = -\frac{2}{3}\, \frac{I_2}{I_1} \ ,$$

Eqs. (15) and (16) are finally obtained.

## APPENDIX C

## INTEGRAL EXPRESSIONS USED FOR AVERAGE CALCULATIONS

The following integral is used:

$$\int_0^1 (1 - \rho^\beta)^\alpha \rho^{\gamma'}\, d\rho = \frac{1}{\beta} B\left(1 + \alpha, \frac{1 + \gamma'}{\beta}\right) \ ,$$

where

$$B(x,y) = \frac{\Gamma(x)\Gamma(y)}{\Gamma(x+y)}$$

is the Euler beta function. In the special case $\beta = 2$, the above expression may be rewritten as

$$\int_0^1 (1 - \rho^2)^\alpha \rho^\gamma 2\rho\, d\rho = \frac{1}{1+\alpha}\, \frac{\Gamma\left(1 + \frac{\gamma}{2}\right)\Gamma(2+\alpha)}{\Gamma\left(2 + \alpha + \frac{\gamma}{2}\right)} \ ,$$

where the following property has been used:

$$\Gamma(1+z) = z\Gamma(z) \ .$$

## APPENDIX D

## FUNCTIONS AND COEFFICIENTS INVOLVED IN THE AVERAGE QUANTITIES

### D.I. THE CASE OF GENERAL PROFILES

$$I^{(0)}(\rho_{ped}) = \frac{1}{1 - \frac{\Theta_1}{A}} \int_0^{\rho_{ped}} \left(1 - \frac{3}{2}\, \frac{\Theta_1}{A}\, \rho\right) 2\rho\, d\rho = \rho_{ped}^2\, \frac{1 - \frac{\Theta_1}{A}\, \rho_{ped}}{1 - \frac{\Theta_1}{A}}$$

$$I^{(1)}(\rho_{ped}) = \frac{1}{1 - \frac{\Theta_1}{A}} \int_{\rho_{ped}}^1 \left(1 - \frac{3}{2}\, \frac{\Theta_1}{A}\, \rho\right) 2\rho\, d\rho = 1 - I^{(0)}(\rho_{ped}) = (1 - \rho_{ped})\, \frac{1 + \rho_{ped} - \frac{\Theta_1}{A}\, (1 + \rho_{ped} + \rho_{ped}^2)}{1 - \frac{\Theta_1}{A}}$$

$$I_{lin1}^{(1)}(\rho_{ped}) = \frac{1}{1-\dfrac{\Theta_1}{A}} \int_{\rho_{ped}}^{1} \frac{1-\rho}{1-\rho_{ped}} \left(1 - \frac{3}{2}\,\frac{\Theta_1}{A}\,\rho\right) 2\rho\, d\rho = \frac{1-\rho_{ped}}{3}\, \frac{1 + 2\rho_{ped} - \dfrac{3}{4}\,\dfrac{\Theta_1}{A}\,(1 + 2\rho_{ped} + 3\rho_{ped}^2)}{1-\dfrac{\Theta_1}{A}}$$

$$I_n^{(0)}(\alpha_n, \rho_{ped}) = \frac{1}{1-\dfrac{\Theta_1}{A}} \int_0^{\rho_{ped}} \left(1 - \frac{\rho^2}{\rho_{ped}^2}\right)^{\alpha_n} \left(1 - \frac{3}{2}\,\frac{\Theta_1}{A}\,\rho\right) 2\rho\, d\rho = \frac{\rho_{ped}^2}{1+\alpha_n}\, \frac{1 - \dfrac{\Theta_1}{A}\,\rho_{ped}\,\Gamma_1(\alpha_n)}{1-\dfrac{\Theta_1}{A}} \quad ,$$

with

$$\Gamma_1(\alpha) = \frac{3\sqrt{\pi}}{4}\, \frac{\Gamma(2+\alpha)}{\Gamma\left(\dfrac{5}{2} + \alpha\right)} \quad \text{with} \quad \Gamma_1(0) = 1 \quad .$$

The coefficients appearing in the expressions of $T_{e0}$ and $\langle T_e \rangle$ may be written as

$$\begin{cases} A_0 = [n_{ped}^*(I^{(0)} + I_{lin1}^{(1)}) + (1 - n_{ped}^*) I_n^{(0)}]\langle n_e \rangle \\ B_0 = [n_{ped}^*(I^{(0)} - I_T^{(0)} + I_{lin2}^{(1)}) + (1 - n_{ped}^*)(I_n^{(0)} - I_{nT}^{(0)})]\langle n_e \rangle - \cdots \\ \qquad - \{n_{ped}^*[(I^{(0)} - I_T^{(0)}) I^{(1)} - (2I^{(0)} - I_T^{(0)} + I_{lin1}^{(1)}) I_{lin1}^{(1)} + (I^{(0)} + I^{(1)}) I_{lin2}^{(1)}] + \cdots \\ \qquad\quad + (1 - n_{ped}^*)[(I_n^{(0)} - I_{nT}^{(0)}) I^{(1)} - (2I_n^{(0)} - I_{nT}^{(0)}) I_{lin1}^{(1)} + I_n^{(0)} I_{lin2}^{(1)}]\} n_{e,sep} \\ C_0 = n_{ped}^*(I_{lin1}^{(1)} - I_{lin2}^{(1)})\langle n \rangle + \{n_{ped}^*[I^{(0)} I^{(1)} - (2I^{(0)} + I_{lin1}^{(1)}) I_{lin1}^{(1)} + (I^{(0)} + I^{(1)}) I_{lin2}^{(1)}] + \cdots \\ \qquad\qquad + (1 - n_{ped}^*) I_n^{(0)} (I^{(1)} - 2I_{lin1}^{(1)} + I_{lin2}^{(1)})\} n_{e,sep} \end{cases}$$

$$\begin{cases} A_V = I_T^{(0)}[n_{ped}^*(I^{(0)} + I_{lin1}^{(1)}) + (1 - n_{ped}^*) I_n^{(0)}]\langle n_e \rangle \\ B_V = \{n_{ped}^* I_T^{(0)}(I_{lin1}^{(1)} - I_{lin2}^{(1)}) - (1 - n_{ped}^*)[I_n^{(0)} I_T^{(0)} - I_{nT}^{(0)}(I^{(0)} + I_{lin1}^{(1)})]\}\langle n_e \rangle - \cdots \\ \qquad - \{n_{ped}^* I_T^{(0)}(I^{(0)} + I^{(1)})(I_{lin1}^{(1)} - I_{lin2}^{(1)}) - \cdots \\ \qquad\quad - (1 - n_{ped}^*)\{(I_n^{(0)} I_T^{(0)} - I^{(0)} I_{nT}^{(0)}) I^{(1)} - [2I_n^{(0)} I_T^{(0)} - I_{nT}^{(0)}(I^{(0)} - I^{(1)} + I_{lin1}^{(1)})] I_{lin1}^{(1)} + I_n^{(0)} I_T^{(0)} I_{lin2}^{(1)}\}\} n_{e,sep} \\ C_V = [n_{ped}^* I_T^{(0)}(I^{(1)} - 2I_{lin1}^{(1)} + I_{lin2}^{(1)}) + (1 - n_{ped}^*) I_{nT}^{(0)}(I^{(0)} - I_{lin1}^{(1)})]\langle n_e \rangle - \cdots \\ \qquad - \{n_{ped}^* I_T^{(0)}(I^{(0)} + I^{(1)})(I^{(1)} - 2I_{lin1}^{(1)} + I_{lin2}^{(1)}) + (1 - n_{ped}^*) \\ \qquad\quad \times [I_n^{(0)} I_T^{(0)}(I^{(1)} - 2I_{lin1}^{(1)} + I_{lin2}^{(1)}) + I_{nT}^{(0)}(I^{(1)} - I_{lin1}^{(1)})^2]\} n_{e,sep} \quad , \end{cases}$$

where

$$I_{lin2}^{(1)}(\rho_{ped}) = \frac{1}{1-\dfrac{\Theta_1}{A}} \int_{\rho_{ped}}^{1} \left(\frac{1-\rho}{1-\rho_{ped}}\right)^2 \left(1 - \frac{3}{2}\,\frac{\Theta_1}{A}\,\rho\right) 2\rho\, d\rho$$

$$= \frac{1-\rho_{ped}}{6}\, \frac{1 + 3\rho_{ped} - \dfrac{3}{5}\,\dfrac{\Theta_1}{A}\,(1 + 3\rho_{ped} + 6\rho_{ped}^2)}{1-\dfrac{\Theta_1}{A}}$$

$$I_T^{(0)}(\beta_T,\alpha_T,\rho_{ped}) = \frac{1}{1-\dfrac{\Theta_1}{A}} \int_0^{\rho_{ped}} \left(1-\frac{\rho^{\beta_T}}{\rho_{ped}^{\beta_T}}\right)^{\alpha_T} \left(1-\frac{3}{2}\,\frac{\Theta_1}{A}\,\rho\right) 2\rho\, d\rho$$

$$= \rho_{ped}^2 \frac{\Gamma(1+\alpha_T)}{1-\dfrac{\Theta_1}{A}} \left[ \frac{\Gamma(1+2/\beta_T)}{\Gamma(1+\alpha_T+2/\beta_T)} - \frac{\Theta_1}{A}\,\rho_{ped}\,\frac{\Gamma(1+3/\beta_T)}{\Gamma(1+\alpha_T+3/\beta_T)} \right]$$

$$I_{nT}^{(0)}(\alpha_n,\beta_T,\alpha_T,\rho_{ped}) = \frac{1}{1-\dfrac{\Theta_1}{A}} \int_0^{\rho_{ped}} \left(1-\frac{\rho^2}{\rho_{ped}^2}\right)^{\alpha_n} \left(1-\frac{\rho^{\beta_T}}{\rho_{ped}^{\beta_T}}\right)^{\alpha_T} \left(1-\frac{3}{2}\,\frac{\Theta_1}{A}\,\rho\right) 2\rho\, d\rho \ .$$

$I_{nT}^{(0)}$ cannot be expressed in closed form; it is calculated numerically in the code.

### D.II. THE CASE OF PARABOLIC TYPE PROFILES

In this case, expressions in Sec. II.D.2.a simplify to give

$$n_{e0} = \langle n_e\rangle(1+\alpha_n)\,\frac{1-\dfrac{\Theta_1}{A}}{1-\dfrac{\Theta_1}{A}\,\Gamma_1(\alpha_n)} \ , \tag{D.1}$$

$$\bar{n}_e = n_{e0}\,2^{2\alpha_n}\,\frac{\Gamma^2(1+\alpha_n)}{\Gamma(2+2\alpha_n)} \ ,$$

$$T_{e0} = \langle T_e\rangle_n\,\frac{1+\alpha_n+\alpha_T}{1+\alpha_n}\,\frac{1-\dfrac{\Theta_1}{A}\,\Gamma_1(\alpha_n)}{1-\dfrac{\Theta_1}{A}\,\Gamma_1(\alpha_n+\alpha_T)} \ ,$$

and

$$\langle T_e\rangle = \langle T_e\rangle_n\,\frac{1+\alpha_n+\alpha_T}{(1+\alpha_n)(1+\alpha_T)}\,\frac{\left[1-\dfrac{\Theta_1}{A}\,\Gamma_1(\alpha_n)\right]\left[1-\dfrac{\Theta_1}{A}\,\Gamma_1(\alpha_T)\right]}{\left(1-\dfrac{\Theta_1}{A}\right)\left[1-\dfrac{\Theta_1}{A}\,\Gamma_1(\alpha_n+\alpha_T)\right]} \ .$$

## APPENDIX E

## FIT FOR THE D-T THERMONUCLEAR REACTION RATE

### E.I. SADLER-VAN BELLE FIT

The expression used in the code is taken from Ref. 33. It may be written as

$$\overline{\sigma v}_{\rm DT}(T_i) = \frac{a}{T_i^{2/3}}\,\frac{1}{U^{5/6}}\exp\left(-\frac{b}{T_i^{1/3}}\,U^{1/3}\right) \ ,$$

with

$$a = \frac{P_1 B^{1/3}}{2^{1/3}(\mu c^2_{\rm keV})^{1/2}} \quad \text{and} \quad b = \frac{3B^{2/3}}{2^{2/3}} \ ,$$

where $\mu = m_{\rm D}m_{\rm T}/(m_{\rm D}+m_{\rm T})$ is the deuterium-tritium reduced mass and

$$B\ ({\rm keV}^{1/2}) = \frac{\sqrt{2}e^2}{4\varepsilon_0\hbar c}\,(\mu c^2_{\rm keV})^{1/2} \ .$$

The following values are taken for the calculation:

$$\mu c^2_{\text{keV}} = 1.124656 \times 10^6$$

and

$$B\ (\text{keV}^{1/2}) = 34.3827025\ .$$

We have

$$U(T_i) = 1 - T_i \frac{P_2 + (P_4 + P_6 T_i)T_i}{1 + (P_3 + P_5 T_i)T_i}\ ,$$

with

$$P_1 = 1.0545128 \times 10^{-15}\ , \quad P_2 = 2.5077133 \times 10^{-2}\ ,$$
$$P_3 = 6.6024089 \times 10^{-2}\ , \quad P_4 = 2.5773408 \times 10^{-3}\ ,$$
$$P_5 = 8.1215505 \times 10^{-3}\ , \quad P_6 = -6.1880463 \times 10^{-5}\ .$$

The essential feature of this Peres-like fit[34] is that the constant $b$ is not adjusted, so that the asymptotic expansion of $\overline{\sigma v}_{\text{DT}}(T_i)$ for low temperature is the correct Gamow formula. For that reason, it is assumed, following Peres, that the above expression is correct for 0 keV $< T_i <$ 100 keV provided that the optimized function $U(T_i)$ is retained.

### E.II. MONOMIAL FITS

For analytical calculations, the following monomial fits of $\overline{\sigma v}_{\text{DT}}(T_i)$ are useful:

$$\overline{\sigma v}_{\text{DT}}(T_i) = 1.15 \times 10^{-25} T_i^3 \quad \text{for } 5.3 \text{ keV} \le T_i \le 10.3 \text{ keV}\ ,$$

$$\overline{\sigma v}_{\text{DT}}(T_i) = 1.18 \times 10^{-24} T_i^2 \quad \text{for } 10.3 \text{ keV} \le T_i \le 18.5 \text{ keV}\ ,$$

$$\overline{\sigma v}_{\text{DT}}(T_i) = 2.18 \times 10^{-23} T_i \quad \text{for } 18.5 \text{ keV} \le T_i \le 39.9 \text{ keV}\ ,$$

and

$$\overline{\sigma v}_{\text{DT}}(T_i) = 8.69 \times 10^{-22} \quad \text{for } 39.9 \text{ keV} \le T_i \le 100 \text{ keV}\ .$$

## APPENDIX F

## REDUCTION OF $\int_{S_p} \frac{1}{\eta(\rho)} \frac{R_0}{R}\, dS_p$ TO A SIMPLE INTEGRAL

The integral may be decomposed as

$$\int_{S_p} \frac{1}{\eta} \frac{R_0}{R}\, dS_p = \frac{1}{2}\left( \int_{S_p^{-(1)}} \frac{1}{\eta} \frac{R_0}{R}\, dS_p + \int_{S_p^{-(2)}} \frac{1}{\eta} \frac{R_0}{R}\, dS_p \right) + \frac{1}{2}\left( \int_{S_p^{+(1)}} \frac{1}{\eta} \frac{R_0}{R}\, dS_p + \int_{S_p^{+(2)}} \frac{1}{\eta} \frac{R_0}{R}\, dS_p \right)\ ,$$

where $S_p^{-(i)}$ represents a virtual symmetrical internal cross section with parameters $\kappa_X^{(i)}$, $\delta_X^{(i)}$, and $\psi^{-(i)}$.

In the case of an elliptical internal cross section ($t^- < \frac{1}{2}$), we have

$$\int_{S_p^-} F(\rho) \frac{R_0}{R}\, dS_p = a^2 \beta^- \int_0^1 F(\rho) 2\rho\, d\rho \times \int_0^{\theta_X^-} \frac{\alpha^- - \alpha_0^- \cos\theta}{1 + \frac{\rho}{A}(\alpha_0^- - \alpha^- \cos\theta)}\, d\theta\ ,$$

where $\beta^-$, $\alpha^-$, and $\alpha_0^-$ are given in Eq. (4) and $\theta_X^-$ is given in Eq. (5). The $\theta$ integration can be done analytically, yielding

$$\int_{S_p^-} F(\rho) \frac{R_0}{R}\, dS_p = \frac{2a^2 A \kappa_X}{1 - \delta_X} \left( \int_0^1 2F(\rho)\, d\rho \frac{A[\delta_X - (1+\delta_X)t^-] + (1 - 2\delta_X + 2\delta_X t^-)\rho}{\sqrt{(A-\rho)[A(1-2t^-) + (1-2\delta_X + 2\delta_X t^-)\rho]}} \times \cdots \right.$$
$$\left. \times \arctan \sqrt{\frac{A(1-2t^-) + (1 - 2\delta_X + 2\delta_X t^-)\rho}{A - \rho}} - \frac{\delta_X - (1+\delta_X)t^-}{\sqrt{1-2t^-}} \theta_X^- \int_0^1 F(\rho)\, d\rho \right)\ .$$

In the case of a parabolic internal cross section ($t^- = \frac{1}{2}$), we get

$$\int_{S_p^-} F(\rho) \frac{R_0}{R}\, dS_p = 2a^2 A \kappa_X \left[ \frac{1}{\sqrt{1-\delta_X}} \int_0^1 F(\rho)\, d\rho \frac{2\rho - A}{\sqrt{\rho(A-\rho)}} \arctan \sqrt{\frac{(1-\delta_X)\rho}{A-\rho}} + \int_0^1 F(\rho)\, d\rho \right]\ .$$

In the case of a hyperbolic internal cross section ($t^- > \frac{1}{2}$), we get

$$\int_{S_p^-} F(\rho) \frac{R_0}{R}\, dS_p = -a^2 \beta^- \int_0^1 F(\rho) 2\rho\, d\rho \int_0^{\varphi_X^-} \frac{\alpha^- + \alpha_0^- \cosh\varphi}{1 + \frac{\rho}{A}(\alpha_0^- + \alpha^- \cosh\varphi)}\, d\varphi\ ,$$

where $\beta^-$, $\alpha^-$, and $\alpha_0^-$ are given in Eq. (6) and $\varphi_X^-$ is given in Eq. (7). The $\varphi$ integration can be done analytically, yielding

$$\int_{S_p^-} F(\rho)\,\frac{R_0}{R}\,dS_p = \frac{2a^2A\kappa_X}{1-\delta_X}\left(\int_0^{A(2t^- -1)/(1-2\delta_X+2\delta_X t^-)} 2F(\rho)\,d\rho\,\frac{A[\delta_X-(1+\delta_X)t^-]+(1-2\delta_X+2\delta_X t^-)\rho}{\sqrt{(A-\rho)[A(2t^- -1)-(1-2\delta_X+2\delta_X t^-)\rho]}}\times\cdots\right.$$

$$\times \operatorname{arctanh}\sqrt{\frac{A(2t^- -1)-(1-2\delta_X+2\delta_X t^-)\rho}{A-\rho}}+\cdots$$

$$+\int_{A(2t^- -1)/(1-2\delta_X+2\delta_X t^-)}^1 2F(\rho)\,d\rho\,\frac{A[\delta_X-(1+\delta_X)t^-]+(1-2\delta_X+2\delta_X t^-)\rho}{\sqrt{(A-\rho)[(1-2\delta_X+2\delta_X t^-)\rho-A(2t^- -1)]}}\times\cdots$$

$$\left.\times \arctan\sqrt{\frac{(1-2\delta_X+2\delta_X t^-)\rho-A(2t^- -1)}{A-\rho}}-\frac{\delta_X-(1+\delta_X)t^-}{\sqrt{2t^- -1}}\,\varphi_X^-\int_0^1 F(\rho)\,d\rho\right)$$

for $A(2t^- -1) < 1-2\delta_X+2\delta_X t^-$, or

$$\int_{S_p^-} F(\rho)\,\frac{R_0}{R}\,dS_p = \frac{2a^2A\kappa_X}{1-\delta_X}\left(\int_0^1 2F(\rho)\,d\rho\,\frac{a[\delta_X-(1+\delta_X)t^-]+(1-2\delta_X+2\delta_X t^-)\rho}{\sqrt{(A-\rho)[A(2t^- -1)-(1-2\delta_X+2\delta_X t^-)\rho]}}\times\cdots\right.$$

$$\left.\times \operatorname{arctanh}\sqrt{\frac{A(2t^- -1)-[1-2\delta_X+2\delta_X t^-]\rho}{A-\rho}}-\frac{\delta_X-(1+\delta_X)t^-}{\sqrt{2t^- -1}}\,\varphi_X^-\int_0^1 F(\rho)\,d\rho\right)$$

for $A(2t^- -1) \geq 1-2\delta_X+2\delta_X t^-$.

In the case of a straight line internal cross section ($t^- = 1$), we get

$$\int_{S_p^-} F(\rho)\,\frac{R_0}{R}\,dS_p = \frac{2a^2A\kappa_X}{1-\delta_X}\int_0^1 F(\rho)\,d\rho\,\ln\frac{A-\delta_X\rho}{A-\rho}\quad .$$

In the case of an elliptical external cross section ($t^+ < \frac{1}{2}$), we have

$$\int_{S_p^+} F(\rho)\,\frac{R_0}{R}\,dS_p = a^2\beta^+\int_0^1 F(\rho)2\rho\,d\rho\int_0^{\theta_X^+}\frac{\alpha^+ + \alpha_0^+\cos\theta}{1+\dfrac{\rho}{A}\,(\alpha_0^+ + \alpha^+\cos\theta)}\,d\theta\quad ,$$

where $\beta^+$, $\alpha^+$, and $\alpha_0^+$ are given in Eq. (8) and $\theta_X^+$ is given in Eq. (9). The $\theta$ integration can be done analytically, yielding

$$\int_{S_p^+} F(\rho)\,\frac{R_0}{R}\,dS_p = \frac{2a^2A\kappa_X}{1+\delta_X}\left(\int_0^{A(1-2t^+)/(1+2\delta_X-2\delta_X t^+)} 2F(\rho)\,d\rho\,\frac{A[\delta_X+(1-\delta_X)t^+]+(1+2\delta_X-2\delta_X t^+)\rho]}{\sqrt{(A+\rho)[A(1-2t^+)-(1+2\delta_X-2\delta_X t^+)\rho]}}\times\cdots\right.$$

$$\times \arctan\sqrt{\frac{A(1-2t^+)-(1+2\delta_X-2\delta_X t^+)\rho}{A+\rho}}+\cdots$$

$$+\int_{A(1-2t^+)/(1+2\delta_X-2\delta_X t^+)}^1 2F(\rho)\,d\rho\,\frac{A[\delta_X+(1-\delta_X)t^+]+(1+2\delta_X-2\delta_X t^+)\rho}{\sqrt{(A+\rho)[(1+2\delta_X-2\delta_X t^+)\rho-A(1-2t^+)]}}\times\cdots$$

$$\left.\times \operatorname{arctanh}\sqrt{\frac{(1+2\delta_X-2\delta_X t^+)\rho-A(1-2t^+)}{A+\rho}}-\frac{\delta_X+(1-\delta_X)t^+}{\sqrt{1-2t^+}}\,\theta_X^+\int_0^1 F(\rho)\,d\rho\right)$$

for $A(1-2t^+) < 1+2\delta_X - 2\delta_X t^+$, or

$$\int_{S_p^+} F(\rho)\,\frac{R_0}{R}\,dS_p = \frac{2a^2 A\kappa_X}{1+\delta_X}\left(\int_0^1 2F(\rho)\,d\rho\,\frac{A[\delta_X+(1-\delta_X)t^+]+(1+2\delta_X-2\delta_X t^+)\rho}{\sqrt{(A+\rho)[A(1-2t^+)-(1+2\delta_X-2\delta_X t^+)\rho]}}\times\cdots\right.$$
$$\left.\times\arctan\sqrt{\frac{A(1-2t^+)-(1+2\delta_X-2\delta_X t^+)\rho}{A+\rho}}-\frac{\delta_X+(1-\delta_X)t^+}{\sqrt{1-2t^+}}\,\theta_X^+\int_0^1 F(\rho)\,d\rho\right)$$

for $A(1-2t^+) \geq 1+2\delta_X-2\delta_X t^+$.

In the case of a parabolic external cross section ($t^+ = \frac{1}{2}$), we get

$$\int_{S_p^+} F(\rho)\,\frac{R_0}{R}\,dS_p = 2a^2 A\kappa_X\left[\frac{1}{\sqrt{1+\delta_X}}\int_0^1 F(\rho)\,d\rho\,\frac{A+2\rho}{\sqrt{\rho(A+\rho)}}\operatorname{arctanh}\sqrt{\frac{(1+\delta_X)\rho}{A+\rho}}-\int_0^1 F(\rho)\,d\rho\right]\,.$$

In the case of a hyperbolic external cross section ($t^+ > \frac{1}{2}$), we get

$$\int_{S_p^+} F(\rho)\,\frac{R_0}{R}\,dS_p = a^2\beta^+\int_0^1 F(\rho)2\rho\,d\rho\int_0^{\varphi_X^+}\frac{\alpha^+ + \alpha_0^+\cosh\varphi}{1+\dfrac{\rho}{A}\,(\alpha_0^+ + \alpha^+\cosh\varphi)}\,d\varphi\,,$$

where $\beta^+$, $\alpha^+$, and $\alpha_0^+$ are given in Eq. (10) and $\varphi_X^+$ is given in Eq. (11). The $\varphi$ integration can be done analytically, yielding

$$\int_{S_p^+} F(\rho)\,\frac{R_0}{R}\,dS_p = \frac{2a^2 A\kappa_X}{1+\delta_X}\left(\int_0^1 2F(\rho)\,d\rho\,\frac{A[\delta_X+(1-\delta_X)t^+]+(1+2\delta_X-2\delta_X t^+)\rho}{\sqrt{(A+\rho)[A(2t^+-1)+(1+2\delta_X-2\delta_X t^+)\rho]}}\times\cdots\right.$$
$$\left.\times\operatorname{arctanh}\sqrt{\frac{A(2t^+-1)+(1+2\delta_X-2\delta_X t^+)\rho}{A+\rho}}-\frac{\delta_X+(1-\delta_X)t^+}{\sqrt{2t^+-1}}\,\varphi_X^+\int_0^1 F(\rho)\,d\rho\right)\,.$$

In the case of a straight line external cross section ($t^+ = 1$), we get

$$\int_{S_p^+} F(\rho)\,\frac{R_0}{R}\,dS_p = \frac{2a^2 A\kappa_X}{1+\delta_X}\int_0^1 F(\rho)\,d\rho\,\ln\frac{A+\rho}{A-\delta_X\rho}\,.$$

## APPENDIX G

## EXPRESSION OF THE CONFINEMENT TIME IN TERMS OF THE AVERAGED ELECTRON TEMPERATURE FOR A PURELY MONOMIAL SCALING EXPRESSION WITH ARBITRARY EXPONENTS

A general monomial energy confinement time scaling is considered:

$$\tau_{E,sc} = C_\tau H M_{eff}^{x_M}\kappa_a^{x_\kappa}A^{x_A}\,\frac{I_p^{x_I}(\bar{n}_e)^{x_n}B_t^{x_B}R^{x_R}}{P_{net}^{x_P}}\,.$$

Solving Eq. (45) for $P_{net}$ and inserting into the above expression, we get

$$\tau_{E,sc} = C_{\tau 1}H^{1/(1-x_P)}\,\frac{(\bar{n}/\langle n\rangle)^{x_P/(1-x_P)}}{C_W^{x_P/(1-x_P)}}\,M_{eff}^{x_M/(1-x_P)}\kappa_a^{(x_\kappa-x_P)/(1-x_P)}A^{(x_A+2x_P)/(1-x_P)}$$
$$\times\,\frac{I_p^{x_I/(1-x_P)}(\bar{n}_e)^{(x_n-x_P)/(1-x_P)}B_t^{x_B/(1-x_P)}R^{(x_R-3x_P)/(1-x_P)}}{\langle T_e\rangle_n^{x_P/(1-x_P)}}\,,$$

with

$$C_{\tau 1} = \frac{C_\tau^{1/(1-x_P)}}{(6\pi^2 k)^{x_P/(1-x_P)}}$$

or, in terms of $n_N$ and $q_{95}$,

$$\tau_{E,sc} = C_{\tau 2} H^{1/(1-x_P)} \frac{(\bar{n}/\langle n\rangle)^{x_P/(1-x_P)}}{C_W^{x_P/(1-x_P)}} M_{eff}^{x_M/(1-x_P)} \kappa_a^{(x_\kappa + x_I + x_n - 2x_P)/(1-x_P)} F_q^{(x_I+x_n-x_P)/(1-x_P)} A^{(x_A+2x_P-2x_I)/(1-x_P)}$$

$$\times \frac{n_N^{(x_n-x_P)/(1-x_P)} B_t^{(x_I+x_B+x_n-x_P)/(1-x_P)} R^{(x_I+x_R-x_n-2x_P)/(1-x_P)}}{q_{95}^{(x_I+x_n-x_P)/(1-x_P)} \langle T_e\rangle_n^{x_P/(1-x_P)}} \quad ,$$

with

$$C_{\tau 2} = \frac{10^{14[(x_n-x_P)/(1-x_P)]}}{\pi^{(x_n-x_P)/(1-x_P)}} \left(\frac{2\pi}{\mu_0}\right)^{(x_I+x_n-x_P)/(1-x_P)} \frac{C_\tau^{1/(1-x_P)}}{(6\pi^2 k)^{x_P/(1-x_P)}} \quad .$$

## APPENDIX H

## EQUATION FOR THE HELIUM FRACTION

Using the definition of $\tau_{\rm He}^*$ in Eq. (3), we get

$$\frac{\tau_{\rm He}^*}{\tau_E} = \frac{4}{\langle n_e\rangle \overline{\sigma v}_{\rm DT}^*(\langle T_e\rangle_n)} \frac{f_{\rm He}}{C_\alpha(f_{\rm He})} \frac{1}{\tau_E} \quad .$$

Using the definition of $\tau_E$ according to Eq. (1), we get the following expression for $P_{con}$:

$$P_{con} = \frac{3k}{4} \frac{\tau_{\rm He}^*}{\tau_E} \langle n_e\rangle^2 \langle T_e\rangle_n \overline{\sigma v}_{\rm DT}^*(\langle T_e\rangle_n)$$

$$\times V \frac{C_\alpha(f_{\rm He}) C_W(f_{\rm He})}{f_{\rm He}} \quad . \qquad \text{(H.1)}$$

Making use of $P_{net} = P_{con}$ [Eq. (39)], the following relation is obtained:

$$P_{con} = \frac{3\langle n_e\rangle k \langle T_e\rangle_n V C_W(f_{\rm He})}{\tau_{E,sc}(\langle n_e\rangle, P_{con})} \quad ,$$

where $\tau_{E,sc}(\langle n_e\rangle, P_{net})$ is the scaling expression used for the confinement time. Inserting Eq. (H.1) into the above relation gives a relation of the following form:

$$F\left(\langle n_e\rangle, \langle T_e\rangle_n, \frac{\tau_{\rm He}^*}{\tau_E}, f_{\rm He}\right) = 0 \quad ,$$

which is the equation allowing the calculation of $f_{\rm He}$ for given $\langle n_e\rangle$, $\langle T_e\rangle_n$, and $\tau_{\rm He}^*/\tau_E$.

## ACKNOWLEDGMENTS

This work, supported by the European Communities under the contract of Association between EURATOM and CEA, was carried out within the framework of the European Fusion Development Agreement.

## REFERENCES

1. R. J. HAWRYLUK et al., "Principal Physics Developments Evaluated in the ITER Design Review," *Nucl. Fusion*, **49**, 065012 (2009).

2. B. SAOUTIC et al., "Evaluation of the Proposal 'FT3 A Facility in Support to a Fast Track to Fusion,'" DRFC/NTT-2007.002, Commissariat à l'Energie Atomique (Mar. 2007).

3. D. MAISONNIER et al., "A Conceptual Study of Commercial Fusion Power Plants," Final Report of the European Fusion Power Plant Conceptual Study, EFDA-RP-RE-5.0, European Fusion Development Agreement (Apr. 13, 2005).

4. P. J. KNIGHT, "A User's Guide to the PROCESS Systems Code," F/MI/PJK/PROCESS/DOCUMENTATION/MANUAL, United Kingdom Atomic Energy Authority (July 1996).

5. Z. DRAGOJLOVIC et al., "An Advanced Computational Algorithm for Systems Analysis of Tokamak Power Plants," *Fusion Eng. Des.*, **85**, 243 (2010).

6. "ITER Physics Basis," *Nucl. Fusion*, **39**, 2137 (1999).

7. O. KARDAUN et al., "The Tortuous Route of Confinement Prediction Near Operational Boundary; Improvement of Analysis Based on ITERH.DB4/L.DB3 Database," presented at 21st IAEA Fusion Energy Conference, Chengdu, China, 2006, IT/P1-10; http://www-pub.iaea.org/MTCD/Meetings/FEC2006/it_p1-10.pdf (current as of June 8, 2010).

8. N. A. UCKAN and ITER PHYSICS GROUP, "ITER Physics Design Guidelines," *Fusion Technol.*, **19**, 1493 (1991).

9. F. ALBAJAR, J. JOHNER, and G. GRANATA, "Improved Calculation of Synchrotron Radiation Losses in Realistic Tokamak Plasmas," *Nucl. Fusion*, **41**, 665 (2001).

10. I. FIDONE, G. GIRUZZI, and G. GRANATA, "Synchrotron Radiation Loss in Tokamaks of Arbitrary Geometry," *Nucl. Fusion*, **41**, 1755 (2001).

11. ADAS (Atomic Data and Analysis Structure), Web site: http://www.adas.ac.uk (current as of June 8, 2010).

12. R. CLARK, J. ABDALLAH, and D. POST, "Radiation Rates for Low Z Impurities in Edge Plasmas," *J. Nucl. Mater.*, **220–222**, 1028 (1995).

13. S. KAYE et al., "ITER L Mode Confinement Database," *Nucl. Fusion*, **37**, 1303 (1997).

14. W. A. HOULBERG, S. E. ATTENBERGER, and L. M. HIVELY, "Contour Analysis of Fusion Reactor Plasma Performance," *Nucl. Fusion*, **22**, 935 (1982).

15. N. A. UCKAN, J. S. TOLLIVER, W. A. HOULBERG, and S. E. ATTENBERGER, "Influence of Fast Alpha Diffusion and Thermal Alpha Buildup on Tokamak Reactor Performance," *Fusion Technol.*, **13**, 411 (1988).

16. Y. R. MARTIN, T. TAKIZUKA, and the ITPA CDBM H-MODE THRESHOLD DATABASE WORKING GROUP, "Power Requirement for Accessing the H-Mode in ITER," *J. Phys. Conf. Ser.,* **123**, 012033 (2008).

17. H. D. PACHER, W. D. D'HAESELEER, and G. W. PACHER, "Scaling of Divertor Conditions in ITER/NET with Density, Power, SOL Transport, Pitch, Size, and Particle Throughput," *Nucl. Fusion*, **32**, 1373 (1992).

18. G. F. MATTHEWS et al., "Studies in JET Divertors of Varied Geometry. II: Impurity Seeded Plasmas," *Nucl. Fusion*, **39**, 19 (1999).

19. A. S. KUKUSHKIN and H. D. PACHER, "Divertor Modelling and Extrapolation to Reactor Conditions," *Plasma Phys. Control. Fusion*, **44**, 931 (2002).

20. A. LOARTE et al., "Progress in the ITER Physics Basis," *Nucl. Fusion*, **47**, S203 (2007).

21. D. POST, J. ABDALLAH, R. E. H. CLARK, and N. PUTVINSKAYA, "Calculations of Energy Losses Due to Atomic Processes in Tokamaks with Applications to the International Thermonuclear Experimental Reactor Divertor," *Phys. Plasmas*, **2**, 2328 (1995).

22. J. G. CORDEY, for the ITPA H-Mode Database Working Group and the ITPA Pedestal Database Working Group, "A Two-Term Model of the Confinement in Elmy H-Modes Using the Global Confinement and Pedestal Databases," *Nucl. Fusion*, **43**, 670 (2003).

23. P. GOHIL et al., "Study of Giant Edge-Localized Modes in DIII-D and Comparison with Ballooning Theory," *Phys. Rev. Lett.*, **61**, 1603 (1988).

24. H. R. WILSON, "Bootstrap Current Scaling in Tokamaks," *Nucl. Fusion*, **32**, 257 (1992).

25. C. GORMEZANO et al., "Progress in the ITER Physics Basis, Chapter 6: Steady State Operation," *Nucl. Fusion*, **47**, S285 (2007).

26. M. FERRARA, I. H. HUTCHINSON, S. M. WOLFE, J. A. STILLERMAN, and T. M. FREDIAN, "Alcasim Simulation Code for Alcator C-Mod," *Proc. 45th IEEE Conf. Decision & Control*, San Diego, California, December 13–15, 2006.

27. A. LI-PUMA, J. BONNEMASON, L. CACHON, J. L. DUCHATEAU, and F. GABRIEL, "Consistent Integration in Preparing the Helium Cooled Lithium Lead DEMO-2007 Reactor," *Fusion Eng. Des.*, **84**, 1197 (2009).

28. "Progress in the ITER Physics Basis," *Nucl. Fusion*, **47**, S1 (2007).

29. "Plasma Performance Assessment (PPA)," ITER Documentation, N 19 RI 11 R0.1, ITER (Aug. 2004).

30. D. J. WARD, "Newly Developing Conceptions of DEMOs: Pulsing and Hydrogen," *Fusion Sci. Technol.*, **56**, 581 (2009).

31. H. ZOHM, "On the Minimum Size of DEMO," *Fusion Sci. Technol.*, **58**, 613 (2010).

32. CERN Program Library Web site, http://cernlib.web.cern.ch (current as of June 8, 2010).

33. G. J. SADLER and P. VAN BELLE, "An Improved Formulation of the $D(t,n)^4He$ Reaction Cross-Section," JET-IR(87)08, Joint European Torus (1987).

34. A. PERES, "Fusion Cross Sections and Thermonuclear Reaction Rates," *J. Appl. Phys.*, **50**, 5569 (1979).